

# Modelling Biofilm Structure and Biofilm-Micropollutant Interactions using an Individual-based Model

*by*

James Kuan Broughton

Thesis presented in partial fulfilment  
of the requirements for the Degree

*of*

**MASTER OF ENGINEERING  
(CHEMICAL ENGINEERING)**



in the Faculty of Engineering  
at Stellenbosch University

The financial assistance of the National Research Foundation (NRF) towards this research is hereby acknowledged. Opinions expressed and conclusions arrived at, are those of the author and are not necessarily to be attributed to the NRF.

*Supervisor*

Dr Tobias Louw

*Co-Supervisor*

Prof Gideon Wolfaardt

April 2019

## **DECLARATION**

By submitting this thesis electronically, I declare that the entirety of the work contained therein is my own, original work, that I am the sole author thereof (save to the extent explicitly otherwise stated), that reproduction and publication thereof by Stellenbosch University will not infringe any third party rights and that I have not previously in its entirety or in part submitted it for obtaining any qualification.

Date: April 2019

## PLAGIARISM DECLARATION

1. Plagiarism is the use of ideas, material and other intellectual property of another's work and to present it as my own.
2. I agree that plagiarism is a punishable offence because it constitutes theft.
3. I also understand that direct translations are plagiarism.
4. Accordingly all quotations and contributions from any source whatsoever (including the internet) have been cited fully. I understand that the reproduction of text without quotation marks (even when the source is cited) is plagiarism.
5. I declare that the work contained in this assignment, except where otherwise stated, is my original work and that I have not previously (in its entirety or in part) submitted it for grading in this module/assignment or another module/assignment.

Student number: .....

Initials and surname: .....

Signature: .....

Date: .....

## ABSTRACT

Micropollutants are emerging contaminants that have received considerable attention in recent years due to environmental concerns. Diclofenac is a nonsteroidal anti-inflammatory drug that is commonly detected in South African surface waters and has been shown to be persistent and harmful to the environment. Biofilms, which are composed of sessile, mixed microbial communities, play a key role in wastewater treatment and functioning of natural ecosystems. There is, however, a poor understanding of biofilm-micropollutant interactions in this context. Biofilm structure is a useful indicator of the effect of micropollutant exposure on a biofilm and its activity. Recently, individual-based models have been developed that can simulate biofilm structure from first principles and show potential as a tool to provide mechanistic understanding of these interactions. The aim of the project was to develop and validate an individual-based model capable of describing biofilm structural development of a sample, as well as reproducing observed effects of diclofenac exposure on biofilm structure. A further aim was to investigate the feasibility of observed biofilm structure for validation of the biofilm model.

Lumped biokinetic parameters of an environmental sample were estimated using batch respirometric methods and regression of model parameters. Heterotrophic growth was found to dominate in the sampled culture. The estimated parameters were thus used to calibrate lumped heterotrophic growth in the biofilm model. Mixed-species biofilms were cultivated in flow cells under control conditions and exposed to diclofenac at 0.1 and 10 mg.L<sup>-1</sup>. Confocal laser scanning microscopy was used to examine morphological changes in biofilm structure over time. Biofilm structural parameters were derived from microscopy data and compared to the simulation output. Observed structure of biofilms were successfully used to validate the proposed biofilm model. Experimental results indicated a dose-dependent response to diclofenac. Diclofenac at 10 mg.L<sup>-1</sup> significantly inhibited biofilm growth over the exposure period compared to a control. Exposure at 0.1 mg.L<sup>-1</sup> resulted in an increase in biofilm growth after 24 h. The biofilm model successfully reproduced observed trends in structure at 10 mg.L<sup>-1</sup> and 0.1 mg.L<sup>-1</sup>. More work is required to elucidate the complex microbial interactions of diclofenac in the µg.L<sup>-1</sup> range. This study showed that an individual-based model can reproduce *in vitro* biofilm structure development based on emergent structural parameters. Individual-based models coupled with comparative experimental methods show potential as a tool for investigating biofilm interactions and improving model development. However, areas of improvement were identified including model parameter uncertainties, limitations in the biofilm model, and reproducibility in experimental methods.

## ABSTRAK

Mikrobesoedelstowwe is opkomende kontaminante wat aansienlike aandag gekry het in die laaste jare as gevolg van bekommernisse oor die omgewing. Diclofenac is 'n nie-steroidale anti-inflammatoriese geneesmiddel wat algemeen in Suid-Afrikaanse oppervlakwater waargeneem word en is bewys om volhouwend en beskadigend vir die omgewing te wees. Biofilms, wat bestaan uit sessiel, gemengde mikrobieuse gemeenskappe, speel 'n belangrike rol in afvalwaterbehandeling en funksionering van natuurlike ekosisteme. Daar is egter gebrekkige insig oor biofilm-mikrobesoedelstof-interaksies in hierdie konteks. Biofilmstruktur is 'n nuttige indikator van die effek van mikrobesoedelstof blootstelling op 'n biofilm en sy aktiwiteit. Onlangs is individu-gebaseerde modelle ontwikkel wat biofilmstruktur kan simuleer vanuit eerste beginsels en wys potensiaal as 'n hulpmiddel om meganistiese insig in hierdie interaksies te verskaf. Die doel van hierdie projek was om 'n individu-gebaseerde model te ontwikkel geskik om die biofilm strukturele ontwikkeling van 'n steekproef te beskryf, sowel as om waargenome gevolge van diclofenac-blootstelling op biofilmstrukture te reproducere. 'n Verdere doel was om die uitvoerbaarheid van waargenome biofilmstrukture vir die validering van die biofilmmodel te ondersoek.

Gekonsentreerde biokinetiese parameters van 'n omgewingsproefsteek is beraam deur lot respirometriese metodes en regressie van modelparameters te gebruik. Dis gevind dat heterotrofiese groei in die proefsteekkultuur domineer. Die beraamde parameters is dus gebruik om gekonsentreerde heterotrofiese groei in die biofilmmodel te kalibreer. Gemengde-spesies-biofilm is gekweek in vloeiselle onder gekontroleerde toestande en blootgestel aan diclofenac by 0.1 en 10 mg.L<sup>-1</sup>. Konfokale-laserskanderingmikroskopie is gebruik om morfologiese veranderinge in biofilmstrukture oor tyd te ondersoek. Biofilm strukturele parameters is afgelei uit mikroskopie data en vergelyk met die simulasié uitsette. Die waargenome struktur van biofilms het die voorgestelde biofilmmodel suksesvol gevalideer. Eksperimentele resultate het 'n dosis-afhanklike respons op diclofenac aangedui. Diclofenac by 10 mg.L<sup>-1</sup> het biofilm groei aansienlik onderdruk oor die periode van blootstelling in vergelyking met 'n kontrole. Blootstelling by 0.1 mg.L<sup>-1</sup> het na 'n verhoging van biofilmgroei gelei na 24 uur. Die biofilmmodel het waargenome neigings in struktur by 10 mg.L<sup>-1</sup> en 0.1 mg.L<sup>-1</sup> suksesvol gereproducer. Meer werk word benodig om die komplekse mikrobieuse interaksies van diclofenac in die µg.L<sup>-1</sup> bestek te verklaar. Hierdie studie het gewys dat 'n individu-gebaseerde model *in vitro* biofilmstruktuurontwikkeling, gebaseer op opkomende strukturele parameters, kan reproducere. Individu-gebaseerde modelle wat gepaard gaan met vergelykende

eksperimentele metodes, wys potensiaal as 'n hulpmiddel om biofilminteraksies te ondersoek en om model ontwikkeling te verbeter. Areas van verbetering is egter geïdentifiseer, insluitend model parameter onsekerhede, beperkinge op die biofilmmodel, en herhaalbaarheid in eksperimentele metodes.

## ACKNOWLEDGMENTS

Firstly, I would like to thank my supervisor, Dr Tobi Louw, for his patience, support and encouragement, and for the valuable knowledge gained throughout this project. I also thank Tobi for the opportunities he has provided me.

I thank my co-supervisor, Prof Gideon Wolfaardt, for his friendly support, funding the experimental work, and providing the freedom to explore my work in his laboratory.

I thank members of the Wolfaardt lab', in particular Alno and Elanna for help with flow cell experiments, and Edward for his help with LCMS analysis.

I also thank Dr Jan-Ulrich Kreft for assistance with iDynoMiCS.

Funding support from the National Research Foundation, East Rand Water Care Association, and the Department of Process Engineering is acknowledged.

Finally, I acknowledge Keira Tucker for her understanding, critique, and encouragement during this period of study.

## TABLE OF CONTENTS

<b>List of Figures.....</b>	i
<b>List of Tables .....</b>	iv
<b>Nomenclature .....</b>	v
<b>Abbreviations .....</b>	vii
<b>Chapter 1: Introduction .....</b>	1
<b>Chapter 2: Literature Review.....</b>	3
2.1 Bacterial biofilms .....	3
2.1.1 What is a biofilm? .....	3
2.1.2 Biofilm formation .....	4
2.1.3 Factors influencing biofilm structure .....	5
2.1.4 Quantifying biofilm structure.....	8
2.2 Biofilm models.....	9
2.2.1 Types of biofilm models .....	11
2.3 Micropollutants .....	14
2.3.1 Diclofenac .....	15
2.3.2 Effect on microbial biofilms .....	16
2.4 Research aims and objectives.....	19
2.5 Key questions .....	19
2.6 Hypotheses .....	19
<b>Chapter 3: Parameter Estimation .....</b>	20
3.1 Materials and Methods .....	20
3.1.1 Inoculum seed and cultivation .....	20
3.1.2 Analytical procedures .....	21
3.1.3 Determination of decay coefficient of heterotrophic biomass .....	21
3.1.4 Determination of the maximum specific growth rate, half-saturation coefficient, and yield coefficient of heterotrophic bacteria by the respirometric method .....	23
3.1.4.1 Batch reactor .....	23
3.1.4.2 Batch reactor model and parameter fitting.....	23
3.1.3 Parameter sensitivity analysis .....	26
3.1.4 Statistical analysis .....	26
3.2 Results .....	27
3.2.1 Decay coefficient .....	27
3.2.2 Maximum specific growth rate, half-saturation coefficient, and yield coefficient .....	28
3.2.3 Parameter sensitivity analysis .....	32
<b>Chapter 4: Flow Cell Bioreactor and Biofilm Simulations .....</b>	34
4.1 Materials and Methods .....	34

4.1.1 Design and operation of bioreactor .....	34
4.1.2 Sterilisation of bioreactor.....	35
4.1.3 Inoculation of flow cells .....	35
4.1.4 Reactor optimisation.....	35
4.1.5 Experimental runs.....	36
4.1.5.1 Batch diclofenac screen.....	36
4.1.5.2 Validation .....	36
4.1.5.3 Diclofenac exposure .....	36
4.1.6 Liquid chromatography – mass spectrometry .....	37
4.1.7 Confocal microscopy of biofilms.....	38
4.1.7.1 Preparation of flow cells for microscopy.....	38
4.1.7.2 Image acquisition.....	39
4.1.8 Biofilm model .....	40
4.1.8.2 Model description .....	40
4.1.8.2 Simulations .....	41
4.1.9 Biofilm parameter calculations .....	44
4.1.10 Statistical analysis of biofilm parameters.....	46
4.2 Results .....	46
4.2.1 Validation.....	46
4.2.2 Diclofenac treatments .....	51
<b>Chapter 5: Discussion .....</b>	<b>59</b>
<b>Chapter 6: Conclusion .....</b>	<b>70</b>
<b>Chapter 7: References .....</b>	<b>73</b>
<b>Chapter 8: Appendices .....</b>	<b>81</b>
Appendix A: Supplementary information for Chapter 3 .....	81
Appendix B: Paraformaldehyde fixative (4%) protocol .....	83
Appendix C: Supplementary information for Chapter 4 .....	84
Appendix D: Sensitivity analysis of simulated structural parameters .....	86
Appendix E: Protocol file used to initiate iDy wholeMiCS simulations.....	88

## LIST OF FIGURES

<b>Figure 2.1.</b> Stages of the biofilm lifecycle. Planktonic bacteria encounter a suitable surface and initiate reversible adhesion. Eventually, irreversible adhesion takes place, followed by the growth and formation of microcolonies. Finally, a mature biofilm develops and detachment events occur to seed new biofilms. Reprinted with permission (Copyright Centre for Biofilm Engineering, Montana State University-Bozeman).....	4
<b>Figure 2.2.</b> Illustration of biofilm structural heterogeneity. Biofilms can develop complex architectures such as water channels, mushroom-like microcolonies, and streamers. Reprinted with permission (Copyright Centre for Biofilm Engineering, Montana State University-Bozeman). .....	5
<b>Figure 2.3.</b> <b>A.</b> Compartments typically defined in biofilm models. These include the bulk liquid, mass transfer boundary layer, biofilm, and substratum. <b>B.</b> Typical mass transfer boundary layer substrate conditions. Both figures redrawn from Wanner <i>et al.</i> (2006).....	11
<b>Figure 2.4.</b> Three approaches for representing biomass in a biofilm model. Particulate components can be represented as: <b>A.</b> a continuum, <b>B.</b> as discrete grid-based elements, or <b>C.</b> as discrete particles. Redrawn from Wanner <i>et al.</i> (2006).....	12
<b>Figure 2.5.</b> Molecular structure of diclofenac.....	15
<b>Figure 3.1.</b> Example plot of <b>A.</b> decay coefficient determination and <b>B.</b> corresponding soluble substrate and optical density data of environmental sample cultured in a batch reactor. Shown is data from run 3A. ....	27
<b>Figure 3.2.</b> Example plot of <b>A.</b> respirogram and <b>B.</b> corresponding heterotrophic biomass and substrate concentration profiles of environmental sample cultured in batch. Shown is data from run 3. NATU: Non-ATU.....	28
<b>Figure 3.3.</b> Non-linear regression of best fit parameter set to response variable profiles of three experimental repeats. Runs were conducted under the same conditions but varying initial concentrations of S <sub>s</sub> and X <sub>H</sub> . 95% prediction intervals are indicated.....	29
<b>Figure 3.4.</b> Parameter estimation response surface with sum of squared error (SSE) for OUR profiles. Shown is the error resulting from regression of the batch model to three OUR datasets over a range of $\mu_{\max,H}$ and K <sub>S</sub> values. The best fit parameter values are indicated by the black dot. .....	31
<b>Figure 3.5.</b> Sensitivity of response variable profiles to variations in estimated parameters using initial conditions from run 3. Parameters values, except the acclimation rate, were varied by two standard deviations around the mean of estimated parameters.....	33
<b>Figure 4.1.</b> Diagram of continuous flow cell bioreactor. <b>A.</b> Sterile air. <b>B.</b> Two parallel reactors for each condition was set up, except for the validation run where both reactors were operated under control conditions. <b>C.</b> Silicone tubing split with T-pieces. <b>D.</b> 12 channel peristaltic pump. <b>E.</b> Bubble traps. <b>F.</b> Flow cells.....	34

- Figure 4.2.** 2-Dimensional representation of computation domain of biofilm IbM. Particulate components (heterotrophs, autotrophs, EPS) are represented by agents while dissolved components (oxygen) are represented by a continuum.....40
- Figure 4.3.** Confocal laser photomicrographs of biofilm depicting steps in processing CLSM image stacks prior to parameter calculations. **A.** Raw image. **B.** Median filtered. **C.** Thresholded. **D.** Binarised: white represents biomass, black represents background. All parameters were calculated for binary images, except for total biomass which utilised the range in pixel values in C.....45
- Figure 4.4.** Representative confocal laser photomicrographs of multispecies biofilm development at **A.** 26.5, **B.** 45.5, **C.** 70.5, and **D.** 94.5 hours of growth under control conditions. Shown is orthogonal view where central plots are top views while upper and right frames are vertical sections through the biofilm at positions indicated by the white triangles. Scale bars are also valid for upper and right frames.....47
- Figure 4.5.** Simulated biofilm at **A.** 24, **B.** 48, **C.** 72, and **D.** 96 hours of growth. Images are perspective projections of the 3D computational domain of the iDyNoMiCS model. Blue particles represents lumped heterotrophs, green represents heterotroph EPS, red represents autotrophs, and yellow represents autotroph EPS.....48
- Figure 4.6.** Comparison between experimental and simulated biofilm parameters for biofilms cultivated under control conditions. **A.** Mean thickness. **B.** Total biomass per substratum area. **C.** Roughness coefficient. **D.** Substratum coverage. **E.** Surface area/biovolume ratio. Experimental time points are at 26.5, 45.5, 70.5, and 94.5 h. Error bars indicate 1 standard deviation.....50
- Figure 4.7.** Response of batch culture following 32 h exposure to DCF at 0.005 and 5 mg.L<sup>-1</sup>. There is no significant difference between control and treatments.....51
- Figure 4.8.** Representative confocal laser photomicrographs of multispecies biofilm structure after 4 d of growth. **A.** Control. **B.** Following 24 h exposure to 10 mg.L<sup>-1</sup> DCF. **C.** Following 24 h exposure to 0.1 mg.L<sup>-1</sup> DCF. **D.** Presumptive protists (white arrows) grazing on biofilm. Shown is orthogonal view where central plots are top views while upper and right frames are vertical sections through the biofilm at positions indicated by the white triangles. Scale bars are also valid for upper and right frames.....52
- Figure 4.9.** Experimental structure parameters of biofilm exposed to 10 mg.L<sup>-1</sup> diclofenac compared to control. **A.** Mean thickness. **B.** Total biomass per substratum area. **C.** Roughness coefficient. **D.** Substratum coverage. **E.** Surface area/biovolume ratio. The first control measurement was taken immediately after exposure of 72 h old biofilms to diclofenac. Each data point represents the average of the respective parameter. Error bars indicate 1 standard deviation. Data was shifted by 0.5 h to avoid overlap of error bars.....53
- Figure 4.10.** Experimental structure parameters of biofilm exposed to 0.1 mg.L<sup>-1</sup> diclofenac compared to control. **A.** Mean thickness. **B.** Total biomass per substratum area. **C.** Roughness coefficient. **D.** Substratum coverage. **E.** Surface area/biovolume ratio. The first control measurement was taken immediately after exposure of 72 h old biofilms to

diclofenac. Each data point represents the average of the respective parameter. Error bars indicate 1 standard deviation. Data was shifted by 0.5 h to avoid overlap of error bars.....54

**Figure 4.11.** Concentration of DCF in the influent and effluent of flow cells from the  $0.1 \text{ mg.L}^{-1}$  treatment run. Indicated is the time elapsed from DCF exposure to 72 h old biofilms. There was no significant difference between and within influent and effluent measurements.....55

**Figure 4.12.** Experimental and simulated biofilm structural parameters for control and treatment at  $10 \text{ mg.L}^{-1}$  DCF. **A.** Mean thickness. **B.** Total biomass per substratum area. **C.** Roughness coefficient. **D.** Substratum coverage. Diclofenac was introduced at 72 h (indicated by dotted line).....56

**Figure 4.13.** Experimental and simulated biofilm structural parameters for control and treatment at  $0.1 \text{ mg.L}^{-1}$  DCF. **A.** Mean thickness. **B.** Total biomass. **C.** Roughness coefficient. **D.** Substratum coverage. DCF was introduced at 72 h (indicated by dotted line).....57

**Figure 4.14.** Fold change in structural parameters of biofilms after 24 h of exposure to **A.**  $10 \text{ mg.L}^{-1}$  and **B.**  $0.1 \text{ mg.L}^{-1}$  DCF. Exposure began after 72 h of biofilm growth under control conditions. The dotted line represents the control.....58

**Figure A1.** Example calculation of OUR. Shown is the DO profile from a measurement in run 3. The slope of the DO profile gives the OUR. Only the slope above  $1.5 \text{ mgO}_2.\text{L}^{-1}$  is considered to avoid anaerobic conditions. Here,  $\text{OUR} = 0.6723 \text{ mgO}_2.\text{L}^{-1}\text{min}^{-1}$ .....81

**Figure A2.** Residual error plots for nonlinear regression of batch model to response variables for three experimental repeats.....82

**Figure C1.** Biofilm parameter scatter plot measured for biofilms cultivated under control conditions. **A.** Mean thickness. **B.** Total biomass per substratum area. **C.** Roughness coefficient. **D.** Substratum coverage. **E.** Surface area/biovolume ratio. Individual points indicate each measurement, including outliers, from duplicate flow chambers over time points. The mean and standard deviation are indicated.....84

**Figure C2.** Experimental and simulated biofilm structural parameters for control and treatment at  $0.1 \text{ mg.L}^{-1}$  DCF. For the treatment simulation an increase in substrate ( $S_s$ ), attributed to DCF, was implemented. **A.** Mean thickness. **B.** Total biomass. **C.** Roughness coefficient. **D.** Substratum coverage. DCF was introduced at 72 h (indicated by dotted line).....85

**Figure D1.** Sensitivity of structural parameters to stochastic effects. Four simulations were run using different seed values for the random number generator.....86

**Figure D2.** Sensitivity of structural parameters to changes in simulation inoculation numbers. Simulations were initiated with the indicated number of particles.....86

**Figure D3.** Sensitivity of structural parameters to changes in the value of detachment coefficient ( $k_{\text{Det}}$ ).....87

## LIST OF TABLES

<b>Table 3.1.</b> Composition of modified synthetic waste water medium.....	20
<b>Table 3.2.</b> Stoichiometric matrix describing the batch reactor.....	24
<b>Table 3.3.</b> Parameter values used for batch reactor model.....	24
<b>Table 3.4.</b> Initial guess combinations and boundary conditions used as inputs for the LSQ function.....	26
<b>Table 3.5.</b> Biokinetic parameter values estimated for three experimental repeats.....	30
<b>Table 3.6.</b> Literature kinetic parameters values at neutral pH and 20°C.....	32
<b>Table 4.1.</b> Parameters used for biofilm model simulations.....	42
<b>Table 4.2.</b> Stoichiometric matrix and kinetic expressions used for the biofilm model.....	43
<b>Table 4.3.</b> Input parameters for biofilm simulations.....	44
<b>Table A1.</b> Results of determination of decay coefficient of heterotrophic biomass in batch reactors. Shown are the results for three independent repeats performed in duplicate.....	81
<b>Table A2.</b> Initial conditions for batch reactors used to estimate biokinetic parameters.....	81
<b>Table A3.</b> Fitting statistics resulting from parameter optimisation procedure.....	82
<b>Table A4.</b> Biokinetic parameter values estimated for three experimental repeats. For each run the 95% confidence intervals are indicated.....	82

## NOMENCLATURE

Symbol	Definition	Unit
$\mu_{\max,i}$	Maximum specific growth rate of species $i$ on substrate	$\text{h}^{-1}$
$\mu_{\text{DCF}}$	Maximum specific growth rate on diclofenac	$\text{h}^{-1}$
$A_{\text{substratum}}$	Area of substratum of biofilm domain or confocal micrograph scan area	$\mu\text{m}^2$
$B$	Total biomass per substratum area of the biofilm	$\mu\text{g} \cdot \mu\text{m}^{-2}$
$b_i$	Decay coefficient for species $i$	$\text{h}^{-1}$
$b_{\text{res},i}$	Endogenous respiration rate for species $i$	$\text{h}^{-1}$
$c_f$	Substratum coverage	%
$C_{x,y,z}$	Concentration of biomass in the computation domain at coordinates $x,y,z$	$\text{mg.L}^{-1}$
$D$	Dilution rate of flow cell bioreactor	$\text{h}^{-1}$
$D_f$	Biofilm diffusivity factor	-
$D_i$	Diffusivity of solute $i$	$\text{m}^2.\text{d}^{-1}$
$f_{A,\text{H}}$	Fraction of active heterotrophic biomass	-
$f_B$	Fraction of readily biodegradable soluble substrate	-
$f_D$	Fraction of biomass leading to debris	-
$f_{\text{XI}}$	Fraction of biomass yielding particulate products	-
$gv_{i,j,k}$	Greyvalue of voxel at pixel $i,j,k$ on 3D matrix of confocal image stack	-
$K_b$	Coefficient for switching function for decay	-
$k_{\text{Det}}$	Erosion strength	$\text{fg} \cdot \mu\text{m}^{-4} \cdot \text{h}^{-1}$
$k_h$	Maximum specific hydrolysis rate	$\text{h}^{-1}$
$K_i$	Half-saturation coefficient for solute $i$	$\text{mg}_{\text{COD}} \cdot \text{L}^{-1}$
$K_{\text{I,DCF}}$	Inhibition constant for diclofenac	$\text{mg}_{\text{DCF}} \cdot \text{L}^{-1}$
$K_X$	Half-saturation coefficient for hydrolysis of slowly biodegradable substrate	$\text{mg}_{\text{COD}} \cdot \text{mg}_{\text{COD}}^{-1}$
$\bar{L}_f$	Mean biofilm thickness	$\mu\text{m}$
$L_{f,\text{max}}$	Maximum biofilm thickness	$\mu\text{m}$
$L_L$	Mass transfer boundary layer thickness	$\mu\text{m}$
$n_{X,i,t0}$	Number of particles of species $i$ used to initiate biofilm simulations	-
$R_a$	Roughness coefficient	-
$s/v$	Surface area-to-biovolume ratio of biofilm	$\mu\text{m}^2 \cdot \mu\text{m}^{-3}$
$S_{\text{in},i}$	Bulk compartment influent concentration of solute $i$	$\text{mg}_{\text{COD}} \cdot \text{L}^{-1}$
$S_I$	Concentration of inert substrate	$\text{mg}_{\text{COD}} \cdot \text{L}^{-1}$
$S_O$	Concentration of dissolved oxygen	$\text{mgO}_2 \cdot \text{L}^{-1}$
$S_s$	Concentration of soluble biodegradable substrate	$\text{mg}_{\text{COD}} \cdot \text{L}^{-1}$
$S_s/X_H$	Organic loading of heterotrophic biomass	$\text{mg}_{\text{COD}} \cdot \text{mg}_{\text{COD}}^{-1}$
$S_T$	Concentration of total soluble substrate	$\text{mg}_{\text{COD}} \cdot \text{L}^{-1}$
$t_0$	Start point of measurement	$\text{h}$
$t_i$	Time at any given moment $i$	$\text{h}$

$X_i$	Concentration of species $i$	$\text{mgCOD.L}^{-1}$
$X_I$	Concentration of inert biomass	$\text{mgCOD.L}^{-1}$
$X_S$	Slowly biodegradable substrate	$\text{mgCOD.L}^{-1}$
$Y_i$	Yield of biomass produced on substrate utilized for species $i$	$\text{mgCOD.mgCOD}^{-1}$
$Y_E$	Yield of EPS produced on substrate utilized	$\text{mgCOD.mgCOD}^{-1}$
$V_{\text{voxel}}$	Volume of a voxel on 3D matrix of confocal image stack	$\mu\text{m}^3$
$\alpha$	Acclimation constant for heterotrophic biomass	-
$\rho_i$	Density of particulate component $i$	$\text{mg.L}^{-1}$
$\sigma_R$	Specific area of flow cell bioreactor	$\text{m}^2.\text{m}^{-3}$

## ABBREVIATIONS

Acronym	Definition	Unit
A	Autotrophic bacteria	
AS	Activated sludge	
ATU	N-Allylthiourea	
CA	Cellular automaton	
CAF	Central analytic facility	
CFU	Colony forming units	
CI	Confidence interval	
CLSM	Confocal laser scanning microscopy	
COD	Chemical oxygen demand	mg <sub>COD</sub> .L <sup>-1</sup>
CV	Coefficient of variation	
DCF	Diclofenac	
DO	Dissolved oxygen	mgO <sub>2</sub> .L <sup>-1</sup>
EPS	Extracellular polymeric matrix	
FISH	Fluorescent <i>in situ</i> hybridisation	
H	Heterotrophic bacteria	
HPC	High performance computing (cluster)	
HPLC	High performance liquid chromatography	
IbM	Individual-based model	
iDyNoMiCS	Individual-based dynamics of microbial communities simulator	
LCMS	Liquid chromatography – mass spectrometry	
LSQ	Non-linear least-squares regression function	
MIC	Minimum inhibitory concentration	
MP	Micropollutant	
NSAID	Non-steroidal anti-inflammatory drug	
OD	Optical density	
OUR	Oxygen uptake rate	mgO <sub>2</sub> .L <sup>-1</sup> .h <sup>-1</sup>
PBS	Phosphate-buffered saline	
PFA	Paraformaldehyde	
PI	Prediction interval	
SD	Standard deviation	
SPE	Solid phase extraction	
SSE	Sum of squared errors	
SW	Synthetic wastewater (medium)	
TSS	Total suspended solids (cell dry weight)	mg <sub>COD</sub> .L <sup>-1</sup>
WWTP	Wastewater treatment plant	

## CHAPTER 1: INTRODUCTION

Micropollutants (MPs) are emerging contaminants found to persist globally in surface waters and have received considerable attention in recent years. Although detected at relatively low levels, many are not efficiently removed during wastewater treatment which creates health risks and compromises the safe reuse of water resources (Petrie *et al.*, 2015). With an ever-growing human population, increasing dependency on pharmaceuticals, and the recent drought in South Africa, the mass load of MPs in receiving water bodies is expected to rise. This poses a major challenge to existing wastewater treatment plants (WWTPs) and is a growing concern for the environment. Diclofenac (DCF) is a non-steroidal anti-inflammatory drug (NSAID) that has been shown to be persistent and bioactive, and is commonly detected in South African surface waters (Archer *et al.*, 2017a). DCF has been added to the first watch list of the European Union Water Framework Directive tasked with identifying compounds with suspected risk to the aquatic environment (EU, 2015). Studies indicate that DCF has a range of harmful effects on the environment, is not easily biodegradable, and has the potential to bioaccumulate (Bonnefille *et al.*, 2018). Moreover, the antimicrobial nature of DCF poses a threat to microbial diversity and functioning in both natural and engineered environments (Lawrence *et al.*, 2012). Despite numerous reviews concerning the presence of MPs in WWTPs, the microbiological basis of MP exposure in water bodies is not completely understood.

Microbial biofilms are ubiquitous in the environment and contribute significantly to the functioning of natural ecosystems as well as engineered settings such as WWTPs. Thus, they represent ideal indicators of environmental change and toxicity. A biofilm is defined as a surface-attached microbial community embedded within a self-produced extracellular polymeric substance (EPS) (Costerton *et al.*, 1995). Today, biofilms are generally well characterised, yet further investigations are still required to fully understand and take advantage of the complexity of these systems. Biofilms within WWTPs come into contact with a myriad of MPs, yet our current understanding of biofilm-MP interactions in this context is poor. What is the fate of MPs that come into contact with biofilms? And what impact, if any, does MP exposure have on biofilm activity and structure?

Structure, in a morphological sense, is an important factor to consider when studying microbial biofilms. The development of biofilm structure, which can vary from uniform to complex architectures, is affected by many internal and external factors, and can influence the activity of the biofilm itself. Therefore, changes in biofilm structure is a useful indicator of the effect of MPs on a biofilm and its activity. Investigating biofilm structure and biofilm-MP

interactions experimentally is laborious and difficult to comprehend given the vast number of processes and variables involved. Mathematical modelling can, however, integrate numerous processes in a highly controlled manner, making it a useful tool for testing hypotheses about biofilm-MP interactions.

Mathematical models have been used since the 1970s to improve our understanding of microbial biofilms. Since then, the field has progressed to a point where one can confidently model highly detailed, three-dimensional (3D) descriptions of biofilm structure and ecology (Wanner *et al.*, 2006). Various modelling frameworks have been developed to describe biofilms, with individual-based models (IbMs) showing great potential in capturing the structural complexity of microbial biofilms. A leading implementation of IbMs in the context of microbiology is iDyNoMiCS (Lardon *et al.*, 2011). The defining feature of IbMs is that they treat biomass components as individual physical entities that act independently according to rule-based behaviour. As a result, biofilm structure is an emergent property resulting from interactions at the individual scale. This represents the closest attempt at modelling biofilm dynamics from first principles and, currently, appears to be the best approach for simulating biofilm structural development. To take full advantage of the predictive power of IbMs, an improved integration of mathematical models and experimental methods is required.

Advances in confocal microscopy have allowed for the detailed, *in situ*, 3D analysis of biofilm structure development over time. Quantitative descriptors of various aspects of biofilm structure can also be derived from confocal datasets. IbM output can be analysed in a similar manner since biofilm growth is simulated in a 3D space. It follows that observed biofilm structure be used for the validation of biofilm IbMs. This idea was introduced by Xavier *et al.* (2004), but no further research has been conducted on this topic. The feasibility of this approach will be investigated, optimised, and extended to capture the effect of pollutant exposure on emergent biofilm structure.

In the present study, the effect of a commonly detected MP, diclofenac, on the structure and development of a mixed-species biofilm community was examined in a flow cell system. A high concentration of  $10 \text{ mg.L}^{-1}$  and an environmentally relevant concentration of  $0.1 \text{ mg.L}^{-1}$  was tested. Furthermore, an IbM was developed and validated in order to simulate biofilm structure development and the impact of DCF exposure. Essentially, this model was used as a tool for testing hypotheses on biofilm-MP interactions. The proposed project also investigated the feasibility of the use of observed biofilm structure for the validation of an IbM.

## CHAPTER 2: LITERATURE REVIEW

### 2.1 Bacterial biofilms

Mathematical modelling of biofilms is a widely accepted tool in fundamental biofilm research and in engineering applications. A validated model can be used to make predictions of the dynamics of a biofilm system under conditions not yet explored experimentally or those that are difficult to measure directly (Hellweger *et al.*, 2016). Building a mathematical model of a biofilm is a test of the conceptual understanding of the fundamental biological and physicochemical mechanisms governing biofilm dynamics, and can often expose gaps in the knowledge and inform the design of further experiments. Before delving deeper into biofilm modelling, it is necessary to understand the biology that the model is representing.

#### 2.1.1 What is a biofilm?

Bacteria may exist in the familiar free-floating, planktonic state or as part of dense microbial communities called biofilms (Donlan, 2002). The latter is in fact the dominant mode of microbial existence, with the planktonic fraction constituting less than 0.1% of aquatic microbial life (Costerton *et al.*, 1995). Biofilms are ubiquitous in the environment, occurring at solid-liquid or even air-liquid interfaces where conditions support microbial growth. A biofilm is defined as a spatially organised, surface-attached microbial community embedded within a self-produced EPS, or extracellular matrix (Costerton *et al.*, 1995). The EPS is mainly polysaccharide in nature, but may also contain extracellular DNA, proteins, glycoproteins, and glycolipids that contribute to the structural integrity and three-dimensional architecture of the biofilm matrix (Costerton *et al.*, 1995, Sutherland, 2001, Donlan, 2002). The EPS mediates strong attachment to various surfaces, including biological tissues, tooth surfaces, medical devices, natural aquatic systems, and water pipes (Donlan, 2002). This mode of growth confers a competitive advantage to the resident bacteria over their planktonic counterparts, allowing access to nutrients in areas with high fluid flow and harsh environmental conditions, as well as providing protection against external predation and antimicrobial treatment (Costerton *et al.*, 1995).

Biofilm complexity can vary dramatically; those grown in the laboratory are usually monocultures, whereas natural biofilms are usually made up of a consortium of diverse bacterial species, including archaea and eukaryotes. As a result, biofilm functional diversity varies as well. Biofilms play an ecologically important role in the environment and human society, most notably in the nitrogen cycle and bioremediation of wastewater. During the

biological treatment stage of water and wastewater, biofilms are key for nutrient and chemical oxygen demand (COD) removal during aerobic and anaerobic processes. On the other hand, biofilms also cause major health and economic problems for society. The biofilm matrix confers an intrinsic phenotypic tolerance to antimicrobial agents, making biofilm-associated infections particularly difficult to treat. It has been reported that the minimum inhibitory concentration (MIC) of antimicrobials required to treat biofilms can be up to 1000-fold higher than their planktonic counterparts (Høiby *et al.*, 2010). Biofilms are often responsible for chronic, and sometimes fatal, bacterial infections such as tuberculosis and urinary tract infections. Moreover, the biofouling and corrosion of water pipes, shipping equipment and membrane systems leads to huge economic losses worldwide (Schultz *et al.*, 2011). Because of the major impact of microbial biofilms on human society, research interest in biofilm formation and control is increasing.

### 2.1.2 Biofilm formation

Biofilm formation is a multistage process (Figure 2.1). Initially, planktonic bacteria attach to a pre-conditioned surface. Bacterial contact with a surface triggers a transition to a sessile state which involves a change in the gene expression profile. Surface-attached cells begin to grow and produce the EPS matrix to form microcolonies.



**Figure 2.1.** Stages of the biofilm lifecycle. Planktonic bacteria encounter a suitable surface and initiate reversible adhesion. Eventually, irreversible adhesion takes place, followed by the growth and formation of microcolonies. Finally, a mature biofilm develops and detachment events occur to seed new biofilms. Reprinted with permission (Copyright Centre for Biofilm Engineering, Montana State University-Bozeman).

Bacteria within biofilms exhibit an altered phenotype and a gene transcription profile distinct from that of planktonic bacteria (Davies and Geesey, 1995, Becker *et al.*, 2001). Cell-to-cell signalling, known as quorum sensing, facilitates bacterial community behaviour and is

involved in biofilm formation and other virulence factors. Quorum sensing allows bacteria to effect synchronised changes in population-wide gene expression based on perceived population density (Miller and Bassler, 2001).

As the biofilm thickens and matures, it eventually reaches a pseudo-steady state where growth is balanced by loss through detachment and erosion. Detachment may occur due to mechanical stress induced by bulk liquid hydrodynamics, self-induced dispersal, as well as loss due to predation and viruses (Klapper and Dockery, 2010). When conditions become unfavourable, self-induced dispersal from the biofilm allows for the colonisation of surfaces elsewhere (Donlan, 2002). It should be noted that the stages of biofilm formation described above are not discrete, rather, the processes overlap. For example, detachment, whether self-induced or otherwise, has been shown to occur throughout biofilm development (Bester *et al.*, 2009). As the biofilm increases in density and size, physical realities such as diffusion-reaction limitations begin to play an important role in biofilm structure, activity, and composition.

### 2.1.3 Factors influencing biofilm structure

Biofilm structure is dynamic and heterogeneous in nature, constantly changing in space and time as a result of external and internal factors. The structure of biofilms can vary from uniform monolayers to thick, complex architectures (Figure 2.2). The development of biofilm structure results from an interplay of physicochemical and biological factors, including mass transfer limitations, the hydrodynamics of the bulk liquid, as well as ecological interactions such as competition and cooperation (Klapper and Dockery, 2010).

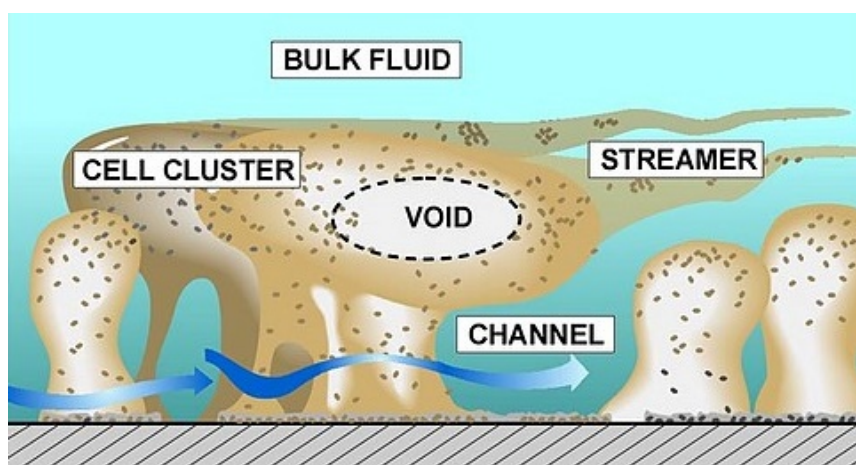


**Figure 2.2.** Illustration of biofilm structural heterogeneity. Biofilms can develop complex architectures such as water channels, mushroom-like microcolonies, and streamers. Reprinted with permission (Copyright Centre for Biofilm Engineering, Montana State University-Bozeman).

Mass transfer is an important process in biofilms due to the diffusion-limiting EPS matrix (Klapper and Dockery, 2010). In the bulk liquid, and assuming dynamic conditions, advection is the predominant solute transport process, resulting in a relatively well-mixed system. However, high cellular density and the EPS matrix limits advective transport within biofilms (Stewart, 2003). Rather, molecular diffusion is the governing solute transport process within biofilms (Zhang and Bishop, 1994). Mass transfer within the biofilm is also affected by the properties and composition of the EPS, the diffusive and reactive properties of the solute, abiotic particles, the density and spatial organisation of microbial cells, and their metabolic activity (Stewart, 2003).

Compared to a uniform biofilm surface, complex architectures such as water channels, voids and mushroom-like protrusions (Figure 2.2) have different mass transfer characteristics. These increase turbulence and provide more surface area for diffusion into the biofilm, and consequently, better access to bulk liquid nutrients (Costerton *et al.*, 1995, Eberl *et al.*, 2001). Bulk liquid can flow through these channels and between protrusions, increasing the diffusion of nutrients and oxygen into the biofilm and metabolites out of the biofilm (Donlan, 2002). Although water channels increase local mass transfer, diffusion is still limited towards the centre of cell clusters (Stewart, 2003). Pores and channels do not contribute to global mass transfer significantly, even at high flow rates. This is because high flow rates promote the formation of compact biofilms due to increased detachment forces, making the potential increase in mass transfer negligible (Van Loosdrecht *et al.*, 2002).

As the biofilm thickens, a concentration gradient is established due to diffusion limitations outlined above. In addition, microbial activity within biofilms alters the internal chemical environment by consuming substrate and producing metabolites, further accentuating the concentration gradient (Stewart and Franklin, 2008). As a result, different microenvironments develop that bacteria respond and adapt to, and a complex, spatially organised microbial community gradually develops. This generally leads to an outer aerobic and metabolically active layer, while inner layers become anaerobic, nutrient-deficient and growth-limiting (Stewart and Franklin, 2008). Bacteria at the surface of biofilms have better access to oxygen and nutrients which in turn results in relatively faster growth near the surface of the biofilm than the base biofilm. This explains the tendency of rapid outgrowth of biofilm protrusions reported in experimental studies (Costerton *et al.*, 1995, Eberl *et al.*, 2001, Ghanbari *et al.*, 2016) and reproduced by several modelling studies (Eberl *et al.*, 2001, Dockery and Klapper, 2002, Miller *et al.*, 2012).

The development of chemical gradient-induced microenvironments results in the localisation of different functional groups throughout the biofilm, which explains the coexistence of metabolically diverse species often observed in natural biofilm systems (Stewart and Franklin, 2008). Physiological cooperation between functionally different bacterial groups produces close spatial arrangements, such as those formed between ammonia and nitrite oxidisers in nitrifying biofilms (Picioreanu *et al.*, 2000b). Thus, biofilm ecology and metabolism are influenced by substrate gradients, further enhancing structural heterogeneity.

The hydrodynamics of the bulk liquid can be a major factor influencing biofilm structure as it dictates transport of nutrients as well as shear forces acting on the biofilm surface. To a large extent, biofilm formation and structure at steady-state depends on the balance between fluid shear rate (detachment) and substrate loading rate (growth rate) (Picioreanu *et al.*, 2000b). Higher substrate loading rates promote thicker biofilms due to increased mass transfer and associated faster growth, while higher shear rates promote thinner, denser biofilms (Picioreanu *et al.*, 2000b, Van Loosdrecht *et al.*, 2002). Erosion and sloughing are the two main detachment processes. Erosion refers to the continuous detachment of single cells or small clusters, whereas sloughing is the more random, rapid, and often larger loss of biofilm (Donlan, 2002). Systems with higher shear forces, where detachment occurs mainly by erosion, tend to create thin, compact biofilms. Sloughing is predominant in systems with lower shear forces, leading to a more heterogeneous and porous biofilm (Van Loosdrecht *et al.*, 2002, Xavier *et al.*, 2005b). However, the reader is reminded that biofilm structure depends on the interplay between multiple factors; low shear forces does not necessarily always lead to a heterogeneous biofilm structure. Van Loosdrecht *et al.* (2002) demonstrated that faster growing biofilms can better balance detachment in systems with higher shear forces, leading to relatively thick biofilms. One should also consider the variations in the composition of the EPS matrix which could determine a biofilms resistance to sloughing.

Detachment mechanisms have been successfully incorporated into multi-dimensional biofilm models which have been used to improve understanding of the effect of detachment on biofilm structure (Morgenroth and Wilderer, 2000, Van Loosdrecht *et al.*, 2002, Xavier *et al.*, 2005b). Based on experimental observation and the use of a cellular automaton (discussed in section 2.2.1), Van Loosdrecht *et al.* (2002) concluded that, along with substrate gradients, detachment processes play a significant role in biofilm structure as well. For example, the detachment of cell aggregates from the biofilm surface was found to be responsible for voids in the structure, leading to an irregular, porous biofilm (Figure 2.2).

In summary, biofilm structure depends on the interplay between physical, chemical and biological processes. Spatial organisation is driven by the presence of chemical gradients resulting from biological activity and diffusion limitations. Biofilm structure is ultimately constrained by the balance between bulk liquid mechanical forces and microbial growth rates. Specific microbial processes influence structure dynamics as well, including biomass yield on the rate-determining substrate and EPS production (Van Loosdrecht *et al.*, 2002). To simulate multidimensional biofilm structure, a mathematical model would need to simulate the interplay between the major physical, chemical and biological processes that occur at different spatial and temporal scales (Klapper and Dockery, 2010, Laspidou *et al.*, 2010).

#### 2.1.4 Quantifying biofilm structure

Confocal laser scanning microscopy (CLSM) has become a popular method for studying microbial biofilms and is particularly well suited for biofilm structure investigations. CLSM has the capability to provide high resolution 3D reconstructions of biofilms by capturing a series of optical sections in the same *x*-*y* plane along the *z*-axis (Lawrence *et al.*, 1991). Combined with fluorescent probes, it allows for the direct, non-destructive, *in situ* analysis of fully hydrated, living biofilms and can provide information on cell morphology and metabolism, as well as the physical structure and chemistry of the biofilm matrix (Costerton *et al.*, 1995). Compared to alternative microscopic techniques, such as scanning electron or phase-contrast microscopy, CLSM does not require harsh chemical fixation and has the beneficial feature of rejecting out-of-focus light, producing clear optical sections (Lawrence *et al.*, 1991). Thus, biofilms can be analysed at specific depths and a 3D render of the biofilm can be reconstructed.

A wide range of non-specific and specific fluorescent probes are available for CLSM analysis of biofilms, which offers a number of options for structural investigations. The non-specific nucleic acid stain, Syto9™ (a component of the LIVE/DEAD® BacLight™ kit), is widely used for general staining of the whole microbial population of single- and mixed-species biofilms. Specific probes are useful for differentiating between species or components of a biofilm. These include molecular probes commonly used in fluorescent *in situ* hybridisation (FISH) studies, and saccharide-specific fluorescent lectins that bind EPS components (Neu and Kuhlicke, 2017). However, there are certain limitations of this method to contend with, such as fluorophore bleaching and laser intensity attenuation in thick biofilms (Semechko *et al.*, 2018).

Since biofilm formation is stochastic in nature, a direct, qualitative comparison between observed and predicted structure is unsuitable (Xavier *et al.*, 2004). Therefore, quantitative parameters describing biofilm structure are derived from simulation and CLSM datasets for comparison, including mean thickness ( $\bar{L}_f$ ), biovolume ( $B$ ), roughness coefficient ( $R_a$ ), surface-to-volume (s/v) ratio, and substratum coverage ( $c_f$ ) (Heydorn *et al.*, 2000b). Quantification is based on image segmentation, where binary values are assigned to pixels with or without biomass over a given threshold value. Structural parameters have been used extensively for investigating the impact of antimicrobials and environmental conditions on biofilms as well as simulation output (Heydorn *et al.*, 2000b, Paje *et al.*, 2002, Xavier *et al.*, 2004, Lawrence *et al.*, 2007). COMSTAT, developed by Heydorn *et al.* (2000b) and improved by others (Vorregaard, 2008), is a well-known and freely accessible program used for quantitative biofilm analysis. Alternative image analysis programs have been developed such as ISA-3D (Yang *et al.*, 2000) and PHLIP (Mueller *et al.*, 2006). See Mueller *et al.* (2006) for a detailed comparison between image analysis software.

Image analysis can be challenging and tedious for large datasets. Pre-processing steps are often required to remove background noise and irregularities. These steps often require manual inspection of image stacks to decide on suitable pre-processing steps and assigning threshold values for image segmentation. There has been a considerable effort to automate image analysis, with the primary benefit of eliminating user subjectivity (Xavier *et al.*, 2001, Xavier *et al.*, 2003, Merod *et al.*, 2007, Yerly *et al.*, 2007). Yet, challenges still remain, such as inconsistent CLSM formats and how to deal with artefacts, which has prevented the development of a gold standard within the biofilm research community.

In recent years, multidimensional models of microbial biofilms have been developed that can simulate biofilm structure from the bottom up (Lardon *et al.*, 2011). Mattei *et al.* (2018) recently called for improved validation of biofilm models which would require a better integration of modelling and experimental methods. Quantitative structural parameters derived from CLSM datasets show promise to be used for the validation of multidimensional biofilm models. Xavier *et al.* (2004) introduced this approach, however, no further research has been conducted on this topic.

## 2.2 Biofilm models

Formulated in the late 1970s, the first biofilm models described a one-dimensional (1D), steady-state, single-substrate biofilm with the assumption that biofilms developed as a uniform

layer (Rittmann and McCarty, 1980, Kissel *et al.*, 1984). Soon after, time-dependent multi-substrate and multi-species biofilm models were developed, capable of describing simple microbial interactions and basic biofilm structure (Wanner and Gujer, 1986, Dockery and Klapper, 2002). However, these 1D models did not simulate the complex, multidimensional structural characteristic of mature biofilms observed by new microscopic techniques. This drove the development of two-dimensional (2D) and 3D models capable of describing biofilm structural heterogeneity (Picioreanu *et al.*, 1998a, Kreft *et al.*, 2001, Xavier *et al.*, 2005a, Alpkvist *et al.*, 2006, Wanner *et al.*, 2006), the work of Xavier and Picioreanu being particularly influential. These models require a high level of modelling expertise and are usually computationally expensive. But, often a high level of detail is not necessary, and a simplistic model is more appropriate for the question being asked. It is impractical, perhaps impossible, to incorporate all the processes occurring during biofilm development. Consequently, simplifying assumptions are usually made to reach an approximate solution within a reasonable timeframe. The choice of model complexity depends on the user's modelling experience, the biofilm system, modelling objectives, and computing power available.

The development of multidimensional biofilm models was driven by advances in experimental and microscopic techniques, molecular biology, numerical methods, as well as powerful computing hardware. Today, mathematical models can describe biofilm activity, geometry and ecology in great detail. Models have also been developed that can simulate cell-to-cell signalling, plasmid invasion, synthetic biology, and anaerobic digesters, among many other biofilm-based processes (Merkey *et al.*, 2011, Fozard *et al.*, 2012, Rudge *et al.*, 2012).

In order to simulate biofilm formation, the components that make up the biofilm must be represented mathematically. Typically, the computation domain is split into four compartments, each containing defined components (biomass and solutes) and processes (reaction-diffusion-advection kinetics) (Figure 2.3A). A mass transfer boundary layer ( $L_L$ ) usually separates the biofilm from the bulk liquid compartment (Figure 2.3B). This represents a hypothetical liquid layer above the biofilm that is known to resist mass transfer of dissolved components from the bulk liquid (Wanner *et al.*, 2006). All processes acting in each compartment are represented by mass balance equations governing mass flow into and out of the system as well as production and consumption. The key processes include (i) biomass growth and decay, (ii) biomass division and spreading, (iii) substrate reactions and transport, (iv) biomass attachment and detachment, and (v) hydrodynamics (Picioreanu *et al.*, 2004). This

modular approach of describing biofilm processes is advantageous and often necessary with increasing model complexity.

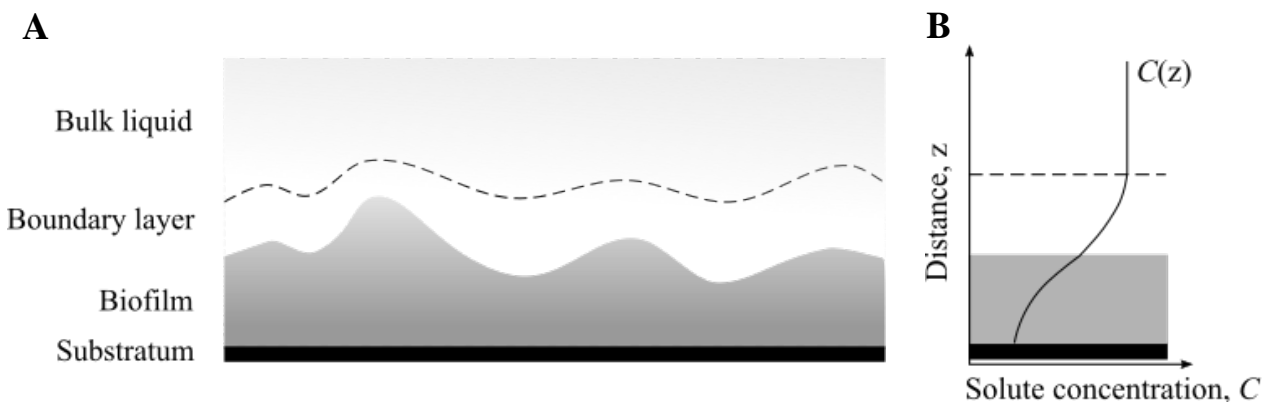


**Figure 2.3.** **A.** Compartments typically defined in biofilm models. These include the bulk liquid, mass transfer boundary layer, biofilm, and substratum. **B.** Typical mass transfer boundary layer substrate conditions. Both figures redrawn from Wanner *et al.* (2006).

Biofilm models are valuable tools for biofilm researchers, capable of integrating numerous experimental observations in a highly controlled environment. Their development tests our understanding of the underlying principles, and has the potential to inform the design of further experiments and make predictions.

### 2.2.1 Types of biofilm models

Mathematical biofilm models in literature vary from simple 1D steady-state models to more complex 2D/3D dynamic models. The IWA Task Group on Biofilm Modelling has produced an extensive review on biofilm models and their applications (Wanner *et al.*, 2006). Models can be solved by analytical, pseudo-analytical, or numerical methods depending on the complexity of the model description. There are three broad categories of biofilm models that differ in the way particulate components (biomass) are represented (Figure 2.4).

Early biofilm models represented biomass as a continuum with population-averaged behaviour described by ordinary and partial differential equations (Wanner and Gujer, 1986, Eberl *et al.*, 2001). Although 1D models provide a simple solution to diffusion-reactions problems, they fail to capture the structural complexity frequently observed in biofilms, such as water channels and protrusions (Figure 2.2), that can only be simulated by multidimensional models. Structure-function dynamics are an important process in microbial biofilms that 1D models cannot account for. Moreover, microenvironments that develop within biofilms may cause localised microbial behaviour to differ from population-averaged behaviour (Stewart and Franklin, 2008, Hellweger and Bucci, 2009).

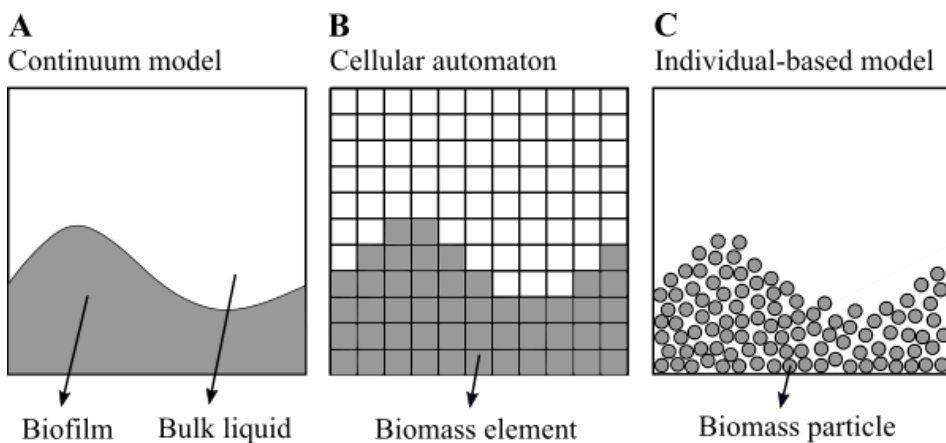


**Figure 2.4.** Three approaches for representing biomass in a biofilm model. Particulate components can be represented as: **A.** a continuum, **B.** as discrete grid-based elements, or **C.** as discrete particles. Redrawn from Wanner *et al.* (2006).

The desire to describe and predict cellular-level differences led to the development of discrete, multidimensional models that attempt to simulate biofilm formation from first principles. 2D models are also limited since the effect of adjacent structures in the third dimension are not accounted for. Although 3D simulations are computationally expensive, they provide a more realistic representation of biofilm structure, especially when structure and microbial interactions (structure-function dynamics) are being considered.

In discrete models, biomass growth kinetics are solved for each individual agent using ordinary differential equations, but biomass transport is governed by discrete particles and stochastic rule-based behaviour (Kreft *et al.*, 2001). Although multidimensional continuum models have been developed for describing biofilm spatial heterogeneity (Alpkvist and Klapper, 2007b), the results are unrealistically linear. An advantage of discrete models is the fact that the biofilm-scale dynamics and structure are an emergent property of the growth and interactions of discrete units at the individual scale. Moreover, they are capable of incorporating more complexity in terms of the physical interactions between cells. Thus, they are closer to modelling biofilms from first principles. The disadvantage of discrete models is that they are more computationally demanding. Unlike the continuum approach, which assumes a homogeneous biofilm composition, the discrete approach can capture different types of biomass components and are better suited for describing biofilm heterogeneity. There are two main types of discrete frameworks for modelling biofilm systems: cellular automata (CA) and individual-based modelling.

Cellular automata (s. cellular automaton) are popular for modelling spatial biofilm dynamics due to it being a well-established technique in the modelling community (Picioreanu *et al.*,

1998a, Picioreanu *et al.*, 1998b, Noguera *et al.*, 1999, Hermanowicz, 2001, Picioreanu *et al.*, 2001, Pizarro *et al.*, 2001, Chang *et al.*, 2003, Laspidou and Rittmann, 2004). Briefly, a CA is composed of a fine grid of cells, in which biomass can exist and grow to a pre-set maximum concentration. Distribution of biomass to neighbouring cells is governed by a set of global rules where biomass is transported to the nearest unoccupied grid cell (Figure 2.4B). An advantage of representing biomass by a grid is simplicity and computational efficiency, however, and contrary to reality, biomass transport can only occur along a finite number of directions (Wanner *et al.*, 2006).

IbMs, or agent-based models, describe biomass components as discrete, individual entities (agents) with position in space defined in continuous coordinates (Figure 2.4C) (Kreft *et al.*, 2001). Several IbMs have been developed for modelling biofilm systems (Kreft *et al.*, 1998, Kreft *et al.*, 2001, Picioreanu *et al.*, 2004, Xavier *et al.*, 2005a, Xavier *et al.*, 2007, Lardon *et al.*, 2011). IbMs are similar to CAs, except that agent movement is not restricted by a predefined grid – transport can occur in any direction and is carried out by minimising the overlap of adjacent particles. Individual agents undergo growth, division, and transport according to a set of rules. Each individual is unique and may differ in properties such as metabolic activity and biomass composition (Hellweger and Bucci, 2009). Although more computationally demanding than CAs, IbMs are closer to modelling biofilms from first principles by treating bacterial cells as the fundamental entities with adaptable behaviour. This allows individual variability to be incorporated into the model, accounting for single-cell observations and the stochastic behaviour of bacterial growth. IbMs are intrinsically better at reproducing adverse effects on emergent biofilm structure, making it an ideal framework for modelling biofilm-MP interactions. Xavier *et al.* (2004) was the first to compare predicted biofilm structure using an IbM to observed biofilms analysed using CLSM. It was found that the model was able to reproduce observed biofilm structure based on structural parameters. This combined experimental and modelling approach shows promise for investigating fundamental biofilm-MP interactions in the present study.

The first IbMs described the EPS as initially bound to the bacterial agent and then excreted as a separate agent (Kreft and Wimpenny, 2001). An alternative approach represented the EPS as a continuum coupled with an IbM for microbial cells (Alpkvist *et al.*, 2006). This was done to better represent the visco-elastic fluid nature of the EPS matrix (Klapper *et al.*, 2002, Alpkvist and Klapper, 2007a). More advanced IbMs incorporated improved detachment processes and multicomponent agents (Picioreanu *et al.*, 2004, Xavier *et al.*, 2005a, Xavier *et al.*, 2005b).

The latter introduced more variation of individuals by including components such as active and inert biomass, storage polymers, and other system-specific components which can each undergo specific conversions (Xavier *et al.*, 2005a).

For computational efficiency, IbMs usually decouple reaction-diffusion processes from biomass growth (Wanner *et al.*, 2006). These processes occur within biofilms at very different time scales. For example, the characteristic time scale for biomass growth and detachment is typically in the order of  $10^5$  sec (~1 day), while mass transport and hydrodynamic processes are up to 10 orders of magnitude faster (Picioreanu *et al.*, 2000a). Therefore, reaction-diffusion processes are typically solved at steady-state for each iteration. This approach is used in most biofilm models that simulate structure development and is not considered to compromise accuracy (Picioreanu *et al.*, 2000a, Picioreanu *et al.*, 2004, Xavier *et al.*, 2005a, Alpkvist *et al.*, 2006, Wanner *et al.*, 2006).

Progress in developing IbMs as a research and engineering tool has been hindered due to the apparent lack of a standardised model and development protocol. To address this issue, Lardon *et al.* (2011) introduced iDyNoMiCS (individual-based Dynamics of Microbial Communities Simulator) as a standardised modelling platform. iDyNoMiCS is based on the foundation and consolidated knowledge of earlier models with various improvements. To date, several studies have been published using the iDyNoMiCS platform (Merkey *et al.*, 2011). A more recent development, the NUFEB IbM, is currently the most advanced iteration of IbMs that incorporates fluid flow dynamics and density-dependent adhesion between cells – capabilities that iDyNoMiCS currently lacks (Jayathilake *et al.*, 2017). However, this model is not yet well established, whereas iDyNoMiCS is accompanied by tutorials, data processing protocols, and is relatively user-friendly. Thus, iDyNoMiCS was used for the present study.

### **2.3 Micropollutants**

Micropollutants are emerging contaminants that have received considerable attention in the past few years. MPs may enter surface waters from human, agricultural, and industrial sources as both active metabolites and in the unmetabolised form (Petrie *et al.*, 2015, Archer *et al.*, 2017a). Detected MPs include a range of pharmaceuticals and personal care products, such as antibiotics, steroids, anti-inflammatories, beta-blockers, anti-depressants, and illicit drugs. Many MPs are not efficiently removed by WWTPs, which represents a continuous source of contamination of water bodies. Limited data is available on the occurrence and persistence of MPs in South African surface waters, but there is growing evidence of their presence and potential ecological impact (Agunbiade and Moodley, 2016, Archer *et al.*, 2017a, Archer *et al.*,

2017b). Due to the large variety of MP classes detected in wastewater, their bioaccumulation and consequent impact on the environment is potentially devastating. Although detected in low concentrations, the continuous release of bioactive and persistent MPs may lead to long-term effects on ecosystems due to bioaccumulation. The issue can be magnified in periods of drought, currently an issue in South Africa, where MPs reach higher concentrations during low flow periods.

Based on a conventional environmental risk assessment, DCF was classified as an environmental risk at levels reported in South African WWTP effluent and river water (Archer *et al.*, 2017a). However, establishing MPs as an environmental risk is complicated by the fact that, in nature, MPs are found in complex mixtures of varying concentrations, and the ecotoxicity of such mixtures may differ from that of individual MPs (Galus *et al.*, 2013). Although studies involving mixtures of MPs are more ecologically relevant, investigations on individual compounds are valuable as they provide a fundamental understanding of their ecological interactions.

### 2.3.1 Diclofenac

Although complex mixtures of MPs are usually detected in WWTP effluent and river water, this case study focussed on the non-steroidal anti-inflammatory drug, DCF. DCF is among the most widely used therapeutics and is primarily used for the treatment of pain and inflammation. DCF, or 2-(2,6-dichloranilino) phenylacetic acid (Figure 2.5), acts to inhibit the activity of cyclooxygenase enzymes, thereby blocking the synthesis of prostaglandins which act to activate an inflammatory response (Dannhardt and Kiefer, 2001).

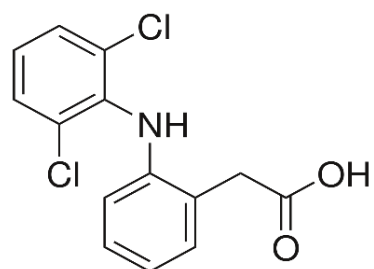


**Figure 2.5.** Molecular structure of diclofenac.

DCF is frequently detected in South African surface waters at levels ranging between 0.3-15.6 µg.L<sup>-1</sup> and in wastewater influent at 2.7-222 µg.L<sup>-1</sup> (Agunbiade and Moodley, 2016, Archer *et al.*, 2017a). DCF has also been reported to be highly persistent, with relatively low removal efficiencies. A recent study on MP occurrence in Gauteng, South Africa reported a

DCF removal efficiency of only 47% during wastewater treatment (Archer *et al.*, 2017a) which is in the range of removal efficiencies reported elsewhere (Petrie *et al.*, 2015, Jiang *et al.*, 2017).

There is growing evidence of the ecotoxicological impact of DCF on the environment at multiple trophic levels. DCF has been reported to modulate reproductive endocrine pathways in fish at levels as low as  $1 \mu\text{g.L}^{-1}$  (Hong *et al.*, 2007). DCF is often detected in surface waters above this level which poses a risk to receiving fish populations and potentially other vertebrate species (Archer *et al.*, 2017a, Gröner *et al.*, 2017). Furthermore, DCF treatment decreases thyroid hormone levels in human patients (Bishnoi *et al.*, 1994). Although this occurred at prescription level doses, it indicates a potential health risk for humans and other larger vertebrates that come into contact with contaminated water. The persistence of DCF can lead to bioaccumulation and magnified effects up the food chain. In an extreme case, the consumption of DCF-treated livestock carcasses led to a catastrophic decline (>95%) in a particular vulture population that was unable to metabolise DCF (Oaks *et al.*, 2004). A recent review has documented further detrimental effects of DCF in marine environments worldwide (Bonnefille *et al.*, 2018). Although studies on the ecological impact of DCF are rising, the full extent of the potential damage is poorly understood. Toxicity studies have mainly focussed on eukaryotic organisms, but more research on the effects on prokaryotes are also required.

### **2.3.2 Effect on microbial biofilms**

The majority of studies in literature focus on single-species evaluations of MP toxicity which has been suggested to be insufficient for accurate environmental risk assessments (Lawrence *et al.*, 2012). Few studies have looked at the effects of MPs on real ecosystems, and even fewer on microbial biofilms. Therefore, in the present study, the effect of DCF exposure on a mixed-species environmental sample was evaluated.

DCF has been found to exhibit broad-spectrum *in vitro* and *in vivo* antibacterial activity against a range of Gram-positive and Gram-negative bacteria (Annadurai *et al.*, 1998, Dastidar *et al.*, 2000, Mazumdar *et al.*, 2006, Dutta *et al.*, 2007, Dutta *et al.*, 2008, Mazumdar *et al.*, 2009). In fact, DCF has been reported to improve bacterial killing when used in combination with antibiotics and has been suggested for augmenting the treatment of antimicrobial-resistant infections (Mazumdar *et al.*, 2009). The MIC of DCF has been reported between  $5\text{-}100 \text{ mg.L}^{-1}$  for Gram-positive bacteria and  $5\text{-}500 \text{ mg.L}^{-1}$  for Gram-negative bacteria (Dastidar *et al.*, 2000, Mazumdar *et al.*, 2009). It was also suggested that the antibacterial action of DCF was due to the inhibition of bacterial DNA synthesis, however, the mechanism of DNA synthesis inhibition was unclear (Dastidar *et al.*, 2000). Subsequent studies demonstrated the

inhibition of thymidine precursor incorporation into DNA as well as moderate membrane damage of *Listeria* spp. when exposed to 200 mg.L<sup>-1</sup> DCF (Dutta *et al.*, 2007, Dutta *et al.*, 2008). There appears to be multiple modes of action exhibited by DCF which explains its broad-spectrum antimicrobial activity.

Microbial biofilms are also susceptible to DCF exposure, although at much higher concentrations than planktonic MICs (Paje *et al.*, 2002, Abbas *et al.*, 2012, Reśliński *et al.*, 2015). Abbas *et al.* (2012) reported a minimum biofilm inhibitory concentration of 3125 mg.L<sup>-1</sup> DCF against *Pseudomonas aeruginosa*. Lower concentrations of DCF, between 5-1000 µg.L<sup>-1</sup>, appear to be sub-inhibitory, but system-dependent (Paje *et al.*, 2002, Lawrence *et al.*, 2007, Lawrence *et al.*, 2012, Reśliński *et al.*, 2015). Besides inhibiting DNA synthesis, studies have indicated that DCF may limit biofilm adhesion to the substratum, reduce microbial carbon utilisation, as well as cause shifts in biodiversity (Lawrence *et al.*, 2007, Lawrence *et al.*, 2012, Reśliński *et al.*, 2015). Paje *et al.* (2002) observed a 70% reduction in biofilm biomass after 4 weeks of exposure to 100 µg.L<sup>-1</sup> DCF. Lawrence *et al.* (2012) reported a significant decrease in the algal and bacterial biomass, as well as biodiversity of mixed-species biofilms when exposed to 5 µg.L<sup>-1</sup>. Carbon utilisation of multiple compounds, particularly carbohydrates, was also significantly depressed. The impact of DCF exposure on microbial diversity and carbon source utilisation may be detrimental to WWTP performance.

There is evidence that microbial biofilms can metabolise DCF, although acclimation and enrichment for DCF-degraders is usually required (Paje *et al.*, 2002, Falas *et al.*, 2013, Jewell *et al.*, 2016). Paje *et al.* (2002) found that DCF removal efficiency increased from 20% to 97% after 10 weeks of acclimation. There is also the possibility that it can be used directly as a carbon source where biodegradation studies have reported cultures surviving on DCF as the sole carbon source (Bessa *et al.*, 2017). This indicates that the presence of DCF at environmentally relevant concentrations could apply a selective pressure on microbial biofilms and consequently alter their overall activity. This may prove insightful for the enrichment of biofilm reactors designed for the removal of DCF. Biodegradation of DCF has been reported to result in a large range of transformation products involving several degradation pathways (Jewell *et al.*, 2016). Toxicity tests usually stick to the parent compound, but the effect of metabolites of MPs on the environment should also be considered since they may exhibit higher toxicity than that of their parent compound, as has been shown for DCF (Diniz *et al.*, 2015, Archer *et al.*, 2017b).

The functional diversity of mixed-species biofilms makes them well suited for the remediation of wastewater containing a range of MPs. Biofilms are capable of removing MPs by sorption to the EPS and/or biodegradation through metabolic and/or co-metabolic pathways (Petropavlovskii and Sillanpää, 2013, Pomies *et al.*, 2013). The initial interaction is likely governed by the physicochemical properties of the MP and the EPS. The bioavailability and sorption to the EPS depends on the hydraulic retention time, hydrophobicity, pH, temperature, and the octanol/water partition coefficient ( $K_{ow}$ ) of the compound (Petrie *et al.*, 2015, Archer *et al.*, 2017a). DCF has a log  $K_{ow}$  of 4.51 and exhibits relatively weak partitioning into solid material which may contribute to its persistence (Petrie *et al.*, 2015). The concentration of MPs within the biofilm EPS may facilitate biodegradation by increasing the residence time of the MP, or, if biodegradation does not occur, the EPS may serve as a reservoir for MPs which may be released in higher concentrations at a later stage. The interaction between MPs and biofilms in this context requires further investigation in order to better understand the fate of MPs and improve removal rates.

The impact of biofilm-scale variations (e.g. biofilm structure) on biofilm activity and MP removal efficiency are poorly understood, but there is evidence that structure and species composition play an important role. Torresi *et al.* (2016) demonstrated the effect of biofilm thickness on the removal of 20 organic MPs in a moving bed biofilm reactor. Overall, thicker biofilms (500 µm) performed better with higher biotransformation rates than thinner biofilms. This was attributed to the higher biodiversity observed in thicker biofilms that results from microenvironments developing along diffusion gradients. However, a few MPs, including DCF, displayed better removal for thinner biofilms, which was associated with higher nitrification rates (Torresi *et al.*, 2016). Changes in biofilm structure has consequences on biofilm activity. The effect that MPs have on the structure-function relationship of biofilms is a concern for the proper functioning of environmental as well as WWTP microbial communities. Biofilm structure, and its concomitant effect on biodiversity and activity, appears to be an important factor to consider for biofilm models simulating MP interactions.

## 2.4 Research aims and objectives

The aim of the project was to develop an IbM capable of describing biofilm structural development of an environmental sample, as well as reproducing observed effects of DCF-treatment on biofilm structure. A further aim was to investigate the feasibility of the use of observed biofilm structure for the validation of an IbM. The following objectives were set to achieve these aims:

1. Calibrate the IbM by determining biokinetic parameters (lumped) of environmental samples through respirometry and regression to a batch model;
2. Define parameters and assumptions for the IbM to describe biofilm growth in a flow cell bioreactor;
3. Validate the IbM by comparing structural parameters of simulation results to observed biofilms cultured under control conditions;
4. Investigate the impact of DCF exposure at a low ( $0.1 \text{ mg.L}^{-1}$ ) and a high concentration ( $10 \text{ mg.L}^{-1}$ ) on the structure of mixed-species biofilms cultured in flow cells;
5. Investigate whether the IbM incorporating a hypothesised DCF interaction can reproduce observed effects on biofilm structure at varying concentrations.

## 2.5 Key questions

1. What is the impact of DCF exposure at varying concentrations on observed biofilm structure?
2. How viable is the use of observed biofilm structure for the validation of a biofilm IbM?
3. Can an IbM reproduce and explain observed effects of DCF exposure on biofilm structure?

## 2.6 Hypotheses

It is hypothesised that DCF exposure at  $10 \text{ mg.L}^{-1}$  will exhibit a sub-inhibitory effect on biofilm growth. It is further hypothesised that the IbM can reproduce observed effects of DCF exposure on biofilm structure.

For clarity, the methodology and results chapters are split in two. First, biokinetic parameter estimation is presented in Chapter 3, followed by the flow cell bioreactor and modelling sections in Chapter 4.

## CHAPTER 3: PARAMETER ESTIMATION

### 3.1 Materials and Methods

#### 3.1.1 Inoculum seed and cultivation

Activated sludge (AS) was sampled from the return AS tank at the Athlone WWTP, Cape Town. On the day of collection, the AS was mixed well and allowed to stand for 15 min to allow large solids to settle. Freezer stocks were made by transferring 500  $\mu\text{L}$  AS to an equivalent volume of 80% glycerol (40% final concentration). These were stored at -80°C until needed.

A modified synthetic wastewater (SW) medium was used in the batch respirometry and flow cell bioreactor experiments (Osachoff *et al.*, 2014). The chemical composition of this medium is listed in Table 3.1. The medium was made up in deionised water. The COD of this medium was approximately 300  $\text{mg}\cdot\text{L}^{-1}$ , unless otherwise stated. For the flow cell reactor feed, a concentration of 1.2  $\text{mg}\cdot\text{L}^{-1}$   $\text{FeSO}_4\cdot7\text{H}_2\text{O}$  was used to avoid blockages due to iron(III) phosphate precipitation. The pH of the autoclaved medium was approximately 9.1 which was adjusted to a pH of 7.5 for subsequent experiments.

**Table 3.1.** Composition of modified synthetic waste water medium

Synthetic waste water component	Concentration ( $\text{mg}\cdot\text{L}^{-1}$ )
Yeast extract	28
Starch ( $\text{C}_6\text{H}_{10}\text{O}_5$ ) <sub>n</sub>	96
Sodium acetate anhydrous ( $\text{NaCH}_3\text{COO}$ )	300
Monopotassium phosphate ( $\text{KH}_2\text{PO}_4$ )	22
Sodium bicarbonate ( $\text{NaHCO}_3$ )	155
Ammonium chloride ( $\text{NH}_4\text{Cl}$ )	52
Ferrous sulphate heptahydrate ( $\text{FeSO}_4\cdot7\text{H}_2\text{O}$ )	12
Magnesium chloride ( $\text{MgCl}_2\cdot6\text{H}_2\text{O}$ )	25
Calcium chloride ( $\text{CaCl}_2\cdot2\text{H}_2\text{O}$ )	37
Zinc sulphate ( $\text{ZnSO}_4\cdot7\text{H}_2\text{O}$ )	0.2

To prepare the seed inoculum, a freezer stock was allowed to thaw at room temperature and then transferred aseptically to 100 mL SW medium and incubated overnight at 26°C on a rotary shaker. The culture was then sub-cultured in 250 mL SW medium for a further 24 h to acclimatise the culture to the SW medium.

### 3.1.2 Analytical procedures

The oxygen uptake rate (OUR) was measured using an optical dissolved oxygen (DO) probe (Vernier) connected to a LabQuest Mini data logger (Vernier). Data was logged using the Logger Lite software (v1.9.4). An aliquot of culture was transferred to a 250 mL bottle and the DO probe inserted while taking care to exclude any air bubbles. The respirometer was sealed using a lid with a rubber O-ring and placed in a beaker containing water to maintain the temperature at 20°C. The culture was mixed using a magnetic stirrer. The DO was allowed to stabilise for 1 min before measurements were taken. The decrease in DO was measured for approximately 10 min.

The soluble substrate concentration ( $S_S$ ) was estimated by multiplying the measured COD (COD Cell Test, Spectroquant®) filtered through a 0.45 µm cellulose acetate filter by the readily biodegradable fraction of COD,  $f_B$ . The total suspended solids (TSS) was determined gravimetrically according to modified APHA methods (APHA, 1998). The culture was vacuum filtered through a 0.45 µm cellulose acetate filter and then dried at 60°C for 48 h. A desiccator was used to keep the filters dry at room temperature before weighing. A COD/dry mass conversion factor of 1.20 was used for recalculation of TSS mass concentration to COD units (Grady Jr *et al.*, 1999, Trojanowicz *et al.*, 2009). The active heterotroph concentration ( $X_H$ ) was estimated by multiplying the TSS by the active heterotroph fraction,  $f_{A.H}$ .

### 3.1.3 Determination of decay coefficient of heterotrophic biomass

The value of decay coefficient ( $b_H$ ) was estimated experimentally using batch respirometry according to the method described in Trojanowicz *et al.* (2009) and Grady Jr *et al.* (1999). The principle of this method is the measurement of OUR change over time during prolonged biomass aeration without external substrate addition. The OUR is then a result of biomass endogenous respiration (decay) only and the change is directly proportional to  $b_H$  (Grady Jr *et al.*, 1999, Trojanowicz *et al.*, 2009).

Seed inoculum (250 ml) was transferred to 4 L SW medium in 5 L Erlenmeyer flasks and incubated for 24 h at 26°C to achieve an endogenous respiration state of heterotrophic bacteria (until all substrate depleted). An air pump was used to aerate the culture and magnetic stirrers for mixing. The culture was then moved to room temperature (20 ± 2°C) with continued aeration and mixing for a further 5 d. Initial reading of TSS,  $S_S$  and OUR were taken to get  $X_{H,10}$ ,  $S_{S,10}$  and  $OUR_{10}$ . The OUR and optical density ( $OD_{600\text{ nm}}$ ) was measured every 6-12 h. The value of  $b_H$  was then determined as follows:

The change in  $X_H$  and rate of oxygen utilisation (in COD units) is influenced by growth and decay processes, given by equations 1-2:

$$\frac{dX_H}{dt} = \mu_{\max,H} \frac{S_S}{K_S + S_S} \frac{S_O}{K_O + S_O} X_H - b_H \frac{K_b}{K_b + S_S/X_H} X_H \quad (1)$$

$$\text{OUR} = \left( \frac{1 - f_D}{Y_H} \right) \mu_{\max,H} \frac{S_S}{K_S + S_S} \frac{S_O}{K_O + S_O} X_H + (1 - f_D) b_H \frac{K_b}{K_b + S_S/X_H} X_H \quad (2)$$

Biomass growth is governed by Monod kinetics with respect to substrates  $S_S$  and  $S_O$ . Biomass decay is governed by a switching function that depends on the ratio of  $S_S$  and  $X_H$ . The parameters are described in Table 3.3.

In a batch reactor that receives no soluble substrate and is not limited by oxygen the only reaction will be decay. Thus, the change in  $X_H$  and oxygen in the batch reactor can be simplified as eqns. 3-4:

$$\frac{dX_H}{dt} = - b_H \cdot X_H \quad (3)$$

$$\text{OUR} = (1 - f_D) b_H \cdot X_H \quad (4)$$

Integrating eq. 4 over time  $t$  gives:

$$X_H|_t = X_{H,t_0} \cdot e^{-b_H \cdot t} \quad (5)$$

Substituting eq. 5 into eq. 4 reveals the OUR in the batch reactor at any time  $t$ :

$$\text{OUR}|_t = (1 - f_D) b_H \cdot X_{H,t_0} \cdot e^{-b_H \cdot t} \quad (6)$$

Taking the natural logarithm of both sides of eq. 6 gives a linear expression (eq. 7) allowing the use of linear regression:

$$\ln(\text{OUR})|_t = \ln[(0.8 \cdot b_H) \cdot X_{H,t_0}] - b_H \cdot t \quad (7)$$

assuming  $f_D = 0.2$ , which is the fraction of biomass leading to debris. An  $f_D$  value of 0.2 was taken from literature as it does not vary significantly from system to system (Grady Jr *et al.*, 1999). Using linear regression,  $b_H$  is the slope of the curve obtained by plotting  $\ln(\text{OUR})$  vs. aeration time. Three independent repeats were carried out in duplicate using different freezer stocks. The  $b_H$  value was calculated for each dataset since the resultant value is dependent on the initial conditions (substrate and biomass concentration), which may vary between batch flasks.

### 3.1.4 Determination of the maximum specific growth rate, half-saturation coefficient, and yield coefficient of heterotrophic bacteria by the respirometric method

The principle of this method involves modelling an aerated batch reactor, comparing what is predicted to what is measured experimentally, and optimising the parameters of the model to minimise the squared error between the predictions and measurements.

#### 3.1.4.1 Batch reactor

For maximum specific growth rate ( $\mu_{\max,H}$ ), half-saturation coefficient ( $K_S$ ), and yield coefficient ( $Y_H$ ) determination, the aerated batch reactors were set up based on respirometric methods presented by Trojanowicz *et al.* (2009) and Almeida and Butler (2002). Seed inoculum (250 mL) was transferred to 4 L SW medium in a 5 L Erlenmeyer flask and incubated for 8-10 h at room temperature ( $20 \pm 2^\circ\text{C}$ ) with mixing (magnetic stirrer) and aeration (air pump). The starting conditions ensured a biomass loading rate ( $S_S/X_H$ ) that is more than 0.5 g COD/g biomass COD to allow the culture to grow at its maximum rate (Trojanowicz *et al.*, 2009). The TSS ( $X_H$ ), COD ( $S_S$ ), and OUR were measured immediately and thereafter every 30-60 min until a sharp drop in OUR was observed. Two samples were collected for OUR measurements. To one of these, *N*-allylthiourea (ATU) (Merck) was added (final concentration of 11.6 mg.L<sup>-1</sup>) before OUR measurement to inhibit autotrophic nitrification (Robertson *et al.*, 1989). OUR readings observed in the presence of ATU were not significantly lower than those without ATU. Thus, it was assumed that heterotrophs were responsible for the majority of growth for the duration of the experiment, which is reflected in the model set up (Table 3.2). This experiment was repeated three times using different freezer stocks.

#### 3.1.4.2 Batch reactor model and parameter fitting

Substrate concentration ( $S$ ), biomass growth ( $X$ ), and oxygen consumption are stoichiometrically linked according to the following balanced COD equation for aerobic chemoheterotrophic growth:

$$S - (1 - Y)O_2 = YX \quad (8)$$

where  $Y$  is the biomass yield. This allows for the use of respirometry to generate data for curve fitting. The model equations and parameters are presented in Table 3.2 and Table 3.3, respectively. Table 3.2 summarises the stoichiometry and rate expressions for heterotrophic bacteria. The process rate column gives the rate expression for the respective processes governing heterotrophic growth and decay. The entries in the component columns are the

stoichiometric coefficients which are multiplied by their respective rate expression to give the appropriate rate of consumption or production of components for each process. The value of  $f_B$  was estimated based on the inert fraction ( $S_I$ ) of  $S_T$  remaining in batch reactors operated for over one week, i.e.  $f_B = (S_T - S_I)/S_T$ . The value of  $f_{A,H}$  was assumed based on growth of the culture in the exponential phase where the majority of biomass is expected to be active.

**Table 3.2.** Stoichiometric matrix describing the batch reactor

Process	Component				Process rate
	Readily biodegradable substrate, $S_S$	Oxygen, $S_O$	Active heterotrophic biomass, $X_H$	Slowly biodegradable substrate, $X_S$	
Heterotrophic growth	$-\frac{1}{Y_H}$	$\frac{1 - Y_H}{Y_H}$	1		$\mu_{max,H} \frac{S_S}{K_S + S_S} \frac{S_O}{K_O + S_O} X_H$
Heterotrophic decay		$1 - f_D$	-1	$1 - f_{XI}$	$b_H \frac{K_b}{K_b + S_S/X_H} X_H$
Hydrolysis	1			-1	$k_h \frac{X_S/X_H}{K_X + X_S/X_H} X_H$

**Table 3.3.** Parameter values used for batch reactor model

Parameters	Description	Value	Units	Reference
$\mu_{max,H}$	Maximum specific heterotrophic growth rate	0.3178	$h^{-1}$	Fitted <sup>1</sup>
$K_S$	Half-saturation coefficient for organic substrate	1.23	$mg_{COD}.L^{-1}$	Fitted <sup>1</sup>
$Y_H$	Yield coefficient of heterotrophic biomass on substrate	0.49	$mg_{COD.}$ $mg_{COD}^{-1}$	Fitted <sup>1</sup>
$b_H$	Decay coefficient for heterotrophic biomass	0.02	$h^{-1}$	Experimental
$K_b$	Coefficient for switching function for decay	1.00	$mg_{COD}.L^{-1}$	Henze <i>et al.</i> (1995)
$K_X$	Half-saturation coefficient for hydrolysis of $X_S$	0.10	$mg_{COD.}$ $mg_{COD}^{-1}$	Henze <i>et al.</i> (1995)
$k_h$	Maximum specific hydrolysis rate	0.08	$h^{-1}$	Henze <i>et al.</i> (1995)
$\alpha$	Acclimation constant for heterotrophic biomass	0.40	-	Fitted <sup>1</sup>
$f_{XI}$	Fraction of biomass yielding particulate products	0.10	$mg_{COD.}$ $mg_{COD}^{-1}$	Henze <i>et al.</i> (1995)
$f_B$	Fraction of readily biodegradable substrate ( $S_S$ ) in total soluble substrate ( $S_T$ )	0.90	-	Specified
$f_D$	Fraction of biomass leading to debris	0.20	-	Trojanowicz <i>et al.</i> (2009)
$f_{A,H}$	Fraction of active heterotrophic biomass	0.95	-	Specified

<sup>1</sup> Mean parameter value

The kinetic parameters  $\mu_{max,H}$ ,  $K_S$  and  $Y_H$  were estimated by minimizing the squared error between the solution of the differential equations and the experimental batch profiles for OUR,

$S_S$  and  $X_H$ . The model was implemented in MATLAB with non-linear regression performed using the *lsqnonlin* (LSQ) function, which minimises the least squares problem of the form

$$\text{LSQ}(\theta) = \sum_{i=1}^n (y_i - y_{Pi}(\theta))^2 \quad (9)$$

where  $\theta$  represents the unknown parameters ( $\theta = \mu_{\max,H}, K_S, Y_H, \alpha$ ),  $y_i$  is a vector of  $i$  measurements for each response variable  $n$  (OUR,  $S_S$  and  $X_H$ ), and  $y_{Pi}$  is the corresponding model predictions that depend on the unknown biokinetic parameters. The trust-region-reflective least-squares algorithm was used with the central finite differences method, and a function and step tolerance of  $10^{-4}$ .

For the batch model eqns. 10-12 were solved simultaneously using the stiff ordinary differential equation algorithm in MATLAB, *ode15s*. The initial reactor measurements,  $S_{S,t0}$  and  $X_{H,t0}$ , were used as the starting points for eq. 10 and 11, respectively. The predicted  $S_S$  and  $X_H$  profiles were then used to solve eq. 13 to generate the predicted OUR profile.

$$\frac{dS_S}{dt} = -\frac{1}{Y_H} \mu_{\max,H} \frac{S_S}{K_S + S_S} X_H + k_H \frac{X_S/X_H}{K_X + X_S/X_H} X_H \quad (10)$$

$$\frac{dX_H}{dt} = \mu_{\max,H} \frac{S_S}{K_S + S_S} X_H - b_H \frac{K_b}{K_b + S_S/X_H} X_H \quad (11)$$

$$\frac{dX_S}{dt} = (1 - f_{XI}) b_H \frac{K_b}{K_b + S_S/X_H} X_H - k_H \frac{X_S/X_H}{K_X + X_S/X_H} X_H \quad (12)$$

$$\text{OUR} = \left( \frac{1 - Y_H}{Y_H} \right) \mu_{\max,H} \frac{S_S}{K_S + S_S} X_H + (1 - f_D) b_H X_H \quad (13)$$

Slowly biodegradable substrate concentration ( $X_S$ ) was included in the model which reduced the residual error. The  $X_S$  value was assumed to be 1% of the initial  $S_S$  for each dataset.

It was noted that there was an initial acclimation/lag period based on the variable profiles. Fitting to data with an acclimation period would return inaccurate parameter estimates since the Monod equation is unable to model growth during the lag or acclimation phase. Therefore, an empirical equation from Checchi and Marsili-Libelli (2005) was adapted to mimic the effect of an increasing number of cells growing at their maximal rate as time progresses:

$$\mu_{\max,H} \frac{S_S}{K_S + S_S} [X_{H,t} - X_{H,t_0} \cdot e^{-\alpha t}] \quad (14)$$

where  $\alpha$  is the acclimation rate constant. Eq. 14 was used in place of the standard Monod equation for the batch model. This expression resulted in a better fit.

The LSQ function required initial guesses as an input for each parameter value to be optimised. Varying the initial guesses (an input for LSQ) may lead to different optimised parameter values as different local minima are found. In order to find the global minimum, a for-loop was programmed to run LSQ iteratively using all possible combinations (27 in total) of parameter starting points listed in Table 3.4. These values were informed by literature sources of similar systems. The parameters were also restricted by boundary values to exclude biologically impossible values. This method was repeated for each dataset. Using goodness-of-fit statistics, the parameters resulting in the best fit for the three response variables ( $X_H$ ,  $S_S$ , OUR) were chosen.

**Table 3.4.** Initial guess combinations and boundary conditions used as inputs for the LSQ function

Parameters	$\mu_{max,H}$	$K_S$	$Y_H$	$\alpha$
Initial Guesses	0.25	1.00	0.45	0.20
	0.30	3.00	0.50	0.50
	0.35	5.00	0.55	0.80
Bounds	Lower	0.00	0.50	0.40
	Upper	1.00	10.0	0.70
				1.00

### 3.1.3 Parameter sensitivity analysis

A parameter sensitivity analysis was conducted to evaluate the sensitivity of the response variables to changes in parameter values optimised by LSQ. One of the estimated model parameters were varied while holding the remaining parameters constant. Sensitivity of the variables was evaluated based on the effect on the resulting response variable profiles. Two standard deviations on either side of the best fit parameter mean were used to illustrate the sensitivity of the response variables using the starting conditions of run 1.

### 3.1.4 Statistical analysis

To assess the predictive accuracy of the batch model the root mean squared error (RMSE) and normalised RMSE (NRMSE) were calculated for the fit to each response variable:

$$\text{RMSE} = \sqrt{\frac{1}{n} \sum_{i=1}^n (y_i - y_{Pi})^2} \quad (15)$$

RMSE is a measure of precision of the model fit to experimental data that aggregates residuals into a single measure of predictive power. NRMSE was calculated by normalising RMSE by the mean of the response variable measurements. For regression analysis, 95% confidence intervals (CIs) were calculated for estimated parameter values, and 95% prediction intervals (PIs) were calculated for response variables. For clarity, a CI is a measure of the precision of the estimated best fit value of a particular parameter. A PI is an estimate of the range that is likely to contain the response value of future observations, given what has already been observed. The 95% CI and 95% PI was calculated using the built in MATLAB functions *nlpaci* and *nlpredci*, respectively.

### 3.2 Results

#### 3.2.1 Decay coefficient

OUR measurements from day 2 onwards were used for  $b_H$  determination based on the  $S_S$  and  $OD_{600\text{ nm}}$  profiles (Figure 3.1). After approximately 2 d,  $S_S$  was completely consumed, leaving only  $S_I$  and slowly biodegradable substrate. The  $OD_{600\text{ nm}}$  has also begun to decline indicating the culture has entered the death phase of microbial growth. The above confirms that the culture was in the decline phase. Here, all oxygen uptake was due to heterotrophic biomass decay. Data for all three independent repeats with duplicates are shown in Table A1. The mean value of  $b_H$  was calculated to be  $0.0206 \pm 0.0019 \text{ h}^{-1}$  with a coefficient of variation (CV) of 9.3%, indicating good repeatability.

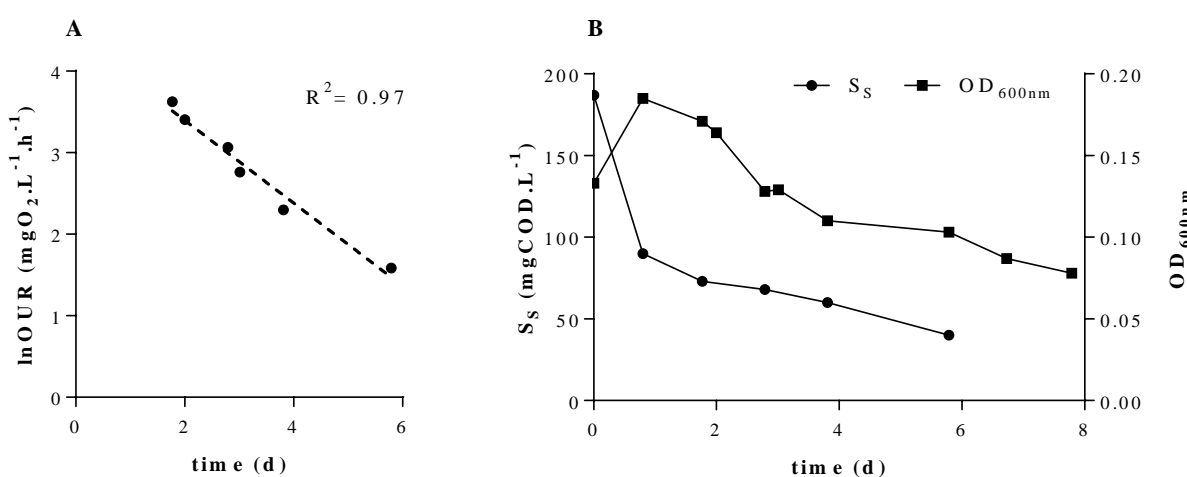


**Figure 3.1.** Example plot of **A.** decay coefficient determination and **B.** corresponding soluble substrate and optical density data of environmental sample cultured in a batch reactor. Shown is data from run 3A.

### 3.2.2 Maximum specific growth rate, half-saturation coefficient, and yield coefficient

A respirogram indicating the difference in OUR measurements in the presence and absence of ATU is depicted in Figure 3.2. An example calculation of OUR is indicated in Figure A1. There was no decrease observed in the OUR profile for all three repeats when ATU was added to the respirometer. This indicated that autotrophic nitrification was negligible in the batch reactors for the duration of the experiment. Therefore, heterotrophic growth was assumed to be dominant in the reactor and the batch model for parameter fitting was set up accordingly (Table 3.2). A minor increase in OUR measurements was noted in the presence of ATU, which was unexpected, and explained later. The NATU dataset for OUR was used for parameter fitting.

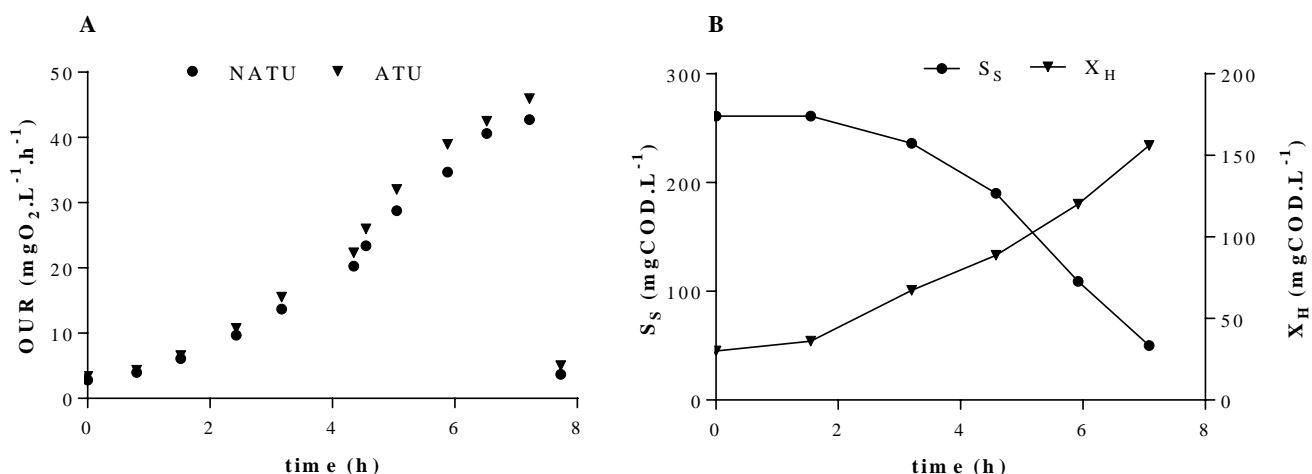


**Figure 3.2.** Example plot of **A.** respirogram and **B.** corresponding heterotrophic biomass and substrate concentration profiles of environmental sample cultured in batch. Shown is data from run 3. NATU: Non-ATU.

Regression of the batch model to experimental response variables resulted in a good fit for runs 2 and 3, with  $R^2$  values above 0.96 (Figure 3.3). The 95% PIs were tight and NRMSEs below 11%, indicating good precision. The fit to run 1 was not as confident with relatively wider 95% PIs and a NRMSE of 43% for the OUR profile. Fitting statistics are shown in Table A3 and residual error plots are shown in Figure A2.

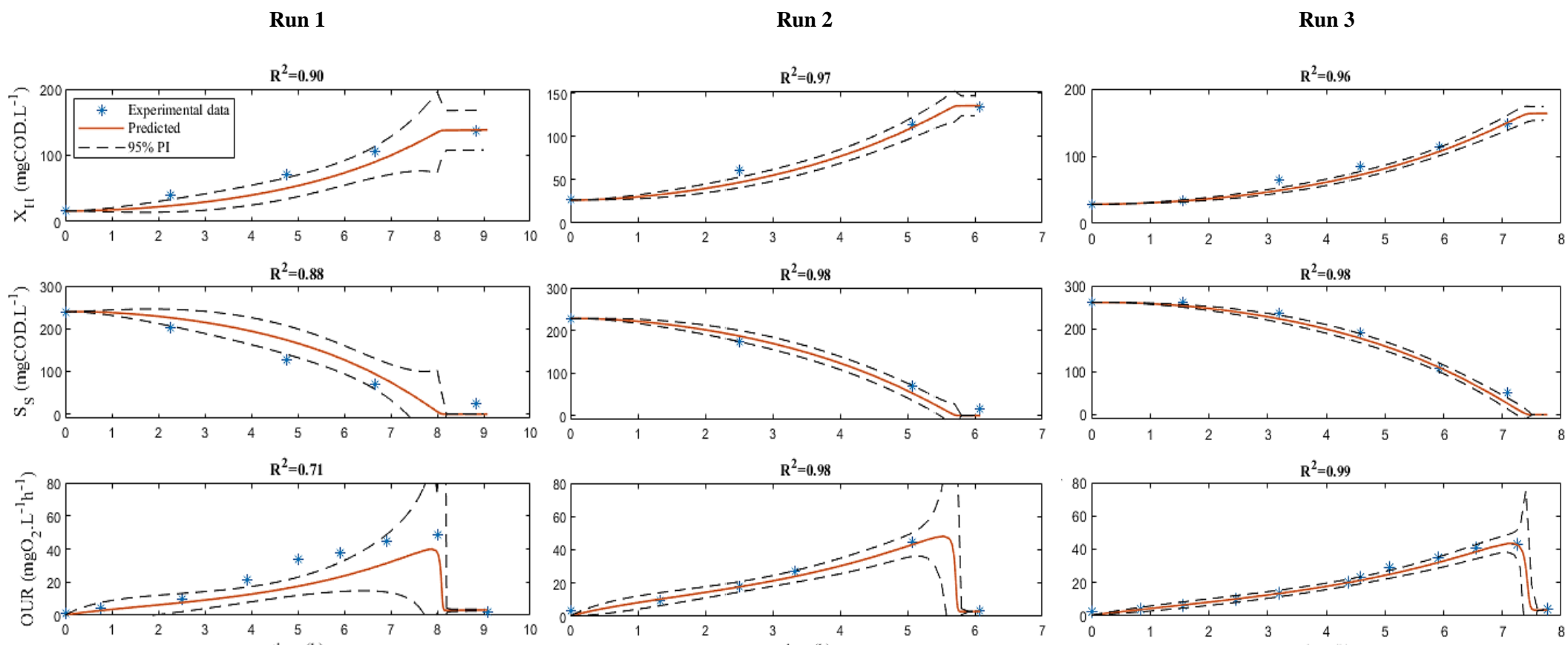


**Figure 3.3.** Non-linear regression of best fit parameter set to response variable profiles of three experimental repeats. Runs were conducted under the same conditions but varying initial concentrations of  $S_S$  and  $X_H$ . 95% prediction intervals are indicated.

The initial conditions ( $S_S/X_H$ ) for each batch reactor were measured and found to vary (Table A2). Since the response variable profiles are dependent on the initial conditions of each batch reactor, the measurements for the experimental repeats were not averaged. Nonetheless, this does make parameter estimations more robust since estimations are made at different conditions. Therefore, non-linear regression was performed on each experimental dataset and the mean of the estimated parameters calculated (Table 3.5). The individual estimates for each run are reported in Table A4. The estimates for  $\mu_{max,H}$  and  $Y_H$  were reproducible for the three runs, both with a CV below 6%. The individual estimates were also confident, with narrow 95% CIs.

At the point where OUR suddenly drops, the 95% PI widens in all three runs (Figure 3.3). It is around this point where the value of  $K_S$  plays a significant role, controlling the slope of the sharp decline in OUR and  $S_S$ , and the plateau in  $X_H$  when  $S_S$  becomes limiting. This indicated a high uncertainty in the estimation of  $K_S$ , and is reflected by the wide 95% CI on the individual  $K_S$  estimates (Table A4). The CV for the estimation of  $K_S$  was relatively higher as well (29%).

**Table 3.5.** Biokinetic parameter values estimated for three experimental repeats.

	$\mu_{max,H}$ ( $h^{-1}$ )	$K_S$ ( $mg_{COD} \cdot L^{-1}$ )	$Y_H$ ( $mg_{COD} \cdot mg_{COD}^{-1}$ )
Mean	0.3178	1.2344	0.4928
SD	0.0166	0.3632	0.0151
CV (%)	5.2	29	3.1

SD: Standard deviation. CV: Coefficient of variation.

A parameter estimation response surface was created to evaluate parameter retrievability for  $\mu_{max,H}$  and  $K_S$ , since these had the highest CVs of the estimated parameters (Figure 3.4). This also allowed an investigation into the uncertainty of  $K_S$ . The surface was created by calculating the sum of squared errors (SSE) computed from a grid of  $\mu_{max,H}$ ,  $K_S$  pairs in the neighbourhood of the optimum.

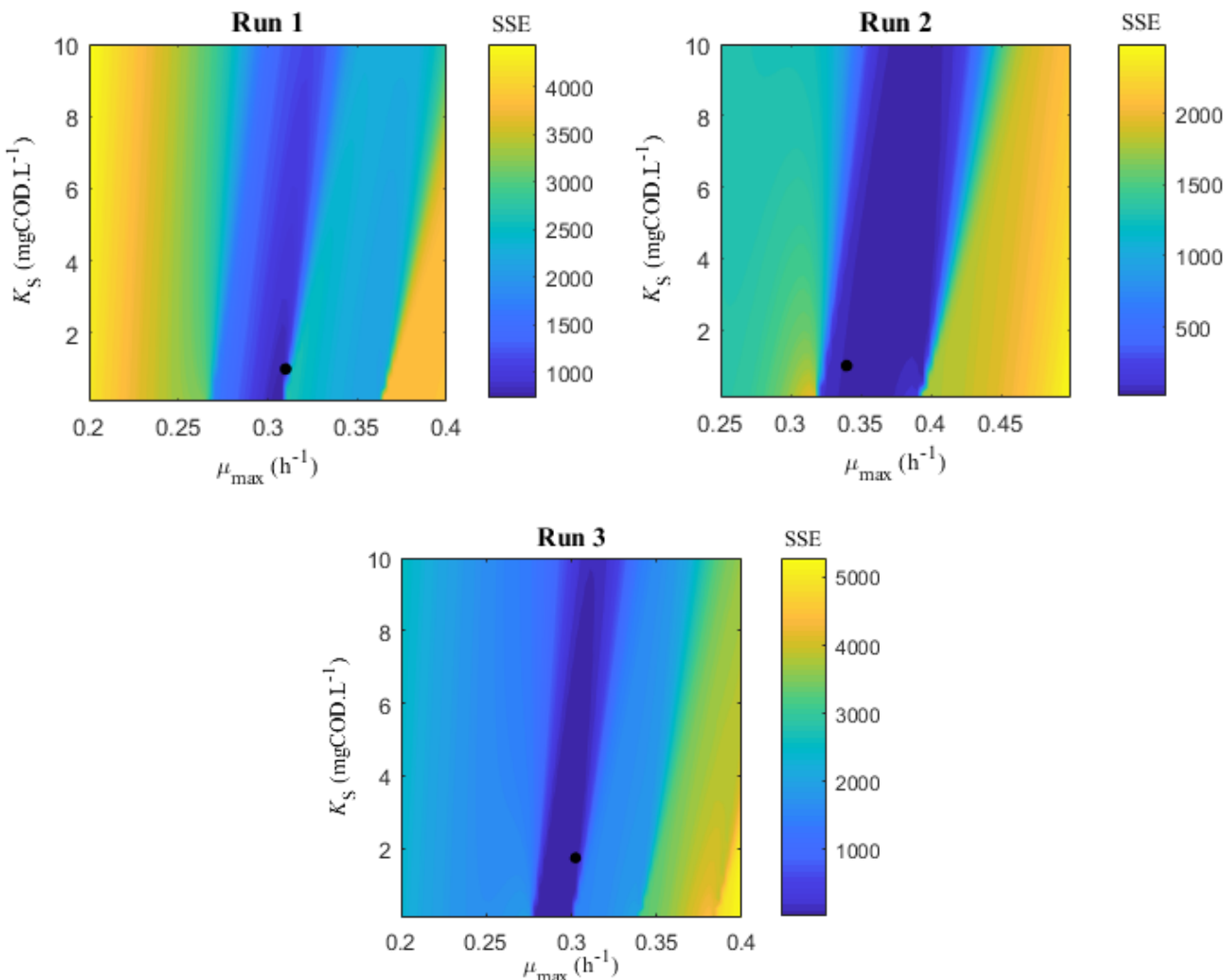


**Figure 3.4.** Parameter estimation response surface with sum of squared error (SSE) for OUR profiles. Shown is the error resulting from regression of the batch model to three OUR datasets over a range of  $\mu_{\text{max},H}$  and  $K_s$  values. The best fit parameter values are indicated by the black dot.

For all runs, the surface had a single, unidirectional valley with a slightly sloped valley floor as it approached a  $K_s$  of 1 mg.L<sup>-1</sup>. The response surface for  $\mu_{\text{max},H}$  and  $K_s$  is characteristic for Monod-like batch models (Vanrolleghem *et al.*, 1995). The  $\mu_{\text{max},H}$  value was tightly constrained by steep walls over the range of  $K_s$  values. In contrast, the error remains low over a range of  $K_s$  values which explains the wide 95% PI at the sudden drop in OUR in Figure 3.3. Most optimisation runs converged at the global minimum observed for each dataset. Although undesirable local minima were also found at different initial guesses, these were rejected due to returning much higher residual errors. Thus, the estimated parameters were deemed as suitably retrievable using the proposed model.

Comparisons of estimated biokinetic parameters with literature values are summarised in Table 3.6. Besides  $\mu_{\text{max},H}$  and  $Y_H$ , estimates for the parameters  $K_s$  and  $b_H$  were within the

expected range of values. The estimated value for  $\mu_{\max,H}$  was slightly higher than is common in literature for similar systems, but is expected for growth on rapidly hydrolysable substrate and at higher temperatures. Furthermore, the estimated value for  $Y_H$  is lower than usual for heterotrophic bacteria.

**Table 3.6.** Literature kinetic parameters values at neutral pH and 20°C.

<b>Reference</b>	<b>Kinetic parameter</b>			
	$\mu_{\max,H}$ (d <sup>-1</sup> )	$K_S$ (mg <sub>COD</sub> .L <sup>-1</sup> )	$Y_H$ (mg <sub>COD</sub> .mg <sub>COD</sub> <sup>-1</sup> )	$b_H$ (d <sup>-1</sup> )
Almeida and Butler (2002) <sup>1</sup>	6.3	-	0.57	-
Henze <i>et al.</i> (1987) <sup>2</sup>	3.0-6.0 <sup>3</sup>	20.0	0.67	0.2-0.62
Henze <i>et al.</i> (1995) <sup>2</sup>	3.0-6.0 <sup>3</sup>	-	0.63	0.2-0.4
Kappeler and Gujer (1992) <sup>2</sup>	1.0-8.0	2.5-4.0	-	-
Riefler <i>et al.</i> (1998) <sup>4</sup>	5.28	0.99	-	-
Trojanowicz <i>et al.</i> (2009) <sup>1,5</sup>	6.1	9.4	0.58	0.18
Present study	7.63	1.23	0.49	0.49

Parameters were reported as d<sup>-1</sup> here for convenient comparison to literature values.

<sup>1</sup> Measured for suspended biomass

<sup>2</sup> Activate sludge

<sup>3</sup> Values for 10-20°C

<sup>4</sup> Curve fitting for OUR measurements on biofilm reactor

<sup>5</sup> Resuspended biofilm

### 3.2.3 Parameter sensitivity analysis

The sensitivity of response variables (X<sub>H</sub>, S<sub>S</sub>, OUR) to variations in the estimated parameters is shown in Figure 3.5. The response variables for the batch model are sensitive to changes in Y<sub>H</sub> and  $\mu_{\max,H}$ . Despite the uncertainty of the estimated K<sub>S</sub> value, the X<sub>H</sub> and S<sub>S</sub> profiles were not sensitive to variations around the mean, but the peak and slope of the sharp decline in the OUR profile was mildly sensitive. Note the effect of a decreasing acclimation rate which resulted in a longer acclimation period.

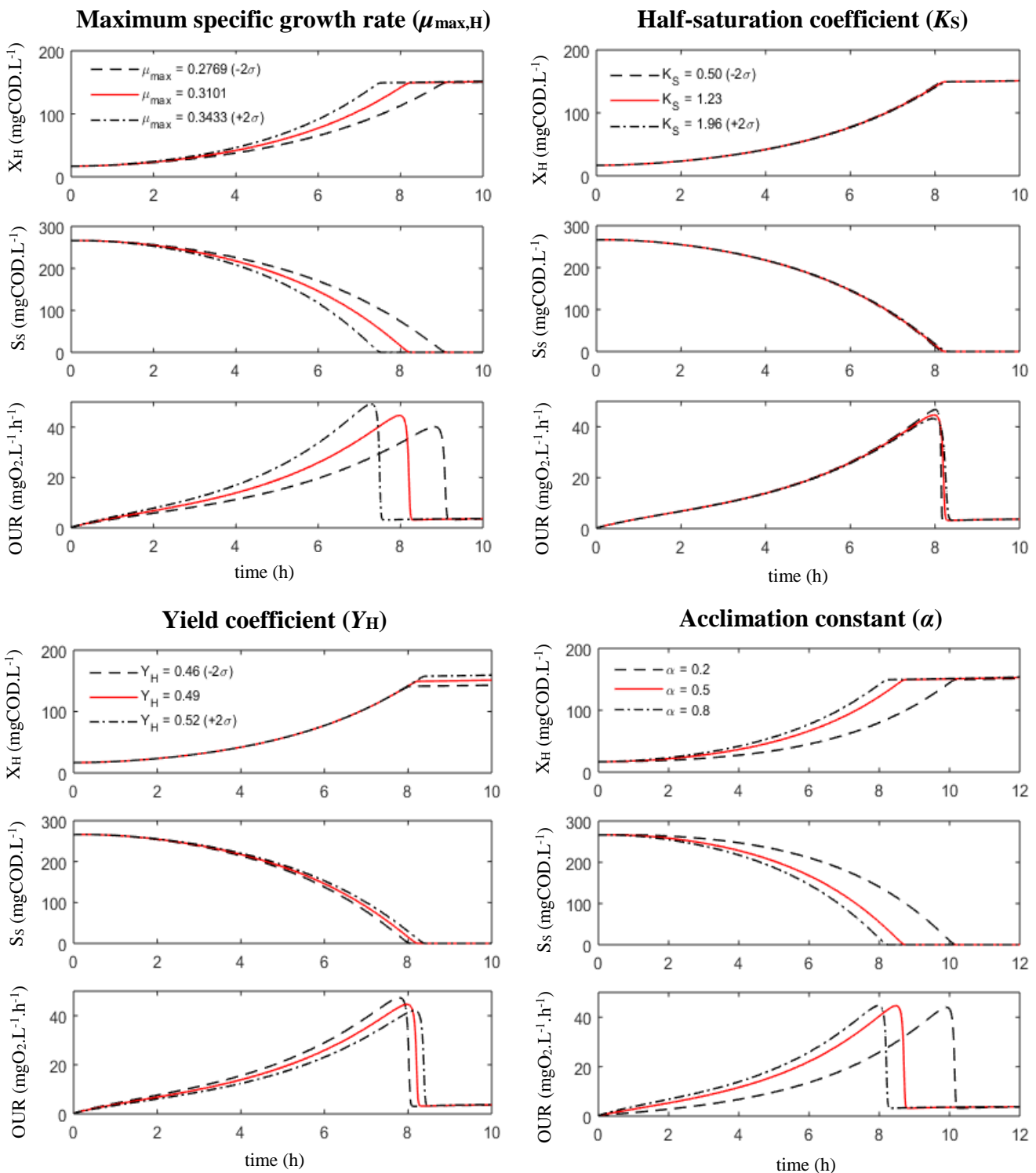


**Figure 3.5.** Sensitivity of response variable profiles to variations in estimated parameters using initial conditions from run 3. Parameters values, except the acclimation rate, were varied by two standard deviations around the mean of estimated parameters.

## CHAPTER 4: FLOW CELL BIOREACTOR AND BIOFILM SIMULATIONS

### 4.1 Materials and Methods

#### 4.1.1 Design and operation of bioreactor

A continuous tubular reactor with in-line flow cells was designed and built with the intention to cultivate and monitor biofilm development (Figure 4.1). Biofilms were cultivated in Perspex flow cells (Wolfaardt *et al.*, 1994). Each flow cell had four recessed flow chambers (31 x 4.0 x 2.2 mm) with holes for inlet and outlet tubing. Flow cells were covered with glass coverslips (50 x 24 mm, 0.13-0.17 mm thickness) and sealed with silicone adhesive to allow for visualisation of the biofilm using CLSM. Silicone tubing (Kimix) with an internal diameter of 1.6 mm was used for the influent and effluent lines. Tubing was connected using straight or T-piece plastic connectors (Cole Palmer, IL, USA). Two parallel reactors were set up: a control and treatment line as illustrated in Figure 4.1. Influent flasks were sealed with rubber stoppers fitted with 1 mL glass pipettes to allow for media uptake and venting with sterile air (0.2 µm, Millex-FG, hydrophobic PTFE, 50 mm).

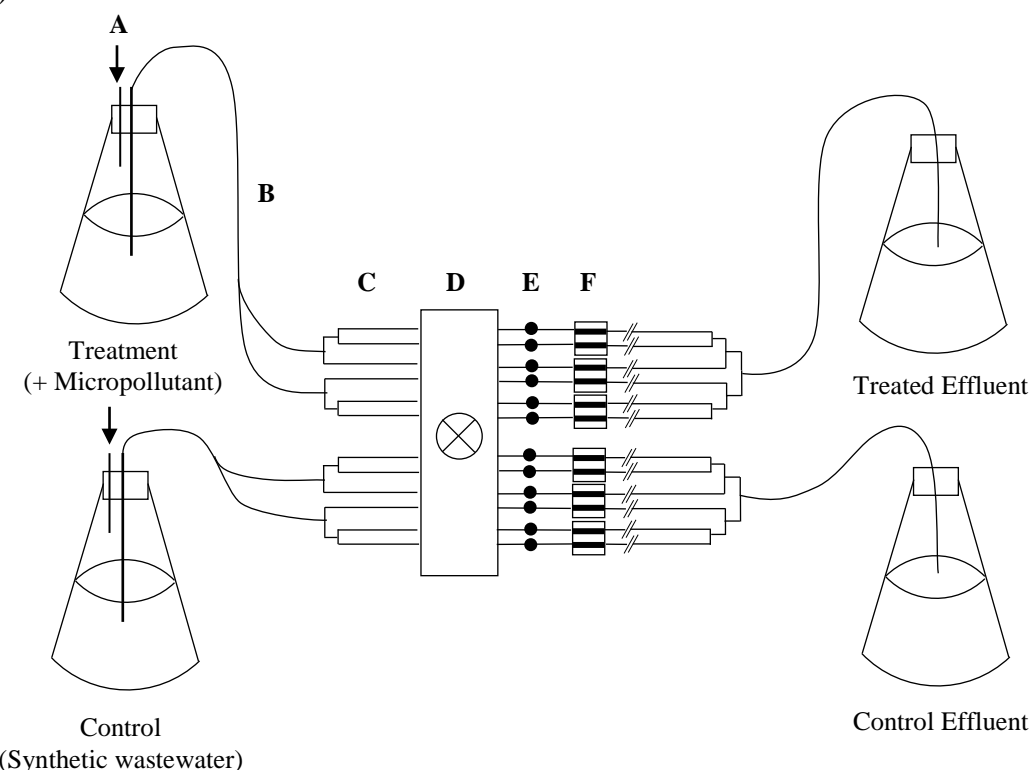


**Figure 4.1.** Diagram of continuous flow cell bioreactor. **A.** Sterile air. **B.** Two parallel reactors for each condition was set up, except for the validation run where both reactors were operated under control conditions. **C.** Silicone tubing split with T-pieces. **D.** 12 channel peristaltic pump. **E.** Bubble traps. **F.** Flow cells.

Glass bubble traps were connected upstream of the flow cells to prevent bubbles passing through which would damage the biofilms. A 12-channel peristaltic pump (Watson Marlow 205S) was used to maintain a flow rate of  $10 \text{ mL.h}^{-1}$  (1.6 rpm), leading to the displacement of the internal volume of each flow cell chamber every 40 seconds. This resulted in a dilution rate of  $18 \text{ h}^{-1}$  within the flow chambers. All flow cell experiments were conducted at room temperature ( $20 \pm 2^\circ\text{C}$ ).

#### **4.1.2 Sterilisation of bioreactor**

The reactor was sterilised by running a 20% (v/v) NaOCl (bleach) solution through the entire system at  $10 \text{ mL.h}^{-1}$  for 1-3 h. The flow cell was rinsed overnight with sterile reverse osmosis water. Flasks containing 5 L sterile SW medium were connected to the inlet tubing aseptically and the water flushed out the system for 1 h. The flow was stopped and the tubing upstream of the flow cell was clamped before inoculation.

#### **4.1.3 Inoculation of flow cells**

The inoculum was prepared using the same procedure described for the respirometry experiments (Section 3.1.1). The optical density of the inoculum was adjusted immediately before inoculation to an  $\text{OD}_{600 \text{ nm}}$  of 0.1 using sterile 0.9% saline. The inoculum was injected slowly into the flow chamber through the tubing immediately upstream of the flow cell using a sterile 1 mL syringe and 26-gauge needle. The injection hole left by the needle was sealed with silicone glue. All flow chambers were inoculated with the same pre-culture. The flow cell was then inverted (cover slip facing down) for 1 h under stagnant conditions to allow the inoculum to adhere to the cover slip. Following this, the flow cell was inverted again, the clamps removed, and the flow resumed.

#### **4.1.4 Reactor optimisation**

Initially, overgrowth was noted within the flow cells including biofilm growth upstream of the flow cell which could potentially cause blockages. To prevent this, the COD of the medium was reduced to approximately  $120 \text{ mg.L}^{-1}$ , the flow rate reduced from  $12.5 \text{ mL.h}^{-1}$  to  $10 \text{ mL.h}^{-1}$ , and the flow cells covered to prevent phototrophic growth. The pH was also reduced to 7.5 to bring it in line with that detected in raw wastewater. These changes resulted in manageable growth of the biofilm within the flow cells.

It was found that some of the microcolonies within the biofilm lost their structural integrity before microscopic analysis. It was hypothesised that, during flow cell preparation for microscopy, the microcolonies would disperse due to the lack of influent substrate or a

change in flow conditions. This phenomenon is noted in literature for certain bacterial species (Hunt *et al.*, 2004). Further work is needed to confirm this. To avoid this issue, paraformaldehyde (PFA), which acts to cross-link proteins within the biofilm, was used to fix the biofilm and strengthen structural integrity.

#### **4.1.5 Experimental runs**

##### **4.1.5.1 Batch diclofenac screen**

Batch cultures were grown in the presence of DCF to screen for effects in microbial growth. Three parallel batch reactors (250 mL SW medium) were set up containing 0, 0.005, and 5 mg.L<sup>-1</sup> DCF, respectively. Each was inoculated with 1 mL of pre-culture and incubated at 26°C with shaking (150 rpm) for 32 h. The OD<sub>600 nm</sub> and colony forming units/mL (CFU/mL) was measured periodically. For CFU/mL measurements, agar plates were made using 10X concentrated SW medium with agar powder added. Serial dilutions of batch cultures were plated out in 10 µL spots in duplicate (100 µL total) and the CFU/mL calculated:

$$\text{CFU/mL} = \frac{\text{number of colonies}}{\text{volume plated} \times \text{dilution factor}} \quad (16)$$

##### **4.1.5.2 Validation**

The objective of this experiment was to monitor the initial development of biofilm structure in order to validate the iDy whole MiCS model output. The reactor was set up as in Figure 4.1 but without DCF exposure and operated for 4 d. Biofilm structure was monitored at 26.5, 45.5, 70.5 and 94.5 h (T<sub>1</sub>, T<sub>2</sub>, T<sub>3</sub>, and T<sub>4</sub>). At each time point, a flow cell was sacrificed for microscopy. Due to limited lines on the peristaltic pump, T<sub>1</sub> and T<sub>4</sub> were operated with duplicate flow chambers while T<sub>2</sub> and T<sub>3</sub> were operated with 4 flow chambers.

##### **4.1.5.3 Diclofenac exposure**

The objective of this experiment was to monitor the impact of DCF exposure over time on 3-day old biofilms compared to a control. Exposure at a low concentration of 0.1 mg.L<sup>-1</sup> and a high concentration of 10 mg.L<sup>-1</sup> DCF was tested. The purpose was to produce two different scenarios for the iDy whole MiCS model to replicate and to test for dose-dependency of DCF exposure. An environmentally relevant concentration of 0.1 mg.L<sup>-1</sup> was chosen as this was approximately the midpoint of the range that DCF has been detected in wastewater influent in South Africa (Archer *et al.*, 2017b). A higher concentration of 10 mg.L<sup>-1</sup> was chosen as it was in the range that an inhibitory effect is reported in literature (Mazumdar

*et al.*, 2009). This concentration was on the lower end of the planktonic MIC range reported in literature, therefore, a sub-inhibitory effect was expected against biofilms.

The reactor was set up as in Figure 4.1 and inoculated according to the protocol outlined above (Section 4.1.3) for two independent runs – at the low and high DCF concentration. Biofilms were allowed to develop for 72 h under control conditions in all flow chambers. A concentrated DCF stock ( $5 \text{ g.L}^{-1}$ ) was made up in HPLC-grade methanol and stored at  $4^\circ\text{C}$ . Aliquots of the DCF stock were allowed to evaporate completely and then resuspended in sterile 0.9% saline. An appropriate amount was added aseptically to 5 L sterile SW medium to make up the relevant concentration in the influent. After 72 h of biofilm growth one of the influent flasks was then replaced with one containing DCF at the relevant concentration. 125  $\mu\text{g}$  of DCF was evaporated for the  $0.1 \text{ mg.L}^{-1}$  run to account for any loss that may occur during resuspension and addition to the media. To avoid dilution of DCF in the bubble traps the tubing immediately upstream of the flow cell was clamped, disconnected aseptically, and the bubble traps drained. The bubble traps were then filled again with DCF-containing medium, reconnected to the flow cells, and the flow resumed. The influent flask and tubing upstream of the flow cells were covered with aluminium foil to prevent photodegradation of DCF.

Biofilm structure was analysed on the control line immediately after connecting the DCF flask ( $T_0$ ). Biofilm structure was subsequently monitored at 12, 24, and 36 h ( $T_1$ ,  $T_2$ , and  $T_3$ ) for both control and treatment lines.  $T_3$  did not include duplicate flow chambers due to limited channels on the peristaltic pump. Data was not available for  $T_3$  (36 h) for the  $0.1 \text{ mg.L}^{-1}$  run due to bubble damage.

#### 4.1.6 Liquid chromatography – mass spectrometry

For the  $0.1 \text{ mg.L}^{-1}$  run, the concentration of DCF in the effluent of the  $T_2$  line was monitored using liquid chromatography-mass spectrometry (LCMS) to determine if biodegradation occurred. The temporal stability of DCF in the influent was also monitored for the duration of the experiment to determine if abiotic degradation occurred. The nominal DCF concentration ( $C_0$ ) was measured immediately after addition to the influent flask. The influent was sampled periodically and subjected to LCMS analysis. Samples were collected every 4 h in 10 mL aliquots and kept on ice throughout. The samples were concentrated by solid phase extraction (SPE) using a hydrophilic-lipophilic balance (HLB) 3cc (60 mg) extraction cartridge (Oasis<sup>®</sup>).

Prior to SPE, the HLB cartridge was connected to a vacuum manifold and conditioned with 3 mL HPLC-grade methanol and 3 mL Millipore water, respectively, under gravity. Care was taken to prevent drying of the column after conditioning. The sample (10 mL) was filtered through a 0.22 µm cellulose-acetate syringe filter (to remove cellular material) and the filtrate drawn through the SPE column under -5 mmHg vacuum. Once the sample had passed through the column completely, it was allowed to dry under vacuum for 30 min. The columns were then sealed with parafilm, wrapped in foil, and stored in an airtight package at -20°C until submission for LCMS analysis.

Prior to LCMS analysis, the SPE columns were thawed and the sample eluted under gravity using 4 mL HPLC-grade (99.9% purity) methanol into pyrolysed, borosilicate glass test tubes. The methanol in the eluate was allowed to evaporate completely by sparging with N<sub>2</sub> gas. The dried sample was then resuspended in 1 mL HPLC-grade methanol (10X concentrated) and centrifuged at 14 000 rpm for 10 min to remove residual debris. The supernatant (450 µL) was pipetted into a pyrolysed borosilicate glass vial insert (Stargate Scientific) placed within a 2 mL glass vial and sealed tightly. Samples were stored at 4°C and analysed the following day using an Acquity UPLC® Mass Spectrometer at the Central Analytic Facility (CAF), Stellenbosch University. A set of standard concentrations, from 1 to 400 ppb (µg.L<sup>-1</sup>), was used to set up the standard curve.

#### **4.1.7 Confocal microscopy of biofilms**

##### **4.1.7.1 Preparation of flow cells for microscopy**

When biofilm structure needed to be analysed a flow cell was sacrificed and prepared for CLSM. The effluent tubes of the flow chambers were clamped and the relevant lines were disconnected from the peristaltic pump. The inlet tubes were cut so that at least 5 cm of inlet tube was left connected to the flow cell. A second peristaltic pump was placed on the effluent side of the flow cell, and after connecting the effluent tubes to the pump, the clamps were gently removed. Using a slow reverse flow, a drop of medium was allowed to form on the end of the inlet tubes (to prevent intake of air during the next step). The inlet tubes were then submerged in 4% (w/v) PFA fixative in a 50 mL beaker (Appendix B). The PFA was drawn into the flow channels at 10 mL.h<sup>-1</sup> for 15 min. The flow was then stopped for 45 min to allow the fixative to work. The PFA was then flushed with 1X phosphate-buffered saline (PBS) for 15 min at the same flow rate (Tolker-Nielsen and Sternberg, 2011). The influent tubes were clamped and 200 µL of a 2 µL.mL<sup>-1</sup> working stock of Syto9™ (Invitrogen, Molecular Probes, USA) was injected slowly into the flow

chambers using a sterile 1 mL syringe and 26-gauge needle. The dye was allowed to bind to the biofilm in the dark for 30 min. The clamps were then removed, the line reconnected to the secondary pump, and flow resumed for 15 min to flush residual dye with sterile PBS. The influent tubes were then clamped again and the flow cell disconnected from the flow system, sealed with stoppers, and wrapped in foil. Syto9<sup>TM</sup> is a non-specific nucleic acid stain, with an excitation maxima of 480–500 nm.

#### 4.1.7.2 Image acquisition

The biofilms were observed using a Carl Zeiss LSM 780 confocal microscope at the Central Analytic Facility (CAF), Stellenbosch University. Images were obtained with a LD Plan-Neofluar 40 $\times$ /0.6 Korr M27 objective and excitation from a 488 nm Argon laser. Imaging conditions similar to Heydorn *et al.* (2000a) were used to minimise variations between experimental rounds and between flow channels. For all experiments, images were acquired at random positions within 5–10 mm from the inlet and in the middle two-thirds of the flow chamber. Seven image Z-stacks were obtained for each flow channel. Images were recorded with a scan area of 212.55  $\mu\text{m}^2$  (XY). Biofilm image stacks were acquired with an interval of 1.68  $\mu\text{m}$  in the Z-direction, resulting in a voxel volume of 0.2964  $\mu\text{m}^3$ . The number of images in each Z-stack varied depending on the thickness of the biofilm. Additional capture conditions are listed below:

- Image size (pixels): 512 $\times$ 512
- Pixel size (XY): 0.42  $\mu\text{m}$
- Pixel dwell: 2.55  $\mu\text{s}$
- Detection wavelength: 502–672 nm
- Pixel averaging: 2

Orthogonal views of the biofilm were generated using the ZEN 2.3 software (Carl Zeiss Microscopy).

#### 4.1.8 Biofilm model

##### 4.1.8.2 Model description

Biofilm structure was simulated using the iDyNoMiCS package which was adapted to represent the experimental system (Lardon *et al.*, 2011). The model was made up of three classes of discrete particles – heterotrophs, autotrophs, and EPS – whose growth is linked to local substrate concentration and class-specific growth kinetics. For simplicity, heterotrophs and autotrophs are simulated with lumped parameters and generic particle properties sourced from literature. Heterotrophs act aerobically to oxidise organic donor substrate (as COD), to produce biomass and EPS, whereas autotrophs act as nitrifiers, oxidising ammonia directly to nitrate. For both species growth is governed by Monod kinetics for substrate utilisation while loss is governed by endogenous respiration and decay processes. All biomass could additionally be lost through physical detachment from the biofilm surface. Model parameters and the stoichiometry of all reactions are summarised in Table 4.1 and Table 4.2, respectively. Biofilm development proceeds iteratively, where, at each iteration, particles grow in size, consume substrate, divide at a critical cell size, and undergo shoving when in contact with neighbouring particles.

While biomass is modelled discretely (Figure 4.2), solute concentrations (COD, O<sub>2</sub>, NH<sub>4</sub>, NO<sub>3</sub>) are determined by partial differential reaction-diffusion equations solved numerically to steady-state at each iteration using a multigrid algorithm (Lardon *et al.*, 2011). Cyclic boundaries were implemented at the vertical borders and a zero-flux boundary at the bottom border of the computational domain. A mass transfer boundary layer was implemented as a moving upper boundary 48 µm above the biofilm surface.

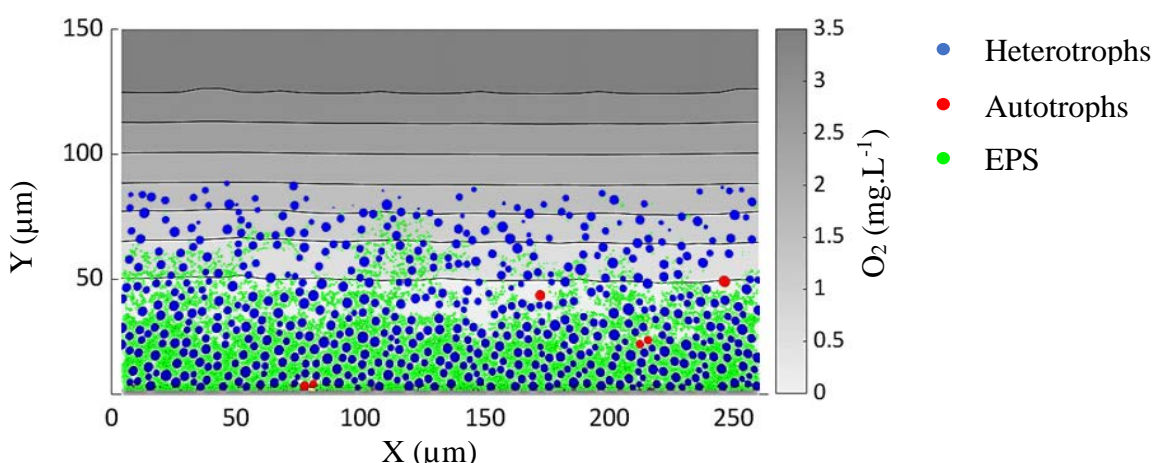


**Figure 4.2.** 2-Dimensional representation of computation domain of biofilm IbM. Particulate components (heterotrophs, autotrophs, EPS) are represented by agents while dissolved components (oxygen) are represented by a continuum.

#### 4.1.8.2 Simulations

Simulations were initialised using the input parameters in Table 4.3. The system was inoculated at  $t_0$  with 8 particles of heterotrophs and 4 particles of autotrophs, placed at random locations on the substratum surface. A ratio of 2:1 heterotrophs to autotrophs was chosen to represent the inoculum in which heterotrophs were identified to dominate. The estimated heterotrophic kinetic parameters were used to calibrate the biofilm model. Remaining parameters were sourced from literature. Biofilm structure was recorded every 0.5 h of simulated biofilm growth. Simulation iterations were governed by an adaptive timestep with a  $t_{\min}$  of 0.05 h and a  $t_{\max}$  of 0.25 h. Simulations were performed using the Stellenbosch University High Performance Computing (HPC) cluster. Biofilm simulation images were rendered using POV-Ray™ 3.7.0 (Persistence of Vision Pty. Ltd., Victoria, Australia). A sample protocol file for initiating an iDyNoMiCS simulation is shown in Appendix E.

The biofilm model, implemented in the iDyNoMiCS platform, was validated against emergent structural parameters of an experimentally observed biofilm grown under control conditions. Validation simulations were run for 96 h under control conditions. Biofilm structural parameters were calculated for the model output and compared to the experimental dataset.

For treatment runs, simulations were run for 72 h under control conditions, after which DCF was introduced into the bulk compartment at the relevant concentration and the simulation continued for a further 24 h (4 d total). Based on the experimental data, it was hypothesised that the dose-dependent effect of DCF on the biofilm can be described by a simple inhibition kinetic model and a Haldane kinetic model, shown in eq. 17 and 18, respectively.

$$\mu = \frac{K_{I,DCF}}{K_{I,DCF} + S_{DCF}} \quad (17)$$

$$\mu = \mu_{DCF,H} \frac{S_{DCF}}{K_{S,DCF} + S_{DCF} + \frac{S_{DCF}^2}{K_{I,DCF}}} \quad (18)$$

This kinetic was incorporated into aerobic heterotrophic growth as indicated in Table 4.2. The Haldane model (eq. 18) was incorporated to replicate the effect of an increase in growth with a decrease in DCF concentration. The value of  $K_{I,DCF}$  was crudely estimated to be  $5 \text{ mg.L}^{-1}$  based on the low end of planktonic MICs in literature (Dastidar *et al.*, 2000, Mazumdar *et al.*, 2009). The value of  $K_{S,DCF}$  was set to result in an increase in growth when exposed to  $0.1 \text{ mg.L}^{-1}$ . The value of  $\mu_{DCF,H}$  was set such that the peak of the DCF *vs.*  $\mu$  response curve equals that value of  $\mu_{\max,H}$ .

**Table 4.1.** Parameters used for biofilm model simulations

Parameters	Description	Value	Units	Reference
Reaction rate				
Heterotrophs (H)				
$\mu_{\max,H}$	Max. specific growth rate	0.3178	$\text{h}^{-1}$	Experimental
$\mu_{\text{DCF},H}$	Max. growth rate on DCF	0.3270	$\text{h}^{-1}$	Specified
$K_{S,H}$	Saturation constant for COD	1.23	$\text{mg}_{\text{COD}} \cdot \text{L}^{-1}$	Experimental
$K_{O,H}$	Saturation constant for $\text{O}_2$	0.2	$\text{mg}_{\text{O}_2} \cdot \text{L}^{-1}$	Wanner <i>et al.</i> (2006)
$K_{S,\text{DCF}}$	Saturation constant for DCF	$1 \times 10^{-3}$	$\text{mg}_{\text{DCF}} \cdot \text{L}^{-1}$	Specified
$K_{I,\text{DCF}}$	Inhibition constant for DCF	5.0	$\text{mg}_{\text{DCF}} \cdot \text{L}^{-1}$	Specified
$k_H$	EPS hydrolysis rate	$7.08 \times 10^{-3}$	$\text{h}^{-1}$	Ni <i>et al.</i> (2008)
$Y_H$	Biomass yield	0.4928	$\text{mg}_{\text{COD}} \cdot \text{mg}_{\text{COD}}^{-1}$	Experimental
$Y_E$	EPS yield	0.20	$\text{mg}_{\text{COD}} \cdot \text{mg}_{\text{COD}}^{-1}$	Lardon <i>et al.</i> (2011)
$b_{\text{res},H}$	Endogenous respiration rate	$1.33 \times 10^{-2}$	$\text{h}^{-1}$	Wanner <i>et al.</i> (2006)
$b_H$	Decay rate	$2.06 \times 10^{-2}$	$\text{h}^{-1}$	Experimental
Autotrophs (A)				
$\mu_{\max,A}$	Max. specific growth rate	$4.17 \times 10^{-2}$	$\text{h}^{-1}$	Rittmann <i>et al.</i> (2004)
$K_{N,A}$	Saturation constant for $\text{NH}_4$	1.5	$\text{mg}_N \cdot \text{L}^{-1}$	Wanner <i>et al.</i> (2006)
$K_{O,A}$	Saturation constant for $\text{O}_2$	0.5	$\text{mg}_{\text{O}_2} \cdot \text{L}^{-1}$	Wanner <i>et al.</i> (2006)
$k_H$	EPS hydrolysis rate	$7.08 \times 10^{-3}$	$\text{h}^{-1}$	Ni <i>et al.</i> (2008)
$Y_A$	Biomass yield	0.24	$\text{mg}_{\text{COD}} \cdot \text{mg}_N^{-1}$	Rittmann <i>et al.</i> (2004)
$Y_E$	EPS yield	0.18	$\text{mg}_{\text{COD}} \cdot \text{mg}_{\text{COD}}^{-1}$	Lardon <i>et al.</i> (2011)
$b_{\text{res},A}$	Endogenous respiration rate	$5 \times 10^{-3}$	$\text{h}^{-1}$	Wanner <i>et al.</i> (2006)
$b_A$	Decay rate	$1.25 \times 10^{-3}$	$\text{h}^{-1}$	Wanner <i>et al.</i> (2006)
Particulates				
$\rho_X$	Density of biomass	$200 \times 10^3$	$\text{mg} \cdot \text{L}^{-1}$	Xavier <i>et al.</i> (2005a)
$\rho_I$	Density of inert biomass	$200 \times 10^3$	$\text{mg} \cdot \text{L}^{-1}$	Xavier <i>et al.</i> (2005a)
$\rho_{\text{EPS}}$	Density of EPS	$33 \times 10^3$	$\text{mg} \cdot \text{L}^{-1}$	Xavier <i>et al.</i> (2005a)
Mass transfer				
$D_f$	Biofilm diffusivity factor	0.8	-	Lardon <i>et al.</i> (2011)
$D_{\text{O}_2}$	Diffusivity of oxygen	$4.76 \times 10^{-3}$	$\text{m}^2 \cdot \text{h}^{-1}$	Lardon <i>et al.</i> (2011)
$D_{\text{NH}_4}$	Diffusivity of ammonia	$4.05 \times 10^{-3}$	$\text{m}^2 \cdot \text{h}^{-1}$	Lardon <i>et al.</i> (2011)
$D_{\text{NO}_3}$	Diffusivity of nitrate	$4.05 \times 10^{-3}$	$\text{m}^2 \cdot \text{h}^{-1}$	Lardon <i>et al.</i> (2011)
$D_S$	Diffusivity of substrate	$2.38 \times 10^{-3}$	$\text{m}^2 \cdot \text{h}^{-1}$	Lardon <i>et al.</i> (2011)
$D_{\text{DCF}}$	Diffusivity of diclofenac	$5.95 \times 10^{-3}$	$\text{m}^2 \cdot \text{h}^{-1}$	Estimated <sup>1</sup>
$L_L$	Mass transfer boundary layer thickness	48	$\mu\text{m}$	Alpkvist <i>et al.</i> (2006)
$k_{\text{Det}}$	Erosion strength	$1 \times 10^{-3}$	$\text{fg} \cdot \mu\text{m}^{-4} \cdot \text{h}^{-1}$	Xavier <i>et al.</i> (2005a)
Computation domain				
$L_X \times L_Z \times L_Y$	System size	264	$\mu\text{m}^3$	Specified
$N_X \times N_Z \times N_Y$	Number of grid elements	33	-	Specified
$x \times z \times y$	Size of solute grid element	8	$\mu\text{m}$	Specified
$i \times j \times k$	Size of agent grid element	4	$\mu\text{m}$	Specified
$L_{f,\text{max}}$	Maximum biofilm thickness	400	$\mu\text{m}$	Specified
$D$	Dilution rate	18	$\text{h}^{-1}$	Calculated
$\sigma_R$ <sup>2</sup>	Specific area of flow cell	1474	$\text{m}^2 \cdot \text{m}^{-3}$	Calculated

<sup>1</sup> Estimated using general correlation for unassociated liquids equation from Wilke and Chang (1955).<sup>2</sup> Describes the ratio between the carrier surface (substratum on which the biofilm grows) and the bulk compartment volume.

**Table 4.2.** Stoichiometric matrix and kinetic expressions used for the biofilm model

Reaction	Soluble components				Particulate components				Kinetic Expression
	S <sub>S</sub>	S <sub>O</sub>	S <sub>NH<sub>4</sub></sub> <sup>+</sup>	S <sub>NO<sub>3</sub></sub> <sup>-</sup>	X <sub>H</sub>	X <sub>A</sub>	X <sub>EPS</sub>	X <sub>I</sub>	
Aerobic heterotroph growth <sup>1</sup>	− $\frac{1}{Y_H}$	− $\frac{1 - Y_H}{Y_H}$			Y <sub>H</sub>		Y <sub>E</sub>		$\mu_{\max,H} \frac{S_S}{K_S + S_S} \frac{S_O}{K_O + S_O} j_{Inh} X_H + \mu_{DCF} j_{Hal} \frac{S_O}{K_O + S_O} X_H$
Heterotroph endogenous respiration		−1				−1			$b_{res,H} \frac{S_O}{K_O + S_O} X_H$
Heterotroph decay					−1			1	$b_H X_H$
Autotroph growth	− $\frac{4.57 - Y_A}{Y_A}$	− $\frac{1}{Y_A}$	$\frac{1}{Y_A}$		Y <sub>A</sub>		Y <sub>E</sub>		$\mu_{\max,H} \frac{S_N}{K_N + S_N} \frac{S_O}{K_O + S_O} X_H$
Autotroph endogenous respiration		−1				−1			$b_{res,A} \frac{S_O}{K_O + S_O} X_H$
Autotroph decay					−1		1		$b_A X_A$
EPS decay	1					−1			$K_{Hyd} X_{EPS}$

<sup>1</sup> The following kinetic equations were only implemented for treatment simulations.

$$j_{Hal} = \frac{S_{DCF}}{K_{S,DCF} + S_{DCF} + \frac{S_{DCF}^2}{K_{I,DCF}}} ; j_{Inh} = \frac{K_{I,DCF}}{K_{I,DCF} + S_{DCF}}$$

**Table 4.3.** Input parameters for biofilm simulations

Inputs	Description	Value	Units	Reference
<i>Biomass components</i> <sup>1</sup>				
$n_{X,H,t0}$	Initial number of heterotroph cells	8	-	Specified
$n_{X,A,t0}$	Initial number of autotroph cells	4	-	Specified
<i>Solute components</i> <sup>2</sup>				
$S_{in,O_2}$	Bulk concentration of O <sub>2</sub>	5	mg <sub>O<sub>2</sub></sub> .L <sup>-1</sup>	Experimental
$S_{in,COD}$	Bulk concentration of COD	120	mg <sub>COD</sub> .L <sup>-1</sup>	Experimental
$S_{in,NH_4}$	Bulk concentration of NH <sub>4</sub>	16	mg <sub>N</sub> .L <sup>-1</sup>	Experimental
$S_{in,NO_3}$	Bulk concentration of NO <sub>3</sub>	0	mg <sub>N</sub> .L <sup>-1</sup>	Specified
$S_{in,DCF,low}$ <sup>3</sup>	Bulk concentration of DCF for 0.1 mg L <sup>-1</sup> run	0.1	mg <sub>DCF</sub> .L <sup>-1</sup>	Experimental
$S_{in,DCF,high}$ <sup>3</sup>	Bulk concentration of DCF for 10 mg L <sup>-1</sup> run	10	mg <sub>DCF</sub> .L <sup>-1</sup>	Experimental

<sup>1</sup>The initial number of particles was adjusted such that the predicted and experimental parameter profiles matched.

<sup>2</sup>Solute concentrations were set the same for influent and initial state of bulk compartment.

<sup>3</sup>Only implemented for treatment simulations.

#### 4.1.9 Biofilm parameter calculations

Before biofilm parameter calculations, the CLSM datasets were pre-processed to remove background noise (Figure 4.3). First, images below the substratum were removed from the image stack. To smooth the edges of the biofilm and reduce noise, CLSM datasets were processed through a 2D median filter with a 5-by-5 pixel neighbourhood. This was performed in MATLAB using the built-in function, *medfilt2*. This step was vital for accurate calculation of *s/v* ratio. Due to the relatively large interval between Z-stacks, the fluorescence emitted by biomass was stretched in the Z-direction resulting in an artificially high surface area. Of course, this issue can be avoided with a smaller Z-interval, but this would drastically increase image acquisition times to an unreasonable level considering the number of image stacks required per flow channel. Following this, thresholding of image stacks was performed manually. A fixed threshold value (pixel intensity) was determined by the user to exclude background noise. Finally, planktonic cells and background noise not removed by thresholding were removed using connected-volume filtration. This removed any biomass pixels which are not in some way connected to the substratum (Heydorn *et al.*, 2000b).

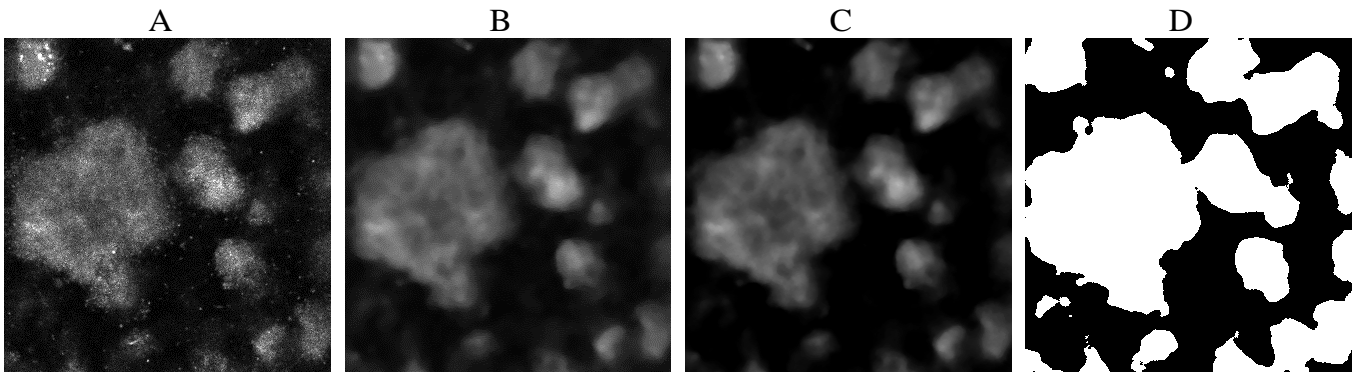


**Figure 4.3.** Confocal laser photomicrographs of biofilm depicting steps in processing CLSM image stacks prior to parameter calculations. **A.** Raw image. **B.** Median filtered. **C.** Thresholded. **D.** Binarised: white represents biomass, black represents background. All parameters were calculated for binary images, except for total biomass which utilised the range in pixel values in C.

COMSTAT 1.2, implemented in MATLAB, was used to calculate biofilm structure parameters of each CLSM image stack (Heydorn *et al.*, 2000b). Since the biofilm is simulated in a 3D domain, the output can be analysed in a similar manner to CLSM data, making comparative studies easier. The COMSTAT script and associated functions were modified to handle the simulation output for calculating biofilm parameters.

The following biofilm structure parameter set was used for comparisons:

- Average biofilm thickness,  $\bar{L}_f$  is the mean of biofilm height above the substratum.
- Substratum coverage,  $c_f$ , is the fraction of substratum colonised by the biofilm.
- Surface area-to-biovolume ratio,  $s/v$ , is the surface area of the biofilms surface divided by the biovolume. Biovolume ( $\mu\text{m}^3$ ) is defined as the sum of pixels containing biomass multiplied by the voxel size. This parameter indicates what fraction of the biofilm is exposed to bulk liquid nutrients, and can give insight into how the biofilm adapts to the environment.
- Total biomass,  $B$ , is the sum of the mass of biofilm (in  $\mu\text{g}$ ) per unit area of substratum. For simulation and experimental data,  $B$  was calculated using eq. 19 and 20, respectively.

$$B_{\text{sim}} = \sum_{i=1}^{66} \sum_{j=1}^{66} \sum_{k=1}^{66} C_{x,y,z} \cdot V_{\text{voxel}} / A_{\text{substratum}} \quad (19)$$

$$B_{\text{exp}} = \sum_{i=1}^{512} \sum_{j=1}^{512} \sum_{k=1}^{512} F(gv_{i,j,k}) \cdot \rho_{\text{biomass}} V_{\text{voxel}} / A_{\text{substratum}} \quad (20)$$

where  $C_{x,y,z}$  is the concentration of biomass particles at coordinates  $x,y,z$  in the computation domain of the biofilm model, and  $gv_{i,j,k}$  is the greyvalue of the voxel at entries  $i,j,k$  on the 3D matrix defined by the CLSM image stack. The function  $F$  converts greyvalues ( $gv_{i,j,k}$ ) from the [0,255] range to the [0,1] range (Xavier *et al.*, 2004). Instead of calculating total biomass as biovolume per substratum area ( $\mu\text{m}^3 \cdot \mu\text{m}^{-2}$ ), it was decided to utilise the greyscale pixel intensity range in the CLSM datasets to calculate a mass per unit area parameter ( $\mu\text{g} \cdot \mu\text{m}^{-2}$ ). This provided a more accurate estimation of the biomass present in the biofilm.

- Roughness coefficient,  $R_\alpha$ , is a dimensionless measure of the variability in biofilm thickness, and is an indicator of biofilm heterogeneity (Heydorn *et al.*, 2000b). Defined by eq. 21.

$$R_\alpha = \frac{1}{n} \sum_{i=1}^n \frac{|L_{fi} - \bar{L}_f|}{\bar{L}_f} \quad (21)$$

where  $n$  is the number of thickness measurements,  $L_{fi}$  is the  $i$ th individual thickness measurement, and  $\bar{L}_f$  is the mean thickness. A higher value indicates an irregular surface whereas a value approaching zero represents a smooth, flat surface.

#### 4.1.10 Statistical analysis of biofilm parameters

Statistical analysis of data was performed in GraphPad Prism®. LCMS data was analysed using two-way ANOVA with a  $P$ -value of 0.05. The Shapiro-Wilk test was used to check data sets for normality. Differences between biofilm parameter values for all data sets were calculated using an unpaired  $t$ -test (normal distribution) or Mann-Whitney test (non-normal distribution) with a  $P$ -value of 0.05, unless stated otherwise. Coefficients of determination ( $R^2$ ) were calculated for validation comparison.

## 4.2 Results

### 4.2.1 Validation

Selected biofilm CLSM images are depicted in Figure 4.4. Following 26.5 h of incubation, individual cells have attached to the substratum and have divided to form the early stages of a microcolony. By 45.5 h, most of the substratum has been colonised and a few microcolonies have grown in size to form mounds. Here, one can see the variety of bacterial phenotypes forming part of the mixed-species biofilm.

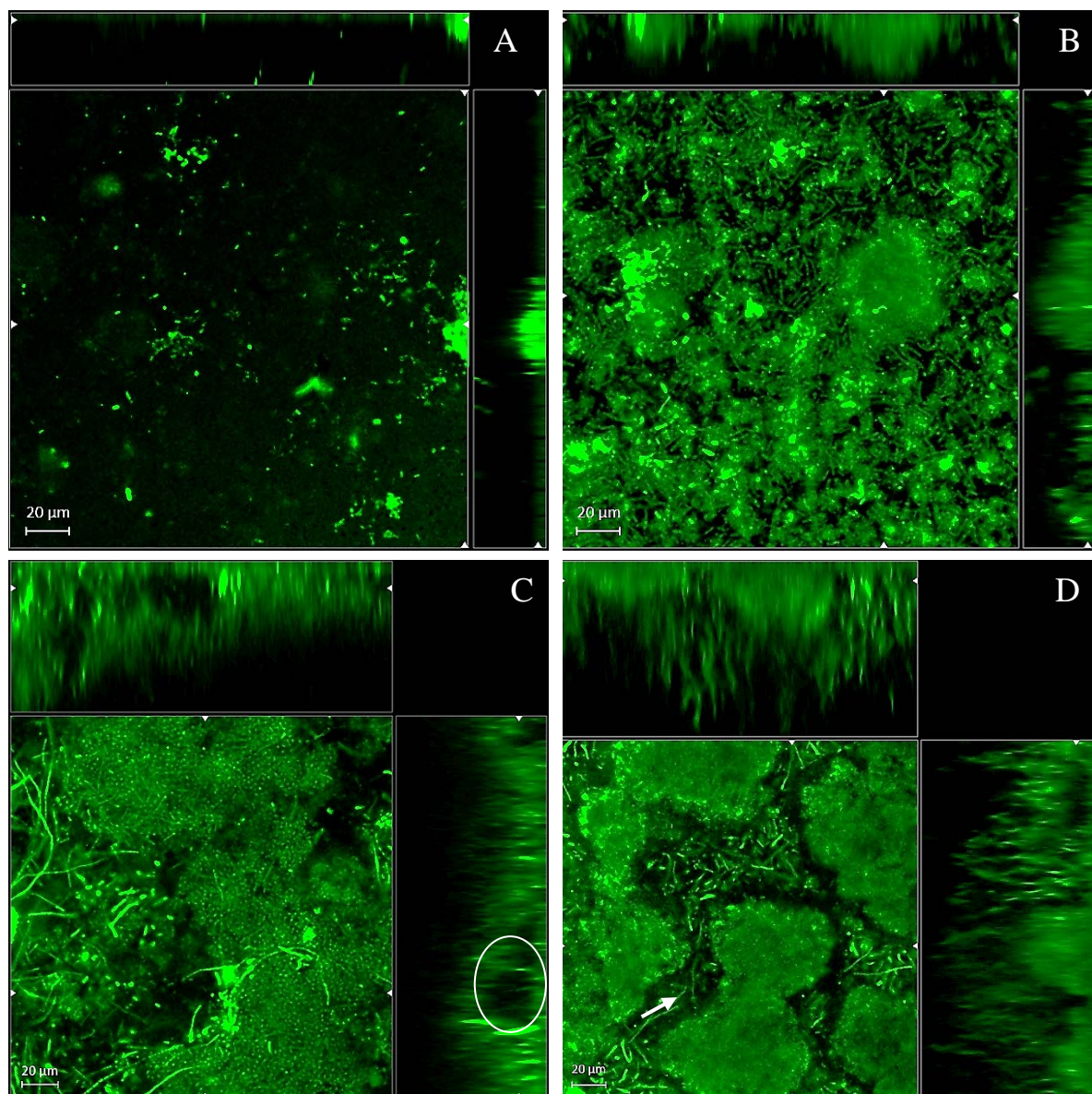


**Figure 4.4.** Representative confocal laser photomicrographs of multispecies biofilm development at **A.** 26.5, **B.** 45.5, **C.** 70.5, and **D.** 94.5 hours of growth under control conditions. Shown is orthogonal view where central plots are top views while upper and right frames are vertical sections through the biofilm at positions indicated by the white triangles. Scale bars are also valid for upper and right frames.

Following 70.5 h of growth, the biofilm has increased in thickness significantly. Here the majority of the biofilm was made up of coccoid-shaped cells. Voids have begun to develop within the biofilm (indicated by the white circle). At 94.5 h, the biofilm has developed a complex structure with distinct microcolonies separated by a network of channels which were occupied by a loose mass of mainly rod-shaped bacteria (indicated by the white arrow).

Rendered images of the simulated biofilm are shown in Figure 4.5. Throughout the simulation, heterotrophs dominated in the biofilm. This corresponds well with batch culture observations. At 72 h, heterotrophs were localised near the surface of the biofilm where they have better access to oxygen. EPS formed a significant proportion of the biofilm. Similar to the experimental biofilm (Figure 4.4), the simulated biofilm has formed mound-like microcolonies at 48 h and has colonised most of the substratum at 72 h.

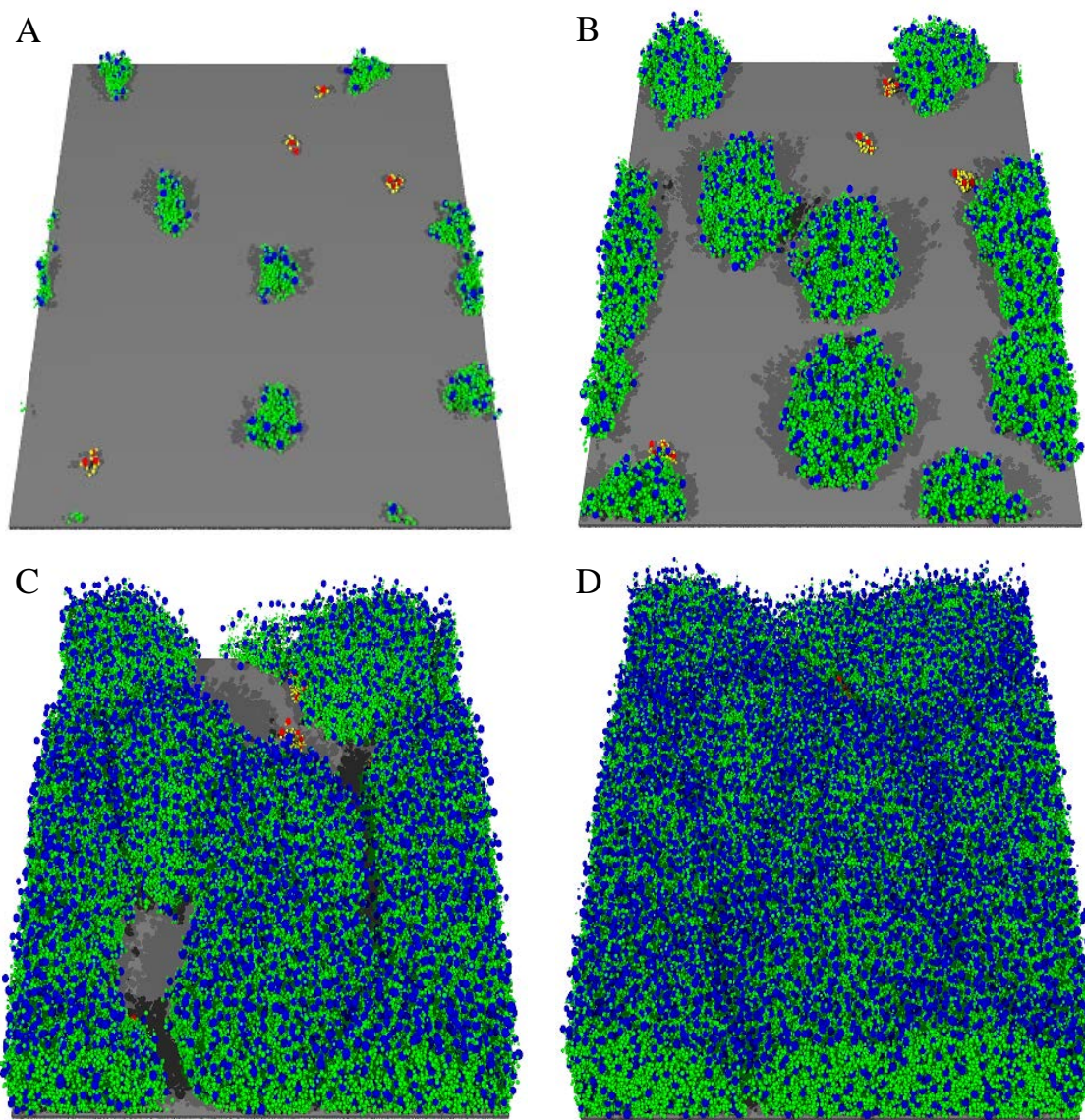


**Figure 4.5.** Simulated biofilm at **A.** 24, **B.** 48, **C.** 72, and **D.** 96 hours of growth. Images are perspective projections of the 3D computational domain of the iDynoMiCS model. Blue particles represents lumped heterotrophs, green represents heterotroph EPS, red represents autotrophs, and yellow represents autotroph EPS.

Comparison between biofilm parameters for experimental and simulated biofilm are depicted in Figure 4.6 and the corresponding scatter plots for each parameter indicating individual measurements are shown in Figure C1. Besides outliers, individual

measurements are reasonably well clustered for all structural parameters, though the variance increased at 70.5 and 94.5 h (Figure C1). Initial biofilm development in the flow cells was characterised by a lag period followed by an exponential increase in  $\bar{L}_f$  and  $B$  at approximately 25 h. The biofilm surface is initially heterogeneous and trends towards a flatter surface as the biofilm matures. There was a rapid increase in horizontal spreading on the substratum after 26 h, which switched to a gradual linear increase to cover 80% of the surface after 94.5 h of growth (Figure 4.6D).

The simulation output fits well to the general trend of experimental biofilm parameters, except for the  $s/v$  ratio (Figure 4.6). The fit was good for  $\bar{L}_f$  and  $R_a$ . After around 60 h,  $\bar{L}_f$  shifts from an exponential to a linear increase. This was due to the depletion of oxygen in the bulk liquid which led to oxygen-limited growth. As the  $s/v$  ratio decreased and the mean thickness increased, the base of the biofilm became oxygen-limited, leaving only cells near the surface growing at their maximum rate. For  $B$ , the fit was initially good but was subsequently overestimated. The  $s/v$  ratio was significantly underestimated ( $R^2$  not calculated) by the model, although it did follow the same downward trend (Figure 4.6E). The calculated surface area for CLSM datasets was significantly higher than for the simulation (data not shown), which contributed to the higher  $s/v$  ratio.

As expected, preliminary 2D simulations ran using identical parameters did not replicate observed biofilm structure (data not shown), and thus, were not ideal for simulating biofilm structure.

The effect of stochasticity on predicted structural parameters is shown in Figure D1. The profiles were not significantly affected by stochastic effects. The sensitivity of structural parameters to changes in simulation inoculation numbers and  $k_{Det}$ , which had suspected uncertainty, are depicted in Figure D2 and Figure D3, respectively. All structural parameters were sensitive to changes in simulation inoculation numbers. An increase in inoculation numbers shifted the profile along the x-axis (time), but did not alter the shape of the profiles (Figure D2). The inoculation number was therefore adjusted so that the simulation profile matched the observed data.

Changes in  $k_{Det}$  drastically altered the profile of  $\bar{L}_f$  and  $B$ , but did not significantly affect  $R_a$  and  $c_f$  (Figure D3). An increase in  $k_{Det}$  correlated with a decrease in biomass by limiting the thickness that the biofilm could reach.

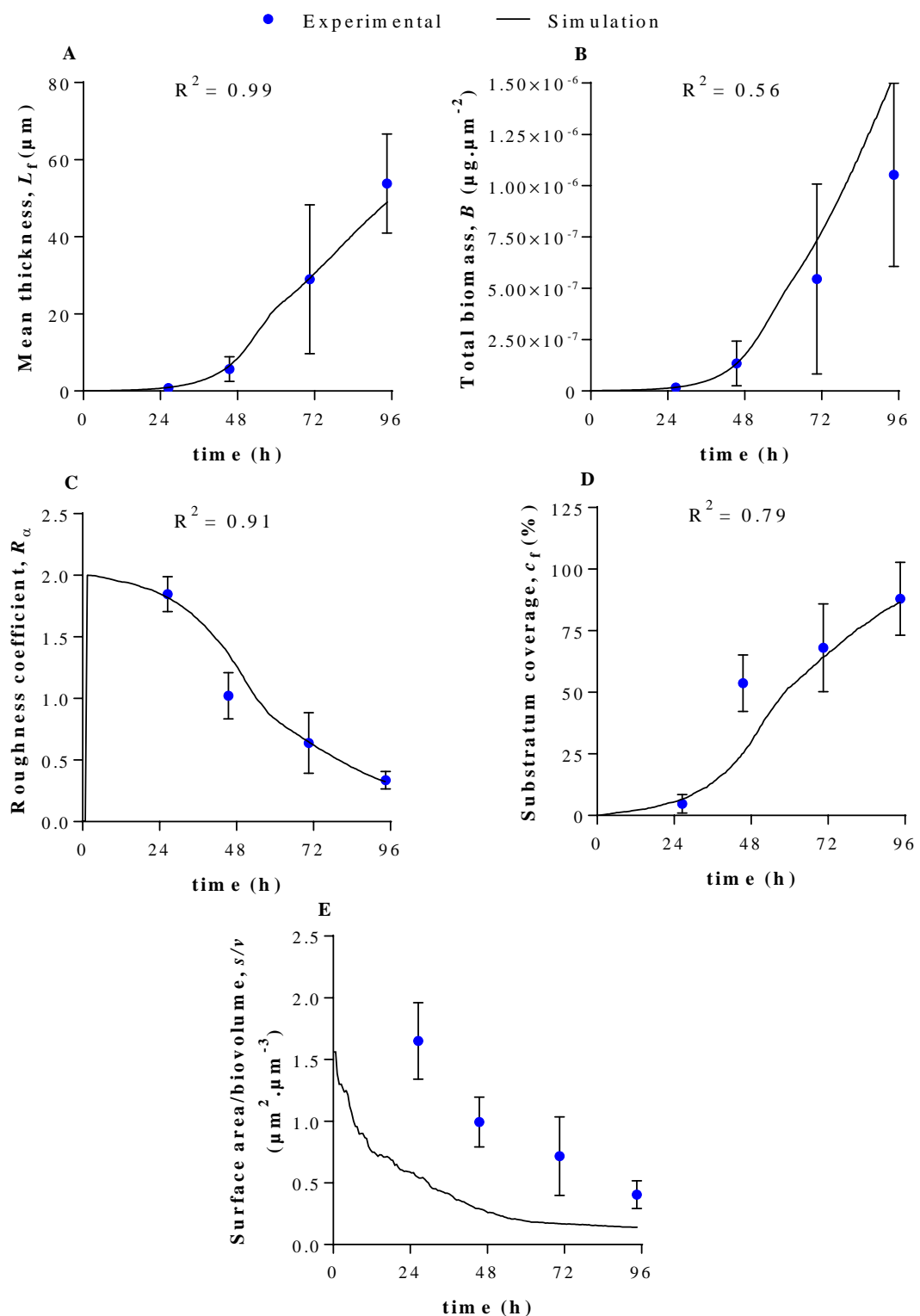


**Figure 4.6.** Comparison between experimental and simulated biofilm parameters for biofilms cultivated under control conditions. **A.** Mean thickness. **B.** Total biomass per substratum area. **C.** Roughness coefficient. **D.** Substratum coverage. **E.** Surface area/biovolume ratio. Experimental time points are at 26.5, 45.5, 70.5, and 94.5 h. Error bars indicate 1 standard deviation.

#### 4.2.2 Diclofenac treatments

The endpoint response of the batch culture to DCF exposure is shown in Figure 4.7. Although insignificant ( $P>0.05$ ), when exposed to  $5 \mu\text{g.L}^{-1}$ , the CFU/mL increased relative to the control, whereas exposure to  $5 \text{ mg.L}^{-1}$  resulted in a decrease in CFU/mL. The majority of colonies plated out from the culture were a cream colour. A few motile bacteria were observed and one filamentous (fungal) colony.

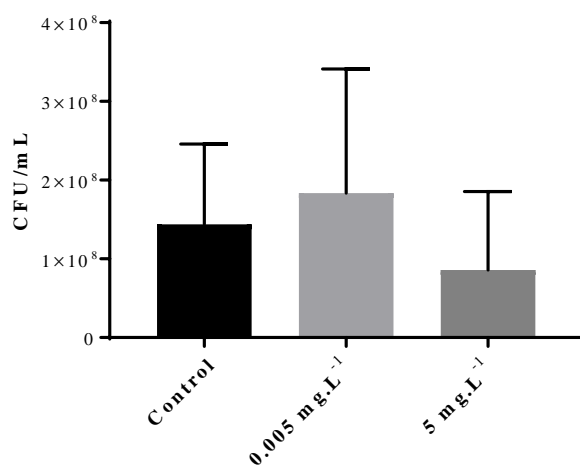


**Figure 4.7.** Response of batch culture following 32 h exposure to DCF at  $0.005$  and  $5 \text{ mg.L}^{-1}$ . There is no significant difference between control and treatments.

Biofilms were cultivated for 72 h under control conditions after which DCF was introduced for a further 24 h. Selected CLSM images are depicted in Figure 4.8. In the control biofilm, the majority of the surface was colonised by regularly occurring mound-shaped microcolonies (Figure 4.8A). The vast majority of the biofilm was composed of coccoid-shaped cells. Treatment with  $10 \text{ mg.L}^{-1}$  DCF resulted in a comparatively lower surface colonisation and a more heterogeneous structure (Figure 4.8B). Treatment with  $0.1 \text{ mg.L}^{-1}$  DCF resulted in a more heterogeneous structure as well, but the microcolonies appeared to be more densely colonised (Figure 4.8C). In Figure 4.8D, parts of the biofilm were colonised by relatively large spherical cells, presumed to be protists (white arrows). Subsequent references to these entities are speculative. Although observed in other parts of the biofilm, and in different flow cells, this was the highest concentration of protozoa found. Microcolonies were less defined and zones of clearance with EPS remaining can be observed as a result of protist grazing. There was also a lower bacterial abundance compared to biofilms not colonised by protists.

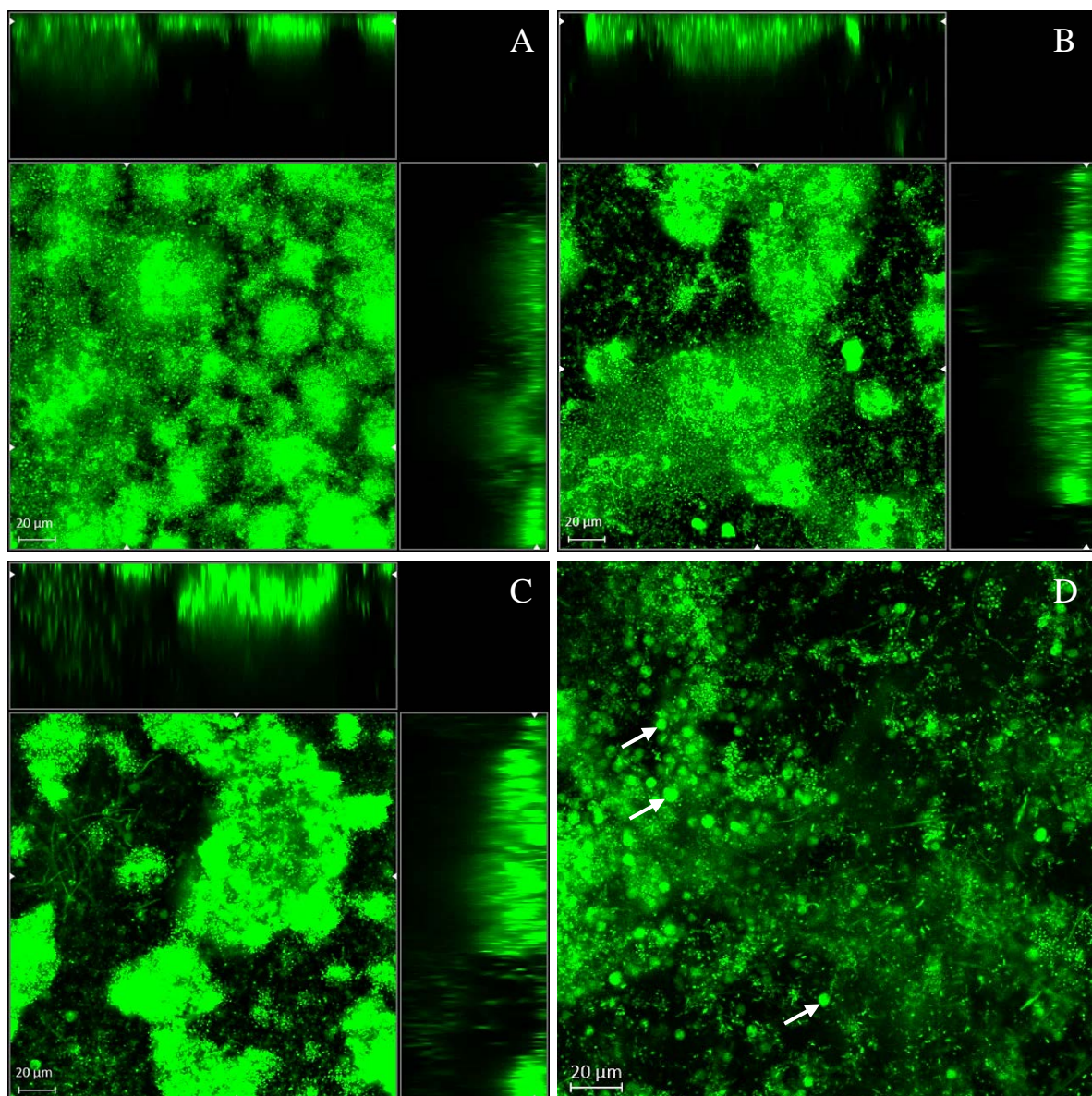


**Figure 4.8.** Representative confocal laser photomicrographs of multispecies biofilm structure after 4 d of growth. **A.** Control. **B.** Following 24 h exposure to  $10 \text{ mg.L}^{-1}$  DCF. **C.** Following 24 h exposure to  $0.1 \text{ mg.L}^{-1}$  DCF. **D.** Presumptive protists (white arrows) grazing on biofilm. Shown is orthogonal view where central plots are top views while upper and right frames are vertical sections through the biofilm at positions indicated by the white triangles. Scale bars are also valid for upper and right frames.

Experimental structural parameters of biofilms exposed to DCF are shown in Figure 4.9 and Figure 4.10. When biofilms were exposed to  $10 \text{ mg.L}^{-1}$  DCF, a significant decrease in  $\bar{L}_f$  (-31%),  $B$  (-33%), and  $c_f$  (-56%) was observed for all temporal measurements (Figure 4.9). The decrease following 24 h of exposure is indicated in parentheses. The decrease in  $c_f$  can be clearly seen in the CLSM image as well (Figure 4.8B). Conversely, there was a significant increase in  $R_a$  (198%) and  $s/v$  ratio (71%) of the biofilm compared to the control. This is indicative of a more heterogeneous biofilm with a larger surface area

exposed to the bulk liquid. Overall, exposure at this concentration resulted in a thinner, less dense, and more disperse biofilm which suggests an inhibitory effect.

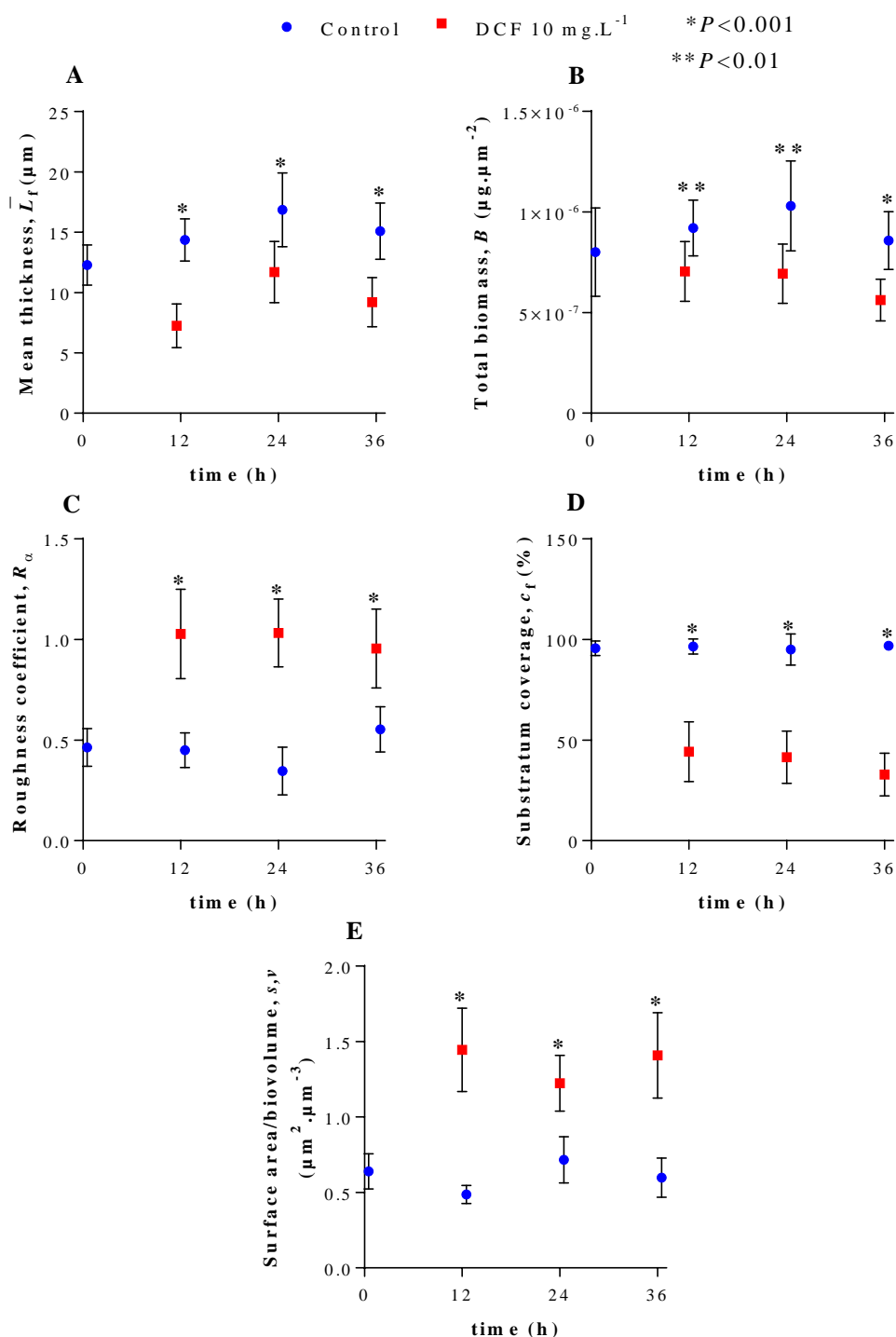


**Figure 4.9.** Experimental structure parameters of biofilm exposed to 10 mg.L<sup>-1</sup> diclofenac compared to control. **A.** Mean thickness. **B.** Total biomass per substratum area. **C.** Roughness coefficient. **D.** Substratum coverage. **E.** Surface area/biovolume ratio. The first control measurement was taken immediately after exposure of 72 h old biofilms to diclofenac. Each data point represents the average of the respective parameter. Error bars indicate 1 standard deviation. Data was shifted by 0.5 h to avoid overlap of error bars.

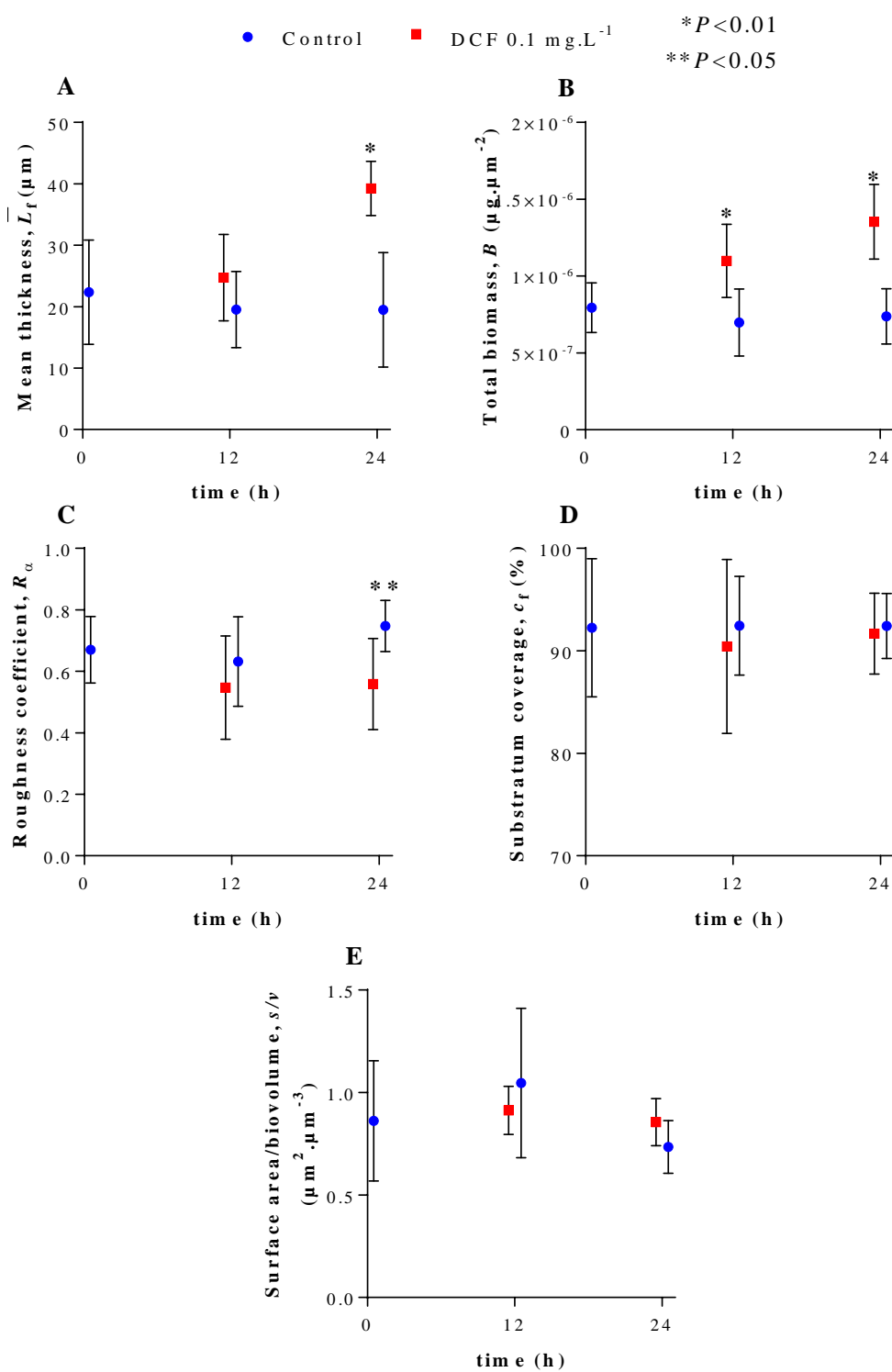


**Figure 4.10.** Experimental structure parameters of biofilm exposed to 0.1 mg.L<sup>-1</sup> diclofenac compared to control. **A.** Mean thickness. **B.** Total biomass per substratum area. **C.** Roughness coefficient. **D.** Substratum coverage. **E.** Surface area/biovolume ratio. The first control measurement was taken immediately after exposure of 72 h old biofilms to diclofenac. Each data point represents the average of the respective parameter. Error bars indicate 1 standard deviation. Data was shifted by 0.5 h to avoid overlap of error bars.

When exposed to a lower concentration of  $0.1 \text{ mg.L}^{-1}$ , a significant increase in  $\bar{L}_f$  (102%) and  $B$  (83%) compared to the control was observed at 24 h of DCF exposure (Figure 4.10). The  $\bar{L}_f$  and  $B$  of the control biofilm remained static, but increased over time for the DCF-treated biofilm. This indicated an overall increase of biofilm growth. Following 12 h of exposure, there was a slight, but not significant ( $P=0.0665$ ), increase in  $\bar{L}_f$ . A minor decrease in  $R_a$  (-25%) was observed at 24 h of exposure. No change was observed for  $c_f$  and  $s/v$  ratio over the exposure period. The final measurement at 36 h was not available due to bubble damage. Although the simulation did not fit well to experimental  $s/v$  ratio in the validation experiment (Figure 4.6), it was still a useful parameter for assessing the biofilm's response to DCF exposure.

The concentration of DCF detected in the influent and effluent of a flow cell during the  $0.1 \text{ mg.L}^{-1}$  run is shown in Figure 4.11. After the experiment was completed, additional influent measurements were taken to check for stability in the medium. Although DCF was added to the influent flask at a final concentration of  $125 \mu\text{g.L}^{-1}$ , it was detected in the influent at  $84 \mu\text{g.L}^{-1}$ . However, the results were not integrated against an internal standard, so loss of DCF during the extraction and elution procedures could not be accounted for. Therefore, only relative concentrations were addressed subsequently. DCF remained stable in the influent; there was no significant abiotic degradation over 5 d (Figure 4.11). There was no significant difference between influent and effluent over the treatment period ( $P>0.05$ ). Although insignificant, the effluent concentration is slightly higher compared to the influent at 10 h and 24 h.

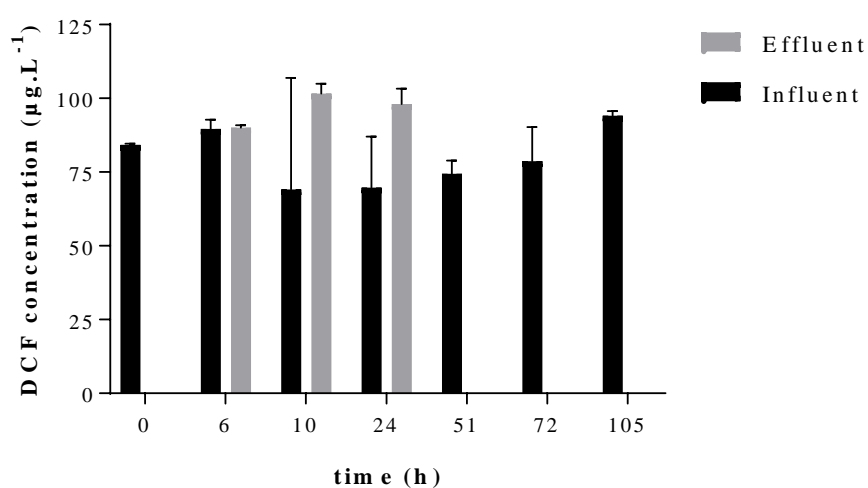


**Figure 4.11.** Concentration of DCF in the influent and effluent of flow cells from the  $0.1 \text{ mg.L}^{-1}$  treatment run. Indicated is the time elapsed from DCF exposure to 72 h old biofilms. There was no significant difference between and within influent and effluent measurements.

A direct comparison between predicted and observed structural parameters of biofilms exposed to  $10 \text{ mg.L}^{-1}$  and  $0.1 \text{ mg.L}^{-1}$  DCF is depicted in Figure 4.12 and 4.13, respectively. The predictions for  $\bar{L}_f$  and  $c_f$  did not match experimental observations directly for both treatments. The  $10 \text{ mg.L}^{-1}$  treatment prediction for  $B$  fits well to experimental observations, but was overestimated in the control (Figure 4.12B), as it was in the validation run (Figure 4.6B). The control prediction for  $R_o$  fits well, but was underestimated for the treatment simulation for  $10 \text{ mg.L}^{-1}$ . Overall, simulations at  $0.1 \text{ mg.L}^{-1}$  did not fit experimental observations well (Figure 4.13). Although the biofilm model did not match the experimental parameter profiles, the expected qualitative effect was reproduced.

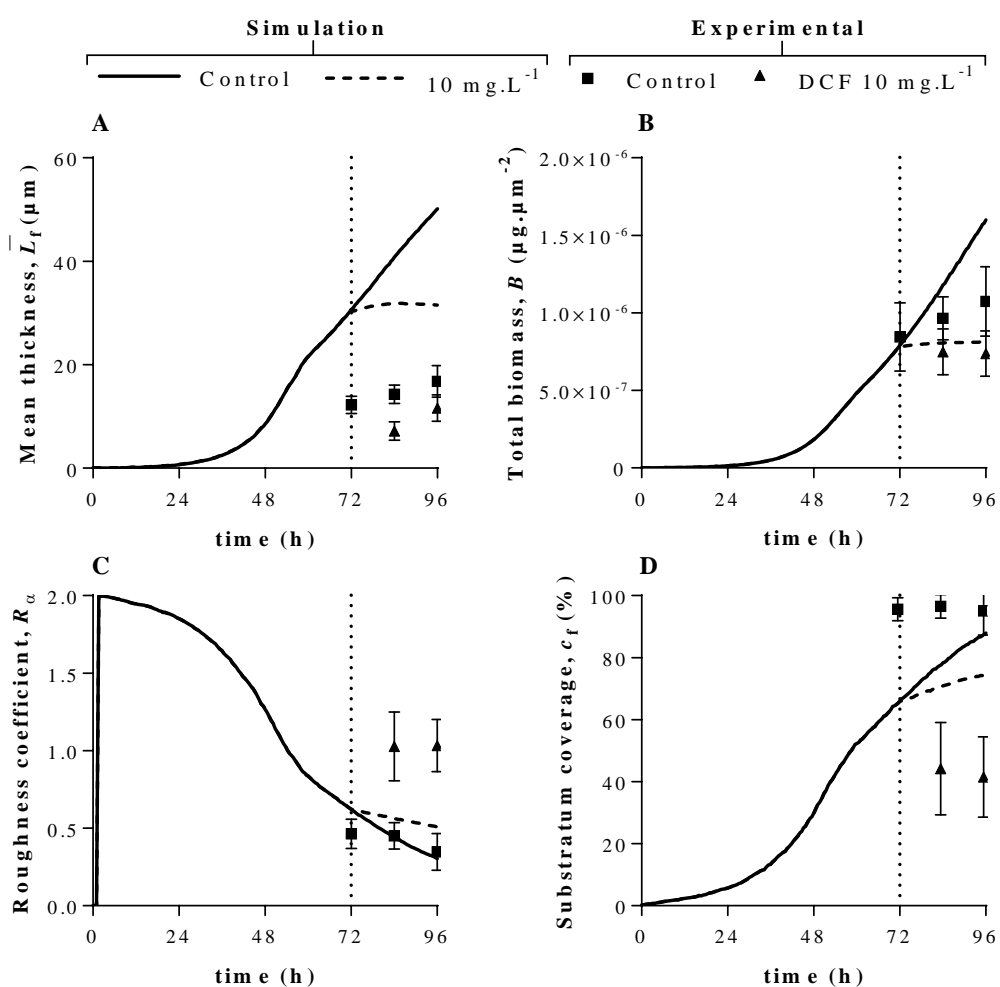


**Figure 4.12.** Experimental and simulated biofilm structural parameters for control and treatment at  $10 \text{ mg.L}^{-1}$  DCF. **A.** Mean thickness. **B.** Total biomass. **C.** Roughness coefficient. **D.** Substratum coverage. DCF was introduced at 72 h (indicated by dotted line).

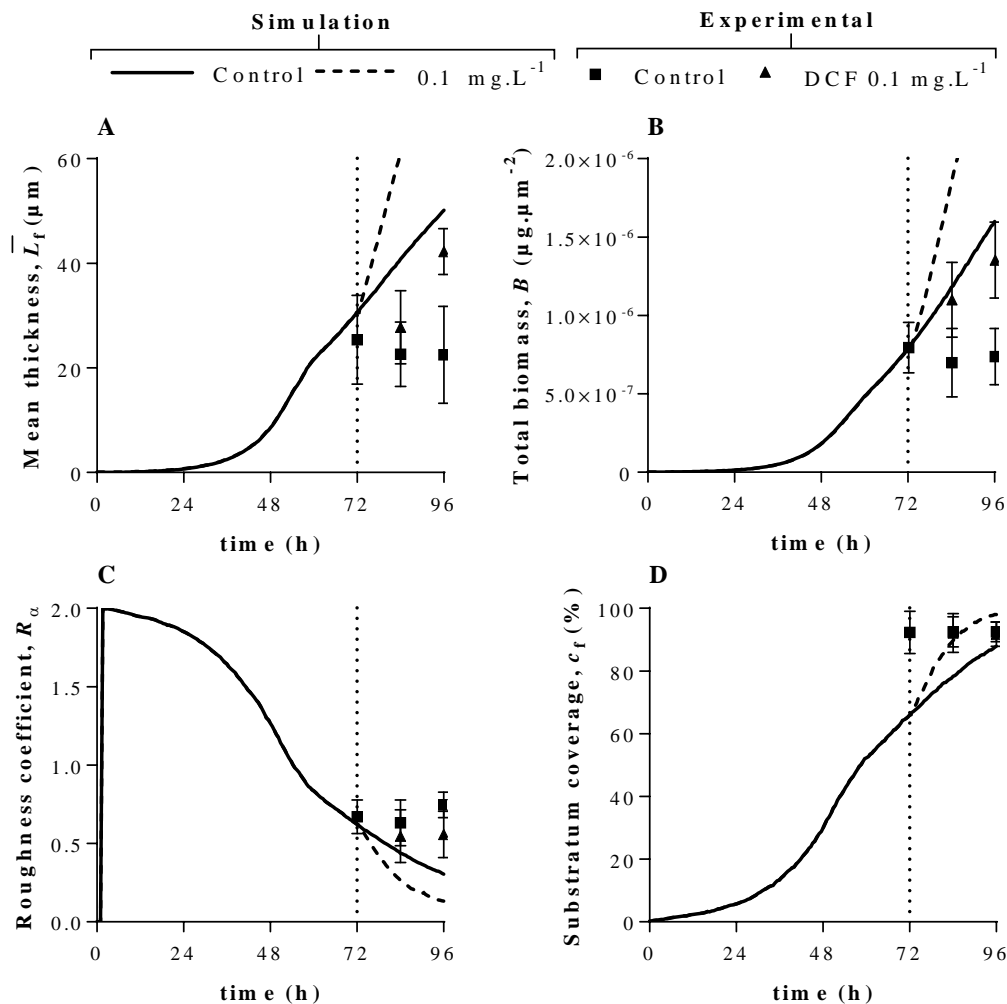


**Figure 4.13.** Experimental and simulated biofilm structural parameters for control and treatment at  $0.1 \text{ mg.L}^{-1}$  DCF. **A.** Mean thickness. **B.** Total biomass. **C.** Roughness coefficient. **D.** Substratum coverage. DCF was introduced at 72 h (indicated by dotted line).

DCF exposure experiments reached a lower steady-state  $\bar{L}_f$  compared to the validation run (Figure 4.12-13). As a result, treatment simulations overestimated observed biofilm thickness. Therefore, instead of direct comparison, a pattern-oriented approach (Grimm *et al.*, 2005) was adopted where fold changes between control and treatment runs were compared for simulation and experimental data at 24 of DCF exposure (Figure 4.14).

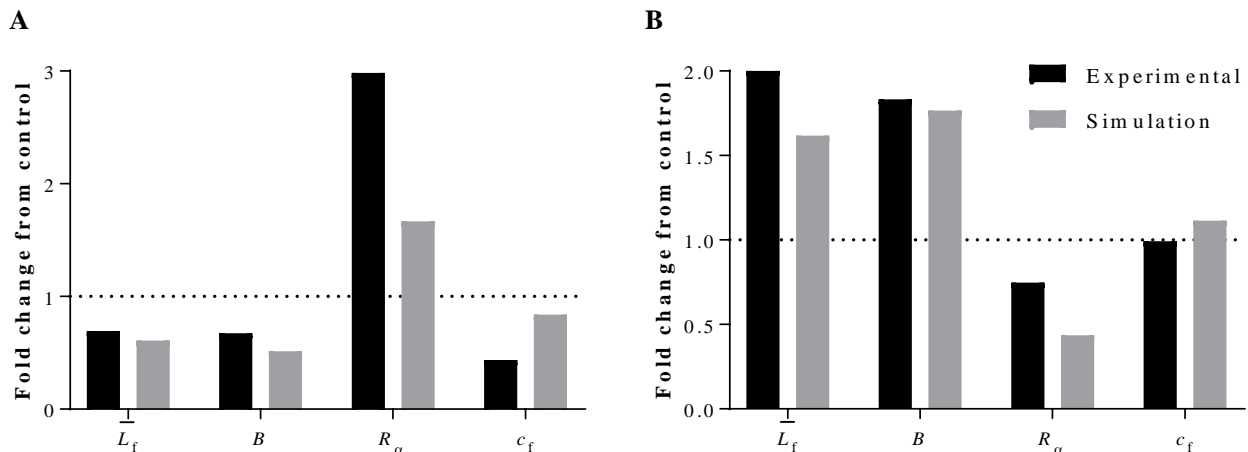


**Figure 4.14.** Fold change in structural parameters of biofilms after 24 h of exposure to **A.**  $10 \text{ mg.L}^{-1}$  and **B.**  $0.1 \text{ mg.L}^{-1}$  DCF. Exposure began after 72 h of biofilm growth under control conditions. The dotted line represents the control.

The IbM reproduced the overall trend in experimental fold changes of structural parameters when exposed to  $0.1$  and  $10 \text{ mg.L}^{-1}$  DCF (Figure 4.14). At  $10 \text{ mg.L}^{-1}$  the match for  $\bar{L}_f$  and  $B$  was good, whereas the effect on  $R_\alpha$  and  $c_f$  was underestimated by the model. As for  $0.1 \text{ mg.L}^{-1}$ , the match for  $B$  and  $c_f$  was good while  $\bar{L}_f$  and  $R_\alpha$  was under- and overestimated by the model, respectively.

## CHAPTER 5: DISCUSSION

The respirometric methods used for  $b_H$ ,  $\mu_{max,H}$ ,  $K_s$ , and  $Y_H$  determination, combined with COD (S<sub>S</sub>) and TSS (X<sub>H</sub>) data, proved to be suitable for biokinetic parameter estimation of an unknown environmental sample. The proposed simple batch model described the experimental system well. Simultaneous regression to three stoichiometrically linked response variables was a robust method of parameter estimation. The experimental methods used were relatively fast and simple, but OUR measurement suffered from a lack of automation, and consequently a low OUR measurement frequency. A reactor configuration used by Almeida and Butler (2002) facilitates automated OUR measurements, but this would require more probes than was available in the present study. Overall, the OUR, S<sub>S</sub>, and X<sub>H</sub> profiles (Figure 3.3) were typical for the S<sub>S</sub>/X<sub>H</sub> ratio used (Kappeler and Gujer, 1992, Trojanowicz *et al.*, 2009).

The lag phase observed in the response variable profiles (Figure 3.3) presented a problem for accurate parameter estimation. Typically, datasets are truncated to exclude data points within the lag phase, but doing so in the present study would have left too few data points for regression. The adoption of an acclimation term (Eq. 14) was an ideal solution to this problem as it mimicked early-stage acclimation while retaining the entire dataset for regression. Future studies can avoid a lag period by ensuring that reactors are inoculated with a culture in the exponential phase of growth.

Since it was determined that heterotrophic growth was dominant in the batch reactors, with no sign of autotrophic nitrification (Figure 3.2), it was assumed that the estimated parameters from the NATU dataset were representative of heterotrophic growth only. Thus, the estimated parameters were used for the calibration of lumped heterotrophic growth in the biofilm model. The minor increase in OUR measured in the presence of ATU (Figure 3.2A) may seem insignificant, but there is evidence that some sulphur-reducing heterotrophs are capable of metabolising ATU and using it as an energy source (Robertson *et al.*, 1989). This may explain the increase in OUR when ATU was added. This did not affect parameter estimation since the NATU dataset was used for this purpose.

There was a relatively high level of uncertainty associated with the estimated  $K_s$  value, with large parameter 95% CIs and a CV of 29% for the mean value (Table 3.5). However,  $K_s$  values are typically difficult to determine with precision, given experimental variability and the nature of the Monod equation. Using a respirometric method on a biofilm reactor, Riefler *et al.* (1998) reported a similarly high CV of 33% and an almost identical response surface seen in suspended

growth models. Furthermore, the long valley in the parameter space with respect to  $K_S$  (Figure 3.4), and associated larger confidence region, is characteristic for batch models based on Monod growth kinetics (Vanrolleghem *et al.*, 1995). It was also shown that two standard deviations around the estimated mean of  $K_S$  did not significantly affect the response variable profiles (Figure 3.5). Thus, a CV of 29% is adequate for this parameter. An increase in the frequency of OUR measurements during the sharp decline phase of the respirogram (Figure 3.2A) could improve the precision of  $K_S$  determination. For future experiments, a consistent initial  $S_S/X_H$  ratio would make the decline phase in the respirogram more predictable.

The biokinetic parameters of the sampled culture were determined from batch experiments under suspended growth conditions. This is the simplest and most common method of estimating kinetic parameters for microbial cultures and is commonly used for attached growth (biofilm) models (Riefler *et al.*, 1998). However, concerns have been raised about the suitability of applying biokinetic parameters estimated from suspended growth systems to biofilm models. The IbM does take into account diffusion-reaction limitations and can thus simulate the gradient of metabolic activity observed in real biofilms, as well as individual agent responses to changes in their environment. However, reality is more nuanced than that. Microbial biofilms are known to exhibit an altered gene expression profile compared to suspended growth systems. For example, density-dependent cell-cell signalling can trigger the expression of genes that may redirect resources to producing alternative compounds, such as EPS components (Flemming and Wingender, 2010). Nevertheless, the biofilm model proved to be an ideal approximation of the real life system, but could certainly do with improvements, which is discussed later.

Throughout the simulations, heterotrophs were dominant within the biofilms, with negligible autotrophic growth. This outcome was expected under the chosen nutrient conditions and is consistent with similar simulations in literature (Lardon *et al.*, 2011, Jayathilake *et al.*, 2017). The selection for heterotrophs in the biofilm model corresponds well with batch reactor observations, where heterotrophs were found to dominate as well based on respirometry. Thus, it was assumed that heterotrophs dominated in the flow cell biofilms as well, which were operated under the same conditions as the batch reactors.

Observed biofilm structure, as revealed by CLSM, proved to be useful for IbM validation. The predicted structural parameters fit well to experimental observations for  $\bar{L}_f$ ,  $R_a$ , and  $c_f$  (Figure 4.6). Although the fit is initially good for  $B$ , the IbM overestimated this parameter as

time proceeded (Figure 4.6B). This may be due to the estimated value of  $\mu_{\max,H}$  which was higher than those usually reported for similar systems (Table 3.6). Biokinetic parameters were estimated under batch conditions that favoured fast-growing heterotrophs due to the high carbon/nitrogen ratio. The estimated biokinetic parameters are thus representative of fast-growing heterotrophs and are an ideal approximation for a short term lumped biofilm model, but may not be ideal for simulating longer term scenarios. Biokinetic parameters should rather be estimated from mature, steady-state cultures.

Xavier *et al.* (2004), using a similar IbM to iDynoMiCS, fit the parameters  $\mu_{\max}$  and  $K_{\text{shov}}$  to observed biofilm structural profiles of a multispecies denitrifying consortium. This resulted in a much better fit to observed structural parameters. The fitted  $\mu_{\max}$  parameter was estimated to be  $0.25 \text{ h}^{-1}$  for the first 22 h of growth, and in a separate experiment,  $\mu_{\max}$  was  $0.06 \text{ h}^{-1}$  for the period of 24-40 h of growth (Xavier *et al.*, 2004). Based on observed structural parameters, overall biofilm growth decreased over time, which was observed in the present study as well (Figure 4.6). Future studies should consider fitting uncertain kinetic parameters to experimental data.

The biofilm model assumes that the system is well-mixed with an equal distribution of substrate in the bulk liquid. The flow cell is not a well-mixed system, however. Biofilm near the inlet receives a higher substrate concentration than biofilm downstream. The substrate concentration will gradually decrease from the inlet to outlet as a result of biological consumption. This gradient in biomass growth along the flow channel would be magnified as time progresses, resulting in relatively thicker biofilms near the inlet. Although efforts were made to reduce variation between and within flow channels (Heydorn *et al.*, 2000a), a degree of stratification was still expected which may account for a proportion of the error observed in the calculated structural parameters. Unfortunately, a gradient in biofilm thickness could not be confirmed in this study since individual measurements were taken at random positions within the defined neighbourhood. But, this has been confirmed to occur in literature (Heydorn *et al.*, 2000a). This is a more likely explanation for the overestimation of  $B$  by the simulation (Figure 4.6B). Perhaps the experimental parameter mean is pulled down by measurements captured away from the channel inlet where biomass density is likely lower. The measurement scatter plot (Figure C1) points towards a decrease in reproducibility at 70.5 h and 94.5 h, but this may be indicative of a gradient in biofilm growth described above.

Furthermore, the issue of stratification calls into question the suitability of the specific area parameter ( $\sigma_A$ ) for this system. This parameter serves to scale up the activity of the biofilm

domain, which is a representative volume, to the full reactor scale, and assumes that the reactor is well-mixed (Lardon *et al.*, 2011). Since it is known that a gradient of metabolic activity can develop along the length of the flow channel, applying a uniform  $\sigma_A$  may not be appropriate for simulating biofilm growth in flow systems.

In contrast to *B*, the *s/v* ratio is significantly underestimated by the model (Figure 4.6E). Initially, the experimental *s/v* ratio was much higher (data not shown) than the values reported in Figure 4.6E (before median filtering). This was believed to be artificially high due to the observed stretching effect of fluorescent signals in the z-direction (seen in Figure 4.4) resulting in a large surface area. This effect could be mitigated by decreasing the Z-step between optical sections, but this would significantly increase image acquisition times. Therefore, a median filter was applied to all CLSM images to smooth the surface of the biofilm and bring the surface area in line with reality (Figure 4.3). This also had the benefit of reducing noise that would persist beyond thresholding. Following this, the higher *s/v* ratio for the experimental biofilm can be attributed to the observed voids and channels (Figure 4.4C & D) that cannot be reproduced by the IbM used in this study. The IbM is limited in this respect and this parameter was deemed unsuitable for validation of the biofilm model. But, it remained useful for experimental comparisons between DCF treatment and control.

The processing of large CLSM datasets generated in this study was a tedious endeavour. Although many automated pre-processing and segmentation (threshold) algorithms have been developed in an attempt to make image processing objective and streamlined, there remains no consensus or gold standard. Even so, the method that one chooses to correct for inconsistencies introduces subjectivity, which makes comparisons to literature difficult. At present, manual inspection and processing performed by an experienced operator, although cumbersome for large data sets, remains the best procedure. Numerous issues may arise during image acquisition that can affect accurate biofilm parameter calculations, including light attenuation in thicker biofilms, un-level stacks, excessive noise, fluorophore bleaching, and out of focus images. These issues are the main cause for preventing full automation of image processing. Attempts have been made to correct for light attenuation (Yerly *et al.*, 2007, Stanciu *et al.*, 2010, Semechko *et al.*, 2018), but these methods increase the complexity and time needed for image processing. The best approach would be to reduce the need for complicated image processing methods by careful microscope set up.

The interval between CLSM measurements (Figure 4.6) is relatively large due to the cumbersome nature of preparing the flow cells for microscopy. Moreover, the gap between

flow cell preparation and microscopic analysis (these occurred in different buildings) was not ideal. Pixel intensity variations could be introduced by fluorophore bleaching while waiting for image capture or by incomplete penetration of the laser in thicker biofilms. An ideal situation would be to have the flow cell reactor set up in the same room as the confocal microscope, so images can be captured more frequently and directly after flow cell preparation.

A few parts of the biofilm were colonised by what appeared to be protists, based on their size and effect on the biofilm (Figure 4.8D). It was observed that protist grazing broke up microcolonies, reduced bacterial abundance, and left parts of the EPS without bacteria. Protists are broadly categorised as single-celled eukaryotes, many of which are known to ‘graze’ on bacteria. Similarly, in literature, protist grazing has been shown to reduce the abundance of bacteria within biofilms and alter biofilm morphology, with obvious consequences on structural parameters (Lawrence and Snyder, 1998, Böhme *et al.*, 2009). Future studies comparing biofilm structure using environmental samples should exercise caution since significant protist grazing could affect quantitative results. Either inspect for significant protist grazing or inhibit eukaryotic growth. In the present study, protist grazing was assumed to have a negligible effect on structural parameters since a minority of the observed biofilm was colonised by protists.

A sensitivity analysis conducted on two parameters with suspected uncertainty, inoculation number and  $k_{\text{Det}}$ , demonstrated significant effects on emergent biofilm structure (Figure D2-3). This finding raised doubts about the legitimacy of the validation results (Figure 4.6) when it comes to specifying the number of agents to initiate the simulation. The relation between experimental and model inoculation numbers should be improved. However, inoculation density in experimental set ups are extremely difficult to control. Xavier *et al.* (2004) evaded this issue by using the observed biomass distribution from CLSM data as a starting condition for the simulation. This is an ideal solution to the uncertainty of inoculation numbers experienced in the present study (Figure D2).

The insensitivity of  $R_a$  and  $c_f$  to model parameter uncertainties ( $k_{\text{Det}}$  in this study) is in agreement with Muhammad and Eberl (2011) who reported a similar outcome when varying the flow regime (Reynolds number) of the bulk fluid. This insensitivity to environmental perturbations may explain the failure of the IbM to replicate observed fold changes of  $R_a$  and  $c_f$  for DCF-treated biofilms (Figure 4.12). Experimental  $R_a$  and  $c_f$  are, however, sensitive to environmental changes, and will remain useful for future comparative studies.

It was found that biofilm growth overall was inhibited by exposure to 10 mg.L<sup>-1</sup> DCF (Figure 4.9). This result was expected and several studies have reported similar inhibition of microbial biofilms by DCF (Paje *et al.*, 2002, Bandara *et al.*, 2004, Lawrence *et al.*, 2007, Reśliński *et al.*, 2015). There are several possible explanations for the observed decrease in biofilm growth. DCF is a known antimicrobial agent, and has been reported to inhibit bacterial growth at the tested concentration (Dastidar *et al.*, 2000, Mazumdar *et al.*, 2009). There is also evidence that DCF exposure inhibits biofilm adhesion and formation on surfaces. Bandara *et al.* (2004) reported a significant decrease in DCF-treated (>600 mg.L<sup>-1</sup>) biofilm colonisation on contact lenses for *P. aeruginosa*, *Staphylococcus* sp., *Streptococcus* sp., and *Haemophilus* sp. At a much lower concentration of 1 mg.L<sup>-1</sup>, Reśliński *et al.* (2015) reported the inhibition of *Escherichia coli* and *S. aureus* biofilm formation on polypropylene mesh. Inhibition for both studies were based on reductions in sampled biofilm cell counts (CFU/mL), which was observed in the present study as well (Figure 4.7), although the difference from the control was insignificant.

DCF has also been shown to inhibit quorum sensing and elastase production in *P. aeruginosa* (Ulusoy and Bosgelmez-Tinaz, 2013). Quorum sensing is known to regulate biofilm formation and the production of EPS components, and its inhibition has consequences on biofilm structure (Flemming and Wingender, 2010). Although DCF has only been shown to inhibit quorum sensing in *P. aeruginosa* thus far, this may be an explanation for the decrease in biofilm formation reported in the present study (Figure 4.9). Future work should identify the relative species abundance of the biofilm and changes thereof induced by DCF treatment. This is relevant since species composition is known to influence emergent biofilm structure (Picioreanu *et al.*, 2000b). Possible methods include quantitative-PCR and metagenomics. A particularly useful approach is the combination of CLSM with species-specific probes (e.g. FISH probes) that can be used to track changes in the abundance and localisation of species within a biofilm.

In contrast to multiple studies (Paje *et al.*, 2002, Lawrence *et al.*, 2012, Reśliński *et al.*, 2015), biofilm growth was observed to increase in flow cells compared to the control after 24 h of DCF treatment at 100 µg.L<sup>-1</sup> (Figure 4.10). In support of this finding, Lawrence *et al.* (2007) reported a significant increase in river biofilm community biomass (as µm<sup>3</sup>.µm<sup>-2</sup>), thickness, and bacterial phyla compared to a control when exposed to the same DCF concentration. Carbon source utilisation was also depressed when exposed to 100 µg.L<sup>-1</sup> DCF in summer, but the opposite effect was observed in spring (Lawrence *et al.*, 2007). The

change based on seasons can be explained by shifts in microbial community composition associated with changes in environmental conditions (Kaevska *et al.*, 2016). In contrast to these findings, Lawrence *et al.* (2012) reported a decrease in the algal and bacterial biomass, thickness, as well as biodiversity of river biofilms when exposed to DCF at 5  $\mu\text{g.L}^{-1}$ . Furthermore, Paje *et al.* (2002) found that mature, 11-week-old river biofilms lost up to 70% of its biomass (measured as thickness) after 4 weeks of exposure to DCF at 100  $\mu\text{g.L}^{-1}$ . Acclimatised biofilms did not fare well either compared to control biofilms. When slides were inserted into the DCF-acclimatised reactor, the resultant biofilm was significantly thinner compared to the control after 3, 4, and 8 weeks of growth. For both cases, the CFU/ml and diversity of organisms isolated were significantly reduced compared to the control, with the former observed in the present study as well (Figure 4.7).

Jiang *et al.* (2017) reported a significant increase in oxidative enzyme activity and EPS production of activated sludge when exposed to 5  $\mu\text{g.L}^{-1}$  DCF. An increase in oxidative enzyme activity is an indication of a stress response induced to protect the cell from oxidative damage (Diniz *et al.*, 2015). The EPS is known to protect resident bacteria within biofilms and its production is often induced in response to environmental stress (Delgado *et al.*, 2010, Jiang *et al.*, 2017). The apparent increase in biofilm growth observed in Figure 4.10 may have, in fact, been due to an upregulation of EPS production in response to oxidative stress induced by moderate DCF toxicity.

The effect of DCF treatment in the  $\mu\text{g.L}^{-1}$  range on microbial communities is more complex than initially thought, with conflicting results in literature. A number of internal and external factors appear to be involved, such as species composition, history of the culture (including acclimation to the MP), and environmental conditions. In order to model these interactions, a better fundamental understanding of the effect of low concentration DCF treatment on microbial communities is required. The unknown species composition of the sample used in the present study is an added complication. Future work should make use of a more controlled system, such as a microbial consortium with a known composition. Future experiments should also evaluate the effect of biofilms grown with DCF as the sole carbon source.

There was no significant biodegradation of DCF over the treatment period (Figure 4.11). Likewise, González *et al.* (2006) observed no biodegradation of DCF in a fixed-bed biofilm reactor inoculated with a WWTP community over a 24 d period, even after acclimation to the drug. However, the authors did find that removal efficiency increased

to 44-85% using a moving bed biofilm reactor with plastic carriers. Paje *et al.* (2002) demonstrated the difference in response of acclimated vs. non-acclimated river biofilms (grown in lab-scale microcosms) when exposed to  $100 \mu\text{g.L}^{-1}$  DCF. The authors reported a significant increase in removal efficiency, from 20% to 97%, after 10 weeks of acclimation. The removal of DCF appears to depend on the presence of species capable of metabolising the drug and is linked with reactor configuration. Studies have indicated that nitrification, observed in thinner biofilms, is linked with higher DCF removal efficiency (Torresi *et al.*, 2016). Nitrification was not a dominant process in the biofilm reactor used in the present study which may explain the lack of DCF removal (Figure 4.11). Since the sampled culture was sourced from a WWTP, perhaps the culture was acclimated by chronic exposure to trace levels of DCF. This may be an explanation for the positive response to DCF exposure observed in Figure 4.10. Unfortunately, data on the levels of DCF received by Athlone WWTP was not available. However, DCF is almost ubiquitously detected in WWTP influent in South Africa, so previous exposure of the sampled culture is very likely (Agunbiade and Moodley, 2016, Archer *et al.*, 2017a).

DCF appeared to increase slightly in the effluent (Figure 4.11), though the difference is insignificant ( $P>0.05$ ). González *et al.* (2006) reported a similar finding for a fixed-bed biofilm reactor. A negative mass balance is not an unrealistic scenario. This phenomenon, where effluent concentration is higher than in the influent, has been observed to occur during wastewater treatment for several MPs including DCF (Archer *et al.*, 2017a). This is believed to occur due to back-transformation of metabolites into the parent compound, and/or from the release of accumulated MPs in bacterial aggregates (Archer *et al.*, 2017a). The latter could be an explanation for the possible negative mass balance observed in the present study. It can also be assumed that sorption of DCF to biomass was minimal, which is in agreement with González *et al.* (2006). But, this should be confirmed experimentally since the amount of biomass within the flow cells is low and thus has a low sorption capacity. In hindsight, any biodegradation of DCF that may have occurred is likely not detectable given the short retention time and low biomass present in the system, as well as the persistent nature of the drug.

Although the IbM reasonably reproduced observed structure during initial biofilm development in the validation run (Figure 4.6), the treatment experiments reached a lower steady-state biofilm thickness than predicted after 72 h (Figure 4.12-13). Furthermore, treatment simulations did not result in a direct match to experimental structural parameters. However, the

expected qualitative effect was reproduced. Biofilm growth is stochastic which can lead to differences in emergent structure between experimental repeats (Heydorn *et al.*, 2000a). The stochastic growth of the mixed-species sample (with unknown composition) used in the present study could explain the differences observed in steady-state thickness between validation and treatment runs, though experimental error could not be ruled out. Because of this, a pattern-oriented approach for comparisons between observed and predicted DCF-treated biofilms was adopted (Grimm *et al.*, 2005). Here, fold changes from the control were used for comparisons between experimental and predicted biofilm parameters. This approach has been suggested for analysing stochastic and complex biological systems to reduce the effect of model parameter uncertainty (Grimm *et al.*, 2005). This is particularly relevant for the IbM used in the present study which involved uncertain model parameters.

The pattern-oriented approach adopted in this study proved to be ideal for comparing proportional effects on biofilm structural parameters when reproducibility was an issue (Figure 4.14). The incorporation of a simple inhibition equation (Eq. 17) successfully reproduced observed fold changes of  $\bar{L}_f$  and  $B$  of biofilms exposed to DCF at 10 mg.L<sup>-1</sup> (Figure 4.14A). This finding confirms the hypothesis that DCF exhibits an antimicrobial effect at 10 mg.L<sup>-1</sup>. In this study,  $K_{I,DCF}$  was estimated based on literature MICs. Future experiments should fit the  $K_{I,DCF}$  parameter to the experimental data or perform separate determination experiments. The failure of the model to reproduce the proportion of fold changes for  $R_a$  and  $c_f$  is not surprising given the structural complexity of experimental biofilms that the IbM cannot reproduce, such as voids and streamers (Figure 2.2). Moreover, predicted  $R_a$  and  $c_f$  were found to be insensitive to environmental perturbations, as discussed earlier. This insensitivity potentially limits the use of these parameters for modelling studies investigating the impact of environmental changes.

To reproduce the increase in biofilm growth observed at 0.1 mg.L<sup>-1</sup> (Figure 4.10) a Haldane kinetic (Eq. 18) was implemented in the biofilm model. The model implementation was able to sufficiently describe the effect of 0.1 mg.L<sup>-1</sup> DCF treatment on the biofilm (Figure 4.14B). The model replicated the fold change for  $B$  and  $c_f$  reasonably well, whereas  $\bar{L}_f$  and  $R_a$  was under- and over-estimated, respectively. Although the pattern-oriented approach yields better comparative results here, the relation between multidimensional simulations and experiments needs to be improved.

It was initially hypothesised that DCF at 0.1 mg.L<sup>-1</sup> was utilised as a carbon or energy source, where a substrate addition, attributed to DCF, was added on top of the standard

influent concentration. This did not reproduce the increase in growth observed experimentally using the proposed model (shown in Figure C2). The model indicated that, at the measured COD concentration, the biofilm was substrate saturated, so the increase in growth of the biofilm could not be attributed to an increase in substrate availability. The model, however, lumps substrate into a single variable – as COD. This representation may be too simple for the system being modelled, where a complex medium and a mixed-species culture was used. In this case, a multi-substrate model may be more appropriate to describe microbial carbon utilisation. Moreover, LCMS results indicated insignificant biodegradation of DCF, which opposes the hypothesis. However, as mentioned earlier, the amount of biomass present in the flow cells may have been too low for this to be detected. Overall, this implementation may have been flawed given the complexity of DCF-microbial interactions in the  $\mu\text{g.L}^{-1}$  range discussed earlier.

The iDyNoMiCS framework does not simulate the mechanical forces that fluid flow exhibits on the biofilm structure. In iDyNoMiCS, detachment is implemented as a detachment rate function rather than a mechanistic approach. Recently, the NUFEB IbM has closed this gap and will prove useful in future studies where fluid flow is an important factor (Jayathilake *et al.*, 2017). It is known that higher flow rates (shear forces) deform biofilms in the direction of flow, with consequences on biofilm structure (Picioreanu *et al.*, 2001, Alpkvist and Klapper, 2007a). However, the reactor in this study was run at a relatively slow flow rate, so the effect of shear forces on biofilm architecture were likely low.

The IbM lacks the ability to simulate the ‘stickiness’ of EPS that hold biofilm aggregates together. The secretion of EPS components, and their local density, may mediate mechanical interactions between cells within a biofilm (Flemming and Wingender, 2010). Melaugh *et al.* (2018) recently investigated emergent effects of a local density-dependent cohesion mechanism in an IbM simulating Brownian suspensions. Simulations resulted in an emergent “phase separation” that has a striking similarity to the mounds and irregular channels with loose cells in-between observed in mature biofilms in the present study (Figure 4.4D). A mechanism that simulates polymer-mediated attraction between particles or “EPS adhesive force” has been incorporated into the recently developed NUFEB IbM (Jayathilake *et al.*, 2017), which has great potential for use in future biofilm IbM studies, as mentioned earlier.

Another criticism of the IbM is that they describe bacteria as hard, incompressible spheres, whereas in reality, bacterial cells are more plastic in nature, and are known to deform under external pressure (Laspidou *et al.*, 2010). As for the EPS, it is known to behave more like a

viscous fluid than a rigid structure as represented in iDyNoMiCS. Furthermore, iDyNoMiCS does not simulate bacterial motility which is known to occur in some species and has been shown to influence biomass spreading and emergent biofilm structure (Picioreanu *et al.*, 2007, Ghanbari *et al.*, 2016).

In iDyNoMiCS, particle shape is limited to spheres. In reality, bacterial cells come in a range of shapes and sizes, but can be broadly categorized into cocci (spherical) and bacilli (rod-shaped). This may not be an issue for single-species biofilms with a known cell morphology, but environmental samples will inevitably contain a variety of cell morphologies. In the present study, both cocci- and rod-shaped bacteria were observed in the biofilm (Figure 4.4 & 4.8). Using an IbM, Smith *et al.* (2017) found that cell shape was an important factor determining cell positioning and survival within a biofilm. When both cocci- and rod-shaped cells were allowed to compete for space, rod-shaped cells tended to colonise and expand along the base of the biofilm whereas coccal cells dominated the upper surface and extended as mounds into the bulk liquid (Smith *et al.*, 2017). Cell shape may therefore affect emergent biofilm structure in biofilms. The results are interesting and may explain the localisation of bacterial types observed in biofilms in the present study (Figure 4.8). In some confocal micrographs of mature biofilms, it was observed that cocci-shaped cells aggregated into defined microcolonies which were surrounded by less defined communities of rod-shaped cells occupying channels between these structures. Clearly, cell shape should be considered in future modelling studies.

As more complexity is introduced to IbMs, simulations become more computationally intense. It is for this reason why many biofilm models disregard complexity in favour of reasonable computation times. Improvements to the limitations of iDyNoMiCS outlined above should be paralleled with more efficient numerical methods.

## CHAPTER 6: CONCLUSION

Biokinetic parameters were estimated with good precision using the respirometric methods and the proposed conceptual batch model. The regression of a simple batch model to three sets of response variables proved to be a sufficiently robust and quick method of estimating lumped kinetic parameters of an unknown environmental sample. Precision could be improved with more frequent and automated OUR measurements. Heterotrophic growth was found to dominate autotrophs under the prevailing reactor conditions using respirometry and a nitrification inhibitor. This information was useful for informing the design of the biofilm model.

Observed structure of mixed-species biofilms grown in flow cells was successfully used to validate the proposed biofilm model which satisfies the first aim set out in this project. In spite of the limitations of iDynoMiCS, structure prediction for initial biofilm development was precise for most structural parameters with the calibrated model, except for  $B$  which was overestimated. Variability in  $\bar{L}_f$  and  $B$  was observed to increase over time which is a concern for longer term studies. The  $s/v$  ratio was shown to be unsuitable for simulated and experimental comparisons. Future studies should also consider fitting structural parameters to improve model calibration.

DCF was found to have a dose-dependent effect on microbial biofilms. Using flow cell experiments and confocal microscopy, DCF exposure was found to inhibit biofilm growth at  $10 \text{ mg.L}^{-1}$  based on a decrease in  $\bar{L}_f$ ,  $B$ , and  $c_f$ . This finding was in agreement with literature and confirmed the proposed hypothesis that DCF will exhibit a sub-inhibitory effect at this concentration. Conversely, at  $0.1 \text{ mg.L}^{-1}$ , biofilm growth increased following 24 h of exposure based on an increase in  $\bar{L}_f$  and  $B$ , with inconsistent results in literature. In order to confidently model this interaction, further research is required to elucidate the fundamental interactions of DCF exposure in the  $\mu\text{g.L}^{-1}$  range on microbial communities. Overall, it was shown that experimental biofilm structural parameters are sufficiently sensitive to environmental changes.

The second aim of this study, to reproduce observed effects of DCF-treatment on biofilm structure, was only partially met. The biofilm model was unable to directly match experimental results for the structural parameters at both  $0.1$  and  $10 \text{ mg.L}^{-1}$  DCF. The pattern-oriented approach adopted in this study proved to be useful for comparing proportional effects on biofilm structural parameters when reproducibility was an issue. Based on fold changes from a control, the IbM was capable of describing the observed antimicrobial effect of DCF

treatment at 10 mg.L<sup>-1</sup> using the proposed inhibition kinetic. The proposed Haldane kinetic reasonably reproduced observed fold changes in structural parameters at 0.1 mg.L<sup>-1</sup>. Although experimental comparisons of biofilm structural parameters are common in literature, this was one of the only studies that have attempted to reproduce such observations using an IbM. The ability of the IbM to reproduce antimicrobial effects on emergent biofilm structure shows potential for investigating antibiotic treatment of biofilms and improving treatment strategies of biofilm-associated infections.

The third aim set out in this study, to investigate the feasibility of the use of observed biofilm structure for the validation of an IbM, was met on the basis of investigations into experimental reproducibility and data processing, model parameter uncertainties, and limitations of the IbM. CLSM and digital image processing proved to be effective for analysing experimental biofilm structure for both qualitative and quantitative comparisons. However, reproducibility of biofilm growth within flow cells and a lack of standardised image processing protocols was found to be an issue. The IbM would be better suited for modelling systems with a known species composition to avoid the uncertainty introduced by an unknown sample composition. Future studies should exercise as much control over the experimental variables as possible. In order to take full advantage of the predictive capability of the biofilm model, an integrated development of models and experimental methods is required. In the effort to further integrate experimental and model data, a genomic aspect should also be considered for model validation, such as metagenomics or qPCR to quantify the relative species abundance of biofilms.

The brief investigation into the sensitivity of emergent biofilm structure to model parameter uncertainties indicated that experimental techniques need to be improved, or new ones developed, to allow for more accurate model parameter determination. The insensitivity of predicted  $R_a$  and  $c_f$  to changes in certain model parameters suggests they are not suitable for describing differences between simulated biofilms, which limits their use for experimental comparisons. Though, further investigations into the effect of other model parameters are required. A better correlation with reality is required for these parameters to improve the confidence of predictions made by the model. Future studies should be accompanied by a parameter sensitivity analysis to inform the interpretation of results and improve model development.

This study demonstrated that structural parameters commonly used for experimental comparisons in literature can be derived from multidimensional biofilm simulations and

compared in a meaningful manner. Individual-based models coupled with comparative experimental methods show potential as a tool for investigating biofilm interactions and improving model development.

IbMs show great promise in simulating biofilms from the ground-up, however, iDynoMiCS was limited with respect to two key aspects: the hydrodynamics of the bulk liquid, and polymer-mediated attraction of the extracellular matrix. The standardised adoption of these features, along with more efficient numerical methods, would bring IbMs closer to simulating biofilm development from first principles.

## CHAPTER 7: REFERENCES

- Abbas, H. A., Serry, F. M. & EL-Masry, E. M. 2012. Combating *Pseudomonas aeruginosa* biofilms by potential biofilm inhibitors. *Asian Journal of Research in Pharmaceutical Sciences*, 2, 66-72.
- Agunbiade, F. O. & Moodley, B. 2016. Occurrence and distribution pattern of acidic pharmaceuticals in surface water, wastewater, and sediment of the Msunduzi River, KwaZulu-Natal, South Africa. *Environmental Toxicology and Chemistry*, 35, 36-46.
- Almeida, M. & Butler, D. 2002. In-sewer wastewater characterization and model parameter determination using respirometry. *Water Environment Research*, 74, 295-305.
- Alpkvist, E. & Klapper, I. 2007a. Description of mechanical response including detachment using a novel particle model of biofilm/flow interaction. *Water Science and Technology*, 55, 265-273.
- Alpkvist, E. & Klapper, I. 2007b. A multidimensional multispecies continuum model for heterogeneous biofilm development. *Bulletin of Mathematical Biology*, 69, 765-789.
- Alpkvist, E., Picioreanu, C., van Loosdrecht, M. C. M. & Heyden, A. 2006. Three-dimensional biofilm model with individual cells and continuum EPS matrix. *Biotechnology and Bioengineering*, 94, 961-79.
- Annadurai, S., Basu, S., Ray, S., Dastidar, S. G. & Chakrabarty, A. N. 1998. Antibacterial activity of the antiinflammatory agent diclofenac sodium. *Indian Journal of Experimental Biology*, 36, 86-90.
- APHA. 1998. *Standard methods for the examination of water and wastewater*, American Public Health Association. Washington, DC.
- Archer, E., Petrie, B., Kasprzyk-Hordern, B. & Wolfaardt, G. M. 2017a. The fate of pharmaceuticals and personal care products (PPCPs), endocrine disrupting contaminants (EDCs), metabolites and illicit drugs in a WWTW and environmental waters. *Chemosphere*, 174, 437-446.
- Archer, E., Wolfaardt, G. M. & van Wyk, J. H. 2017b. Pharmaceutical and personal care products (PPCPs) as endocrine disrupting contaminants (EDCs) in South African surface waters. *Water SA*, 43, 684-706.
- Bandara, B. M. K., Sankaridurg, P. R. & Willcox, M. D. P. 2004. Non-steroidal anti inflammatory agents decrease bacterial colonisation of contact lenses and prevent adhesion to human corneal epithelial cells. *Current Eye Research*, 29, 245-251.
- Becker, P., Hufnagle, W., Peters, G. & Herrmann, M. 2001. Detection of differential gene expression in biofilm-forming versus planktonic populations of *Staphylococcus aureus* using micro-representational-difference analysis. *Applied and Environmental Microbiology*, 67, 2958-2965.
- Bessa, V. S., Moreira, I. S., Tiritan, M. E. & Castro, P. M. L. 2017. Enrichment of bacterial strains for the biodegradation of diclofenac and carbamazepine from activated sludge. *International Biodeterioration & Biodegradation*, 120, 135-142.
- Bester, E., Edwards, E. A. & Wolfaardt, G. M. 2009. Planktonic cell yield is linked to biofilm development. *Canadian Journal of Microbiology*, 55, 1195-1206.
- Bishnoi, A., Carlson, H. E., Gruber, B. L., Kaufman, L. D., Bock, J. L. & Lidonnici, K. 1994. Effects of commonly prescribed nonsteroidal anti-inflammatory drugs on thyroid hormone measurements. *The American Journal of Medicine*, 96, 235-238.
- Böhme, A., Risse-Buhl, U. & Küsel, K. 2009. Protists with different feeding modes change biofilm morphology. *FEMS Microbiology Ecology*, 69, 158-169.
- Bonnefille, B., Gomez, E., Courant, F., Escande, A. & Fenet, H. 2018. Diclofenac in the marine environment: A review of its occurrence and effects. *Marine Pollution Bulletin*, 131, 496-506.

- Chang, I., Gilbert, E. S., Eliashberg, N. & Keasling, J. D. 2003. A three-dimensional, stochastic simulation of biofilm growth and transport-related factors that affect structure. *Microbiology*, 149, 2859-2871.
- Checchi, N. & Marsili-Libelli, S. 2005. Reliability of parameter estimation in respirometric models. *Water Research*, 39, 3686-3696.
- Costerton, J. W., Lewandowski, Z., Caldwell, D. E., Korber, D. R. & Lappin-Scott, H. M. 1995. Microbial biofilms. *Annual Reviews in Microbiology*, 49, 711-745.
- Dannhardt, G. & Kiefer, W. 2001. Cyclooxygenase inhibitors—Current status and future prospects. *European Journal of Medicinal Chemistry*, 36, 109-126.
- Dastidar, S. G., Ganguly, K., Chaudhuri, K. & Chakrabarty, A. N. 2000. The anti-bacterial action of diclofenac shown by inhibition of DNA synthesis. *International Journal of Antimicrobial Agents*, 14, 249-251.
- Davies, D. G. & Geesey, G. G. 1995. Regulation of the alginate biosynthesis gene *algC* in *Pseudomonas aeruginosa* during biofilm development in continuous culture. *Applied and Environmental Microbiology*, 61, 860-867.
- Delgado, L. F., Schetrite, S., Gonzalez, C. & Albasi, C. 2010. Effect of cytostatic drugs on microbial behaviour in membrane bioreactor system. *Bioresource Technology*, 101, 527-536.
- Diniz, M. S., Salgado, R., Pereira, V. J., Carvalho, G., Oehmen, A., Reis, M. A. M. & Noronha, J. P. 2015. Ecotoxicity of ketoprofen, diclofenac, atenolol and their photolysis byproducts in zebrafish (*Danio rerio*). *Science of the Total Environment*, 505, 282-289.
- Dockery, J. & Klapper, I. 2002. Finger formation in biofilm layers. *SIAM Journal on Applied Mathematics*, 62, 853-869.
- Donlan, R. M. 2002. Biofilms: Microbial life on surfaces. *Emerging Infectious Diseases*, 8, 881-890.
- Dutta, N. K., Annadurai, S., Mazumdar, K., Dastidar, S. G., Kristiansen, J. E., Molnar, J., Martins, M. & Amaral, L. 2007. Potential management of resistant microbial infections with a novel non-antibiotic: The anti-inflammatory drug diclofenac sodium. *International Journal of Antimicrobial Agents*, 30, 242-249.
- Dutta, N. K., Mazumdar, K., Baek, M. W., Kim, D. J., Na, Y. R., Park, S. H., Lee, H. K., Lee, B. H. & Park, J. H. 2008. In vitro efficacy of diclofenac against *Listeria monocytogenes*. *European Journal of Clinical Microbiology & Infectious Diseases*, 27, 315-319.
- Eberl, H. J., Parker, D. F. & Van Loosdrecht, M. C. M. 2001. A new deterministic spatio-temporal continuum model for biofilm development. *Computational and Mathematical Methods in Medicine*, 3, 161-175.
- EU 2015. European Union Commission Implementing Decision (EU) 2015/495 of 20 March 2015. OJ L78, 24.3.2015.
- Falas, P., Longree, P., la Cour Jansen, J., Siegrist, H., Hollender, J. & Joss, A. 2013. Micropollutant removal by attached and suspended growth in a hybrid biofilm-activated sludge process. *Water Research*, 47, 4498-506.
- Flemming, H.-C. & Wingender, J. 2010. The biofilm matrix. *Nature Reviews Microbiology*, 8, 623.
- Fozard, J. A., Lees, M., King, J. R. & Logan, B. S. 2012. Inhibition of quorum sensing in a computational biofilm simulation. *Biosystems*, 109, 105-14.
- Galus, M., Jeyaranjaan, J., Smith, E., Li, H., Metcalfe, C. & Wilson, J. Y. 2013. Chronic effects of exposure to a pharmaceutical mixture and municipal wastewater in zebrafish. *Aquatic Toxicology*, 132, 212-222.
- Ghanbari, A., Dehghany, J., Schwebs, T., Müskens, M., Häussler, S. & Meyer-Hermann, M. 2016. Inoculation density and nutrient level determine the formation of mushroom-shaped structures in *Pseudomonas aeruginosa* biofilms. *Scientific Reports*, 6.

- González, S., Müller, J., Petrovic, M., Barceló, D. & Knepper, T. P. 2006. Biodegradation studies of selected priority acidic pesticides and diclofenac in different bioreactors. *Environmental Pollution*, 144, 926-932.
- Grady Jr, C. L., Glen, T. D. & Lim, H. C. 1999. *Biological Wastewater Treatment (second edition, revised and expanded)*, New York. Basel. Hong Kong, Marcel Dekker, Inc.
- Grimm, V., Revilla, E., Berger, U., Jeltsch, F., Mooij, W. M., Railsback, S. F., Thulke, H.-H., Weiner, J., Wiegand, T. & DeAngelis, D. L. 2005. Pattern-oriented modeling of agent-based complex systems: lessons from ecology. *Science*, 310, 987-991.
- Gröner, F., Höhne, C., Kleiner, W. & Kloas, W. 2017. Chronic diclofenac exposure affects gill integrity and pituitary gene expression and displays estrogenic activity in nile tilapia (*Oreochromis niloticus*). *Chemosphere*, 166, 473-481.
- Hellweger, F. L. & Bucci, V. 2009. A bunch of tiny individuals—Individual-based modeling for microbes. *Ecological Modelling*, 220, 8-22.
- Hellweger, F. L., Clegg, R. J., Clark, J. R., Plugge, C. M. & Kreft, J. U. 2016. Advancing microbial sciences by individual-based modelling. *Nature Reviews Microbiology*, 14, 461-71.
- Henze, M., Grady Jr, C. L., Gujer, W., Marais, G. v. R. & Matsuo, T. 1987. Activated sludge model No. 1. *IAWPRC Scientific and Technical Report No.1*. International Water Association, London.
- Henze, M., Gujer, W., Mino, T., Matsuo, T., Wentzel, M. C. & Marais, G. v. R. 1995. Activated sludge model No. 2. *IAWPRC Scientific and Technical Report No. 3*. IAWQ, London.
- Hermanowicz, S. W. 2001. A simple 2D biofilm model yields a variety of morphological features. *Mathematical Biosciences*, 169, 1-14.
- Heydorn, A., Ersbøll, B. K., Hentzer, M., Parsek, M. R., Givskov, M. & Molin, S. 2000a. Experimental reproducibility in flow-chamber biofilms. *Microbiology*, 146, 2409-2415.
- Heydorn, A., Nielsen, A. T., Hentzer, M., Sternberg, C., Givskov, M., Ersbøll, B. K. & Molin, S. 2000b. Quantification of biofilm structures by the novel computer program COMSTAT. *Microbiology*, 146, 2395-2407.
- Høiby, N., Bjarnsholt, T., Givskov, M., Molin, S. & Ciofu, O. 2010. Antibiotic resistance of bacterial biofilms. *International Journal of Antimicrobial Agents*, 35, 322-332.
- Hong, H. N., Kim, H. N., Park, K. S., Lee, S.-K. & Gu, M. B. 2007. Analysis of the effects diclofenac has on Japanese medaka (*Oryzias latipes*) using real-time PCR. *Chemosphere*, 67, 2115-2121.
- Hunt, S. M., Werner, E. M., Huang, B., Hamilton, M. A. & Stewart, P. S. 2004. Hypothesis for the role of nutrient starvation in biofilm detachment. *Applied and Environmental Microbiology*, 70, 7418-7425.
- Jayathilake, P. G., Gupta, P., Li, B., Madsen, C., Oyebamiji, O., González-Cabaleiro, R., Rushton, S., Bridgens, B., Swailes, D. & Allen, B. 2017. A mechanistic individual-based model of microbial communities. *PloS One*, 12, e0181965.
- Jewell, K. S., Falås, P., Wick, A., Joss, A. & Ternes, T. A. 2016. Transformation of diclofenac in hybrid biofilm-activated sludge processes. *Water Research*, 105, 559-567.
- Jiang, C., Geng, J., Hu, H., Ma, H., Gao, X. & Ren, H. 2017. Impact of selected non-steroidal anti-inflammatory pharmaceuticals on microbial community assembly and activity in sequencing batch reactors. *PloS one*, 12, e0179236.
- Kaevska, M., Videnska, P., Sedlar, K. & Slana, I. 2016. Seasonal changes in microbial community composition in river water studied using 454-pyrosequencing. *SpringerPlus*, 5, 409.

- Kappeler, J. & Gujer, W. 1992. Estimation of kinetic parameters of heterotrophic biomass under aerobic conditions and characterization of wastewater for activated sludge modelling. *Water Science and Technology*, 25, 125-139.
- Kissel, J. C., McCarty, P. L. & Street, R. L. 1984. Numerical simulation of mixed-culture biofilm. *Journal of Environmental Engineering*, 110, 393-411.
- Klapper, I. & Dockery, J. 2010. Mathematical description of microbial biofilms. *SIAM Review*, 52, 221-265.
- Klapper, I., Rupp, C. J., Cargo, R., Purvedorj, B. & Stoodley, P. 2002. Viscoelastic fluid description of bacterial biofilm material properties. *Biotechnology and Bioengineering*, 80, 289-296.
- Kreft, J. U., Booth, G. & Wimpenny, J. W. T. 1998. BacSim, a simulator for individual-based modelling of bacterial colony growth. *Microbiology*, 144, 3275-3287.
- Kreft, J. U., Picioreanu, C., Wimpenny, J. W. & van Loosdrecht, M. C. M. 2001. Individual-based modelling of biofilm. *Microbiology*, 147, 2897-2912.
- Kreft, J. U. & Wimpenny, J. W. 2001. Effect of EPS on biofilm structure and function as revealed by an individual-based model of biofilm growth. *Water Science and Technology*, 43, 135-135.
- Lardon, L. A., Merkey, B. V., Martins, S., Dötsch, A., Picioreanu, C., Kreft, J. U. & Smets, B. F. 2011. iDyNoMiCS: Next-generation individual-based modelling of biofilms. *Environmental Microbiology*, 13, 2416-2434.
- Laspidou, C. S., Kungolos, A. & Samaras, P. 2010. Cellular-automata and individual-based approaches for the modeling of biofilm structures: Pros and cons. *Desalination*, 250, 390-394.
- Laspidou, C. S. & Rittmann, B. E. 2004. Modeling the development of biofilm density including active bacteria, inert biomass, and extracellular polymeric substances. *Water Research*, 38, 3349-3361.
- Lawrence, J. R., Korber, D. R., Hoyle, B. D., Costerton, J. W. & Caldwell, D. E. 1991. Optical sectioning of microbial biofilms. *Journal of Bacteriology*, 173, 6558-6567.
- Lawrence, J. R. & Snyder, R. A. 1998. Feeding behaviour and grazing impacts of a *Euplotes* sp. on attached bacteria. *Canadian Journal of Microbiology*, 44, 623-629.
- Lawrence, J. R., Swerhone, G. D. W., Topp, E., Korber, D. R., Neu, T. R. & Wassenaar, L. I. 2007. Structural and functional responses of river biofilm communities to the nonsteroidal anti-inflammatory diclofenac. *Environmental Toxicology and Chemistry*, 26, 573-582.
- Lawrence, J. R., Zhu, B., Swerhone, G. D. W., Roy, J., Tumber, V., Waisser, M. J., Topp, E. & Korber, D. R. 2012. Molecular and microscopic assessment of the effects of caffeine, acetaminophen, diclofenac, and their mixtures on river biofilm communities. *Environmental Toxicology and Chemistry*, 31, 508-517.
- Mattei, M. R., Frunzo, L., D'Acunto, B., Pechaud, Y., Pirozzi, F. & Esposito, G. 2018. Continuum and discrete approach in modeling biofilm development and structure: a review. *Journal of Mathematical Biology*, 76, 945-1003.
- Mazumdar, K., Dastidar, S. G., Park, J. H. & Dutta, N. K. 2009. The anti-inflammatory non-antibiotic helper compound diclofenac: an antibacterial drug target. *European Journal of Clinical Microbiology & Infectious Diseases*, 28, 881.
- Mazumdar, K., Dutta, N. K., Dastidar, S. G., Motohashi, N. & Shirataki, Y. 2006. Diclofenac in the management of *E. coli* urinary tract infections. *In Vivo*, 20, 613-619.
- Melaugh, G., Marenduzzo, D., Morozov, A. & Allen, R. J. 2018. Density dependent cohesion leads to controlled phase separation in Brownian suspensions. *preprint*

- Merkey, B. V., Lardon, L. A., Seoane, J. M., Kreft, J. U. & Smets, B. F. 2011. Growth dependence of conjugation explains limited plasmid invasion in biofilms: An individual-based modelling study. *Environmental Microbiology*, 13, 2435-2452.
- Merod, R. T., Warren, J. E., McCaslin, H. & Wuertz, S. 2007. Toward automated analysis of biofilm architecture: Bias caused by extraneous confocal laser scanning microscopy images. *Applied and Environmental Microbiology*, 73, 4922-4930.
- Miller, J. K., Badawy, H. T., Clemons, C., Kreider, K., Wilber, P., Milsted, A. & Young, G. 2012. Development of the *Pseudomonas aeruginosa* mushroom morphology and cavity formation by iron-starvation: A mathematical modeling study. *Journal of Theoretical Biology*, 308, 68-78.
- Miller, M. B. & Bassler, B. L. 2001. Quorum sensing in bacteria. *Annual Reviews in Microbiology*, 55, 165-199.
- Morgenroth, E. & Wilderer, P. A. 2000. Influence of detachment mechanisms on competition in biofilms. *Water Research*, 34, 417-426.
- Mueller, L. N., De Brouwer, J. F. C., Almeida, J. S., Stal, L. J. & Xavier, J. B. 2006. Analysis of a marine phototrophic biofilm by confocal laser scanning microscopy using the new image quantification software PHLIP. *BMC Ecology*, 6, 1.
- Muhammad, N. & Eberl, H. J. 2011. Model parameter uncertainties in a dual-species biofilm competition model affect ecological output parameters much stronger than morphological ones. *Mathematical Biosciences*, 233, 1-18.
- Neu, T. R. & Kuhlicke, U. 2017. Fluorescence lectin bar-coding of glycoconjugates in the extracellular matrix of biofilm and bioaggregate forming microorganisms. *Microorganisms*, 5, 5.
- Ni, B.-J., Yu, H.-Q. & Sun, Y.-J. 2008. Modeling simultaneous autotrophic and heterotrophic growth in aerobic granules. *Water Research*, 42, 1583-1594.
- Noguera, D. R., Pizarfo, G., Stahl, D. A. & Rittmann, B. E. 1999. Simulation of multispecies biofilm development in three dimensions. *Water Science and Technology*, 39, 123-130.
- Oaks, J. L., Gilbert, M., Virani, M. Z., Watson, R. T., Meteyer, C. U., Rideout, B. A., Shivaprasad, H. L., Ahmed, S., Chaudhry, M. J. I. & Arshad, M. 2004. Diclofenac residues as the cause of vulture population decline in Pakistan. *Nature*, 427, 630.
- Osachoff, H. L., Mohammadali, M., Skirrow, R. C., Hall, E. R., Brown, L. L. Y., van Aggenen, G. C., Kennedy, C. J. & Helbing, C. C. 2014. Evaluating the treatment of a synthetic wastewater containing a pharmaceutical and personal care product chemical cocktail: Compound removal efficiency and effects on juvenile rainbow trout. *Water Research*, 62, 271-280.
- Paje, M., Kuhlicke, U., Winkler, M. & Neu, T. 2002. Inhibition of lotic biofilms by diclofenac. *Applied Microbiology and Biotechnology*, 59, 488-492.
- Petrie, B., Barden, R. & Kasprzyk-Hordern, B. 2015. A review on emerging contaminants in wastewaters and the environment: current knowledge, understudied areas and recommendations for future monitoring. *Water Research*, 72, 3-27.
- Petropavlovskii, A. & Sillanpää, M. 2013. Removal of micropollutants by biofilms: Current approaches and future prospects. *Environmental Technology Reviews*, 2, 29-44.
- Picioreanu, C., Kreft, J. U., Klausen, M., Haagensen, J. A. J., Tolker-Nielsen, T. & Molin, S. 2007. Microbial motility involvement in biofilm structure formation—a 3D modelling study. *Water Science and Technology*, 55, 337-343.
- Picioreanu, C., Kreft, J. U. & van Loosdrecht, M. C. M. 2004. Particle-based multidimensional multispecies biofilm model. *Applied and Environmental Microbiology*, 70, 3024-3040.
- Picioreanu, C., Van Loosdrecht, M. C. M. & Heijnen, J. J. 1998a. Mathematical modeling of biofilm structure with a hybrid differential-discrete cellular automaton approach. *Biotechnology and Bioengineering*, 58, 101-116.

- Picioreanu, C., van Loosdrecht, M. C. M. & Heijnen, J. J. 1998b. A new combined differential-discrete cellular automaton approach for biofilm modeling: Application for growth in gel beads. *Biotechnology and Bioengineering*, 57, 718-731.
- Picioreanu, C., Van Loosdrecht, M. C. M. & Heijnen, J. J. 2000a. Effect of diffusive and convective substrate transport on biofilm structure formation: A two-dimensional modeling study. *Biotechnology and Bioengineering*, 69, 504-515.
- Picioreanu, C., van Loosdrecht, M. C. M. & Heijnen, J. J. Modelling and predicting biofilm structure. *Symposia-Society for General Microbiology*, 2000b. Cambridge; Cambridge University Press; 1999, 129-166.
- Picioreanu, C., Van Loosdrecht, M. C. M. & Heijnen, J. J. 2001. Two-dimensional model of biofilm detachment caused by internal stress from liquid flow. *Biotechnology & Bioengineering*, 72, 205-218.
- Pizarro, G., Griffeth, D. & Noguera, D. R. 2001. Quantitative cellular automaton model for biofilms. *Journal of Environmental Engineering*, 127, 782-789.
- Pomies, M., Choubert, J. M., Wisniewski, C. & Coquery, M. 2013. Modelling of micropollutant removal in biological wastewater treatments: a review. *Science of the Total Environment*, 443, 733-48.
- Reśliński, A., Dąbrowiecki, S. & Głowacka, K. 2015. The impact of diclofenac and ibuprofen on biofilm formation on the surface of polypropylene mesh. *Hernia*, 19, 179-185.
- Riefler, R. G., Ahlfeld, D. P. & Smets, B. F. 1998. Respirometric assay for biofilm kinetics estimation: parameter identifiability and retrievability. *Biotechnology and Bioengineering*, 57, 35-45.
- Rittmann, B. E. & McCarty, P. L. 1980. Model of steady-state-biofilm kinetics. *Biotechnology and Bioengineering*, 22, 2343-2357.
- Rittmann, B. E., Schwarz, A. O., Eberl, H. J., Morgenroth, E., Perez, J., van Loosdrecht, M. C. M. & Wanner, O. 2004. Results from the multi-species Benchmark Problem (BM3) using one-dimensional models. *Water Science and Technology*, 49, 163-168.
- Robertson, L. A., Cornelisse, R., Zeng, R. & Kuenen, J. G. 1989. The effect of thiosulphate and other inhibitors of autotrophic nitrification on heterotrophic nitrifiers. *Antonie van Leeuwenhoek*, 56, 301-309.
- Rudge, T. J., Steiner, P. J., Phillips, A. & Haseloff, J. 2012. Computational modeling of synthetic microbial biofilms. *ACS Synthetic Biology*, 1, 345-352.
- Schultz, M. P., Bendick, J. A., Holm, E. R. & Hertel, W. M. 2011. Economic impact of biofouling on a naval surface ship. *Biofouling*, 27, 87-98.
- Semechko, A., Sudarsan, R., Bester, E., Wolfaardt, G., Dony, R., Oliver, M. & Eberl, H. 2018. Influence of light attenuation on biofilm parameters evaluated from CLSM image data. *CMBES Proceedings*, 33.
- Smith, W. P., Davit, Y., Osborne, J. M., Kim, W., Foster, K. R. & Pitt-Francis, J. M. 2017. Cell morphology drives spatial patterning in microbial communities. *Proceedings of the National Academy of Sciences*, 114, 280-286.
- Stanciu, S. G., Stanciu, G. A. & Coltuc, D. 2010. Automated compensation of light attenuation in confocal microscopy by exact histogram specification. *Microscopy Research Technique*, 73, 165-75.
- Stewart, P. S. 2003. Diffusion in Biofilms. *Journal of Bacteriology*, 185, 1485-1491.
- Stewart, P. S. & Franklin, M. J. 2008. Physiological heterogeneity in biofilms. *Nature Reviews Microbiology*, 6, 199-210.
- Sutherland, I. W. 2001. Biofilm exopolysaccharides: A strong and sticky framework. *Microbiology*, 147, 3-9.
- Tolker-Nielsen, T. & Sternberg, C. 2011. Growing and analyzing biofilms in flow chambers. *Current Protocols in Microbiology*, 21, 1B. 2.1-1B. 2.17.

- Torresi, E., Fowler, S. J., Polesel, F., Bester, K., Andersen, H. R., Smets, B. F., Plósz, B. G. & Christensson, M. 2016. Biofilm thickness influences biodiversity in nitrifying MBBRs: Implications on micropollutant removal. *Environmental Science & Technology*, 50, 9279-9288.
- Trojanowicz, K., Styka, W. & Baczyński, T. 2009. Experimental determination of kinetic parameters for heterotrophic microorganisms in biofilm under petrochemical wastewater conditions. *Polish Journal of Environmental Studies*, 18, 913-921.
- Ulusoy, S. & Bosgelmez-Tinaz, G. 2013. Nonsteroidal anti-inflammatory drugs reduce the production of quorum sensing regulated virulence factors and swarming motility in human pathogen *Pseudomonas aeruginosa*. *Drug Research*, 63, 409-413.
- Van Loosdrecht, M. C. M., Heijnen, J. J., Eberl, H., Kreft, J. & Picioreanu, C. 2002. Mathematical modelling of biofilm structures. *Antonie van Leeuwenhoek*, 81, 245-256.
- Vanrolleghem, P. A., Van Daele, M. & Dochain, D. 1995. Practical identifiability of a biokinetic model of activated sludge respiration. *Water Research*, 29, 2561-2570.
- Vorregaard, M. 2008. *Comstat2-a modern 3D image analysis environment for biofilms*. Master's thesis, Technical University of Denmark, DTU, DK-2800 Kgs. Lyngby, Denmark.
- Wanner, O., Eberl, H. J., Morgenroth, E., Noguera, D., Picioreanu, C., Rittman, B. E., Van Loosdrecht, M. C. M. & Modeling), I. T. G. o. B. 2006. *Mathematical modeling of biofilms*, IWA Publishing.
- Wanner, O. & Gujer, W. 1986. A multispecies biofilm model. *Biotechnology and Bioengineering*, 28, 314-328.
- Wilke, C. R. & Chang, P. 1955. Correlation of diffusion coefficients in dilute solutions. *AIChE Journal*, 1, 264-270.
- Wolfhardt, G. M., Lawrence, J. R., Robarts, R. D., Caldwell, S. J. & Caldwell, D. E. 1994. Multicellular organization in a degradative biofilm community. *Applied and Environmental Microbiology*, 60, 434-446.
- Xavier, J. B., De Kreuk, M. K., Picioreanu, C. & van Loosdrecht, M. C. M. 2007. Multi-scale individual-based model of microbial and bioconversion dynamics in aerobic granular sludge. *Environmental Science & Technology*, 41, 6410-6417.
- Xavier, J. B., Picioreanu, C. & Van Loosdrecht, M. C. M. 2004. Assessment of three-dimensional biofilm models through direct comparison with confocal microscopy imaging. *Water Science and Technology*, 49, 177-185.
- Xavier, J. B., Picioreanu, C. & van Loosdrecht, M. C. M. 2005a. A framework for multidimensional modelling of activity and structure of multispecies biofilms. *Environmental Microbiology*, 7, 1085-103.
- Xavier, J. B., Picioreanu, C. & van Loosdrecht, M. C. M. 2005b. A general description of detachment for multidimensional modelling of biofilms. *Biotechnology and Bioengineering*, 91, 651-669.
- Xavier, J. B., Schnell, A., Wuertz, S., Palmer, R., White, D. C. & Almeida, J. S. 2001. Objective threshold selection procedure (OTS) for segmentation of scanning laser confocal microscope images. *Journal of Microbiological Methods*, 47, 169-180.
- Xavier, J. B., White, D. C. & Almeida, J. S. 2003. Automated biofilm morphology quantification from confocal laser scanning microscopy imaging. *Water Science and Technology*, 47, 31-37.
- Yang, X., Beyenal, H., Harkin, G. & Lewandowski, Z. 2000. Quantifying biofilm structure using image analysis. *Journal of Microbiological Methods*, 39, 109-119.
- Yerly, J., Hu, Y., Jones, S. M. & Martinuzzi, R. J. 2007. A two-step procedure for automatic and accurate segmentation of volumetric CLSM biofilm images. *Journal of Microbiological Methods*, 70, 424-433.

Zhang, T. C. & Bishop, P. L. 1994. Evaluation of tortuosity factors and effective diffusivities in biofilms. *Water Research*, 28, 2279-2287.

## CHAPTER 8: APPENDICES

### Appendix A: Supplementary information for Chapter 3

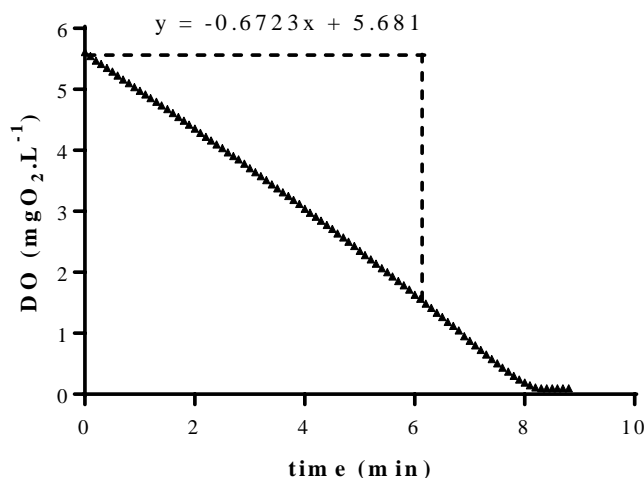


**Figure A1.** Example calculation of OUR. Shown is the DO profile from a measurement in run 3. The slope of the DO profile gives the OUR. Only the slope above  $1.5 \text{ mgO}_2 \cdot \text{L}^{-1}$  is considered to avoid anaerobic conditions. Here,  $\text{OUR} = 0.6723 \text{ mgO}_2 \cdot \text{L}^{-1} \text{ min}^{-1}$ .

**Table A1.** Results of determination of decay coefficient of heterotrophic biomass in batch reactors. Shown are the results for three independent repeats performed in duplicate.

Assay ID	$b_H (\text{h}^{-1})$	$R^2$
Run 1A	0.0173	0.75
Run 1B	0.0207	0.67
Run 2A	0.0230	0.81
Run 2B	0.0190	0.54
Run 3A	0.0211	0.97
Run 3B	0.0222	0.92
Mean	0.0206	
SD	0.0019	
CV (%)	9.3	

SD: Standard deviation. CV: Coefficient of variation (SD/Mean).

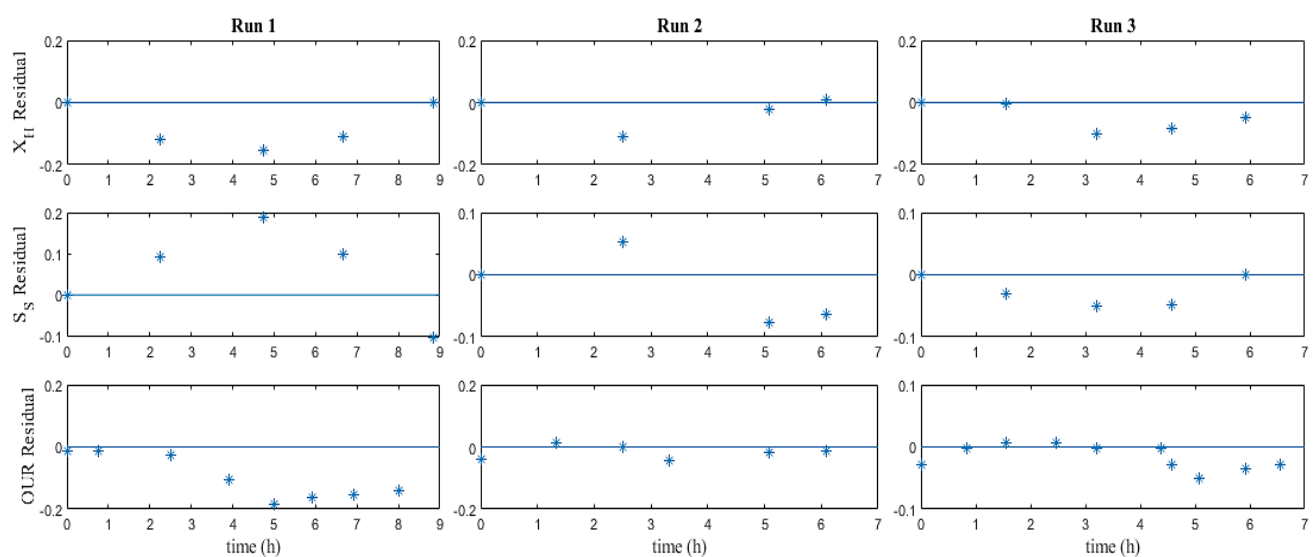
**Table A2.** Initial conditions for batch reactors used to estimate biokinetic parameters.

Assay ID	$\text{OUR}_{t0}$ ( $\text{mgO}_2 \cdot \text{L}^{-1} \text{ h}^{-1}$ )	$S_{s,t0}$ ( $\text{mgCOD} \cdot \text{L}^{-1}$ )	$X_{H,t0}$ ( $\text{mgCOD} \cdot \text{L}^{-1}$ )	$S_s/X_H$
Run 1	1.54	223	16.8	13.3
Run 2	3.76	213	28.0	7.60
Run 3	2.82	261	30.0	8.70

**Table A3.** Fitting statistics resulting from parameter optimisation procedure.

Assay ID	Variable	SSE	R <sup>2</sup>	RMSE	NRMSE (%)
Run 1 (n=9)	X <sub>H</sub>	938	0.90	13.70	18.6
	S <sub>S</sub>	3726	0.88	27.30	20.5
	OUR	84.9	0.70	9.71	42.9
Run 2 (n=6)	X <sub>H</sub>	226	0.97	7.53	8.96
	S <sub>S</sub>	649	0.97	12.75	10.5
	OUR	21.6	0.98	1.90	10.8
Run 3 (n=12)	X <sub>H</sub>	421	0.96	8.38	10.6
	S <sub>S</sub>	919	0.98	12.38	6.71
	OUR	35	0.99	1.71	8.90

SSE: Sum of squared errors. RMSE: Root mean square error. NRMSE: Normalised-RMSE

**Figure A2.** Residual error plots for nonlinear regression of batch model to response variables for three experimental repeats.**Table A4.** Biokinetic parameter values estimated for three experimental repeats. For each run the 95% confidence intervals are indicated.

Assay ID	$\mu_{\max,H}$ (h <sup>-1</sup> )	K <sub>S</sub> (mg <sub>COD</sub> .L <sup>-1</sup> )	Y <sub>H</sub> (mg <sub>COD</sub> .mg <sub>COD</sub> <sup>-1</sup> )	Norm of Residuals
Run 1	0.3101 ± 0.1362	1.0000 ± 19.410	0.4995 ± 0.1211	0.2303
Run 2	0.3408 ± 0.0908	0.9558 ± 14.184	0.4719 ± 0.0493	0.0293
Run 3	0.3024 ± 0.0491	1.7475 ± 4.5125	0.5071 ± 0.0388	0.0406

## **Appendix B: Paraformaldehyde fixative (4%) protocol**

In a glass beaker, 450 mL of 1X phosphate-buffered saline (PBS) was heated to 60°C using a hot plate with stirring. While stirring, 20 g of paraformaldehyde powder (Sigma-Aldrich) was added to the beaker and the temperature maintained at 60°C. The pH was raised slowly by adding 1N NaOH dropwise until the solution clears. The beaker was then removed from the heat, cooled, and 50 mL of 1X PBS was added resulting a final volume of 500 mL. The pH was adjusted to 7.2 using HCl. The solution was then filtered (3HW grade filter paper) and stored in aliquots at -20°C until needed.

## Appendix C: Supplementary information for Chapter 4

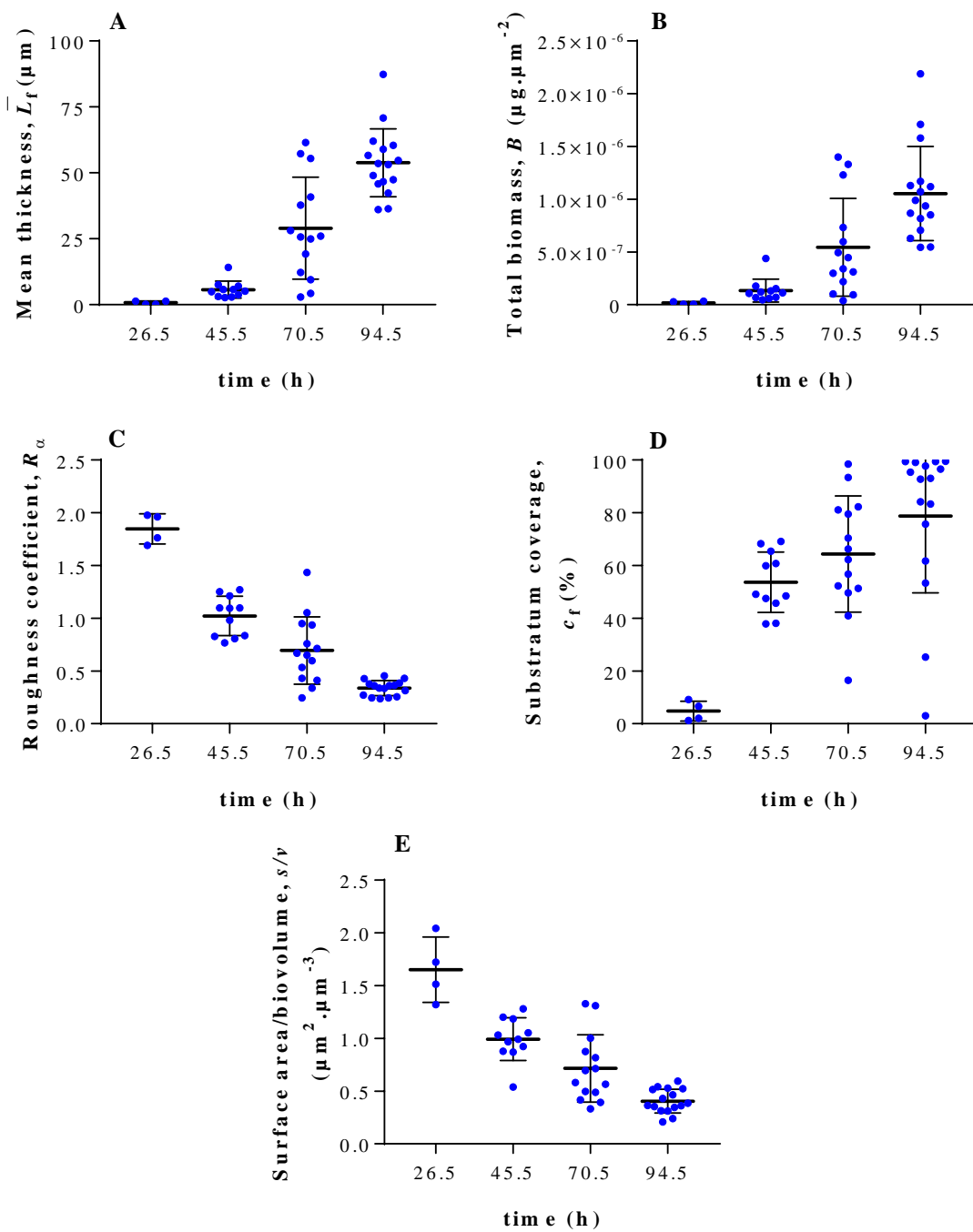


**Figure C1.** Biofilm parameter scatter plot measured for biofilms cultivated under control conditions. **A.** Mean thickness. **B.** Total biomass per substratum area. **C.** Roughness coefficient. **D.** Substratum coverage. **E.** Surface area/biovolume ratio. Individual points indicate each measurement, including outliers, from duplicate flow chambers over time points. The mean and standard deviation are indicated.

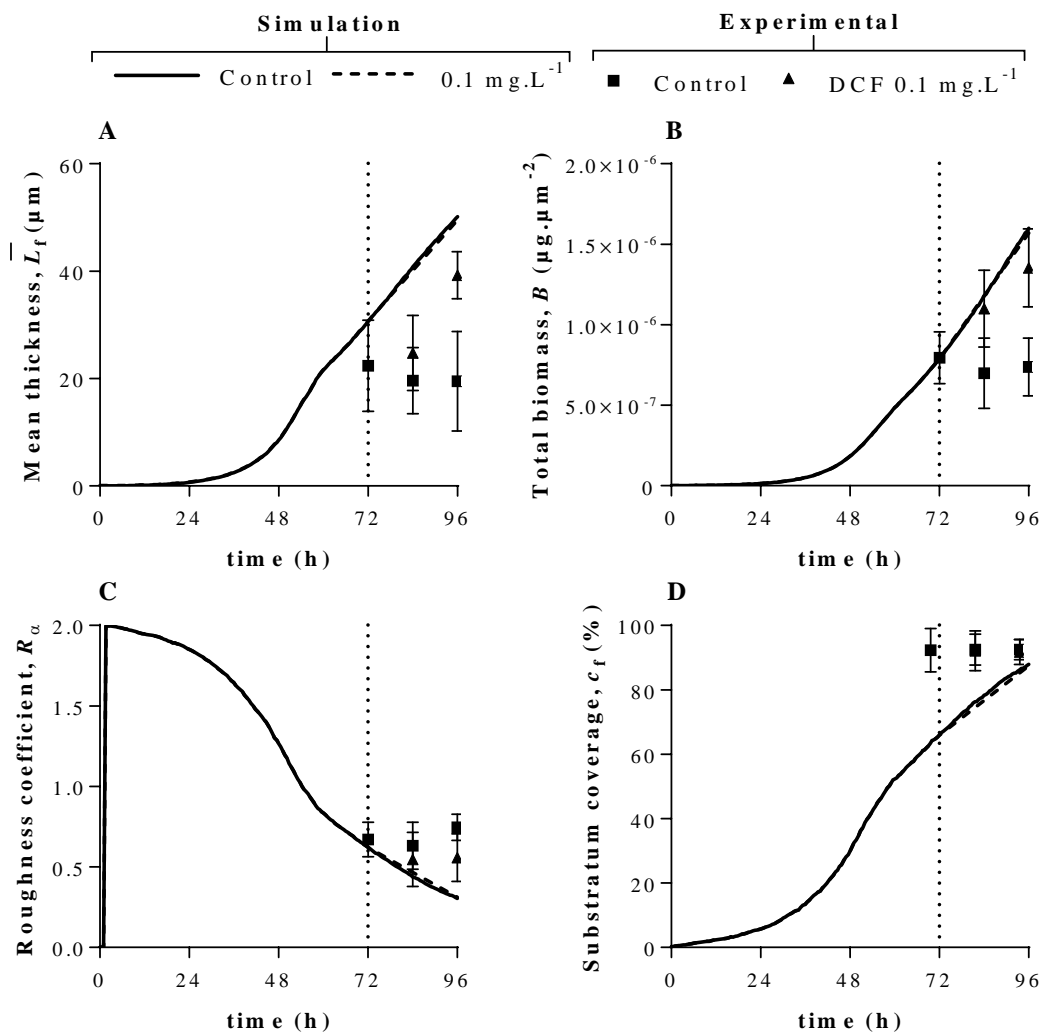


**Figure C2.** Experimental and simulated biofilm structural parameters for control and treatment at  $0.1 \text{ mg.L}^{-1}$  DCF. For the treatment simulation an increase in substrate ( $S_S$ ), attributed to DCF, was implemented. **A.** Mean thickness. **B.** Total biomass. **C.** Roughness coefficient. **D.** Substratum coverage. DCF was introduced at 72 h (indicated by dotted line).

The bulk influent concentration for the treatment simulation was set to  $153.4 \text{ mgCOD.L}^{-1}$  ( $120 + 33.4 \text{ mgCOD.L}^{-1}$ ). DCF contribution calculated based on DCF/COD conversion factor:  $0.1 \text{ mgDCF.L}^{-1} = 33.4 \text{ mgCOD.L}^{-1}$ .

## Appendix D: Sensitivity analysis of simulated structural parameters

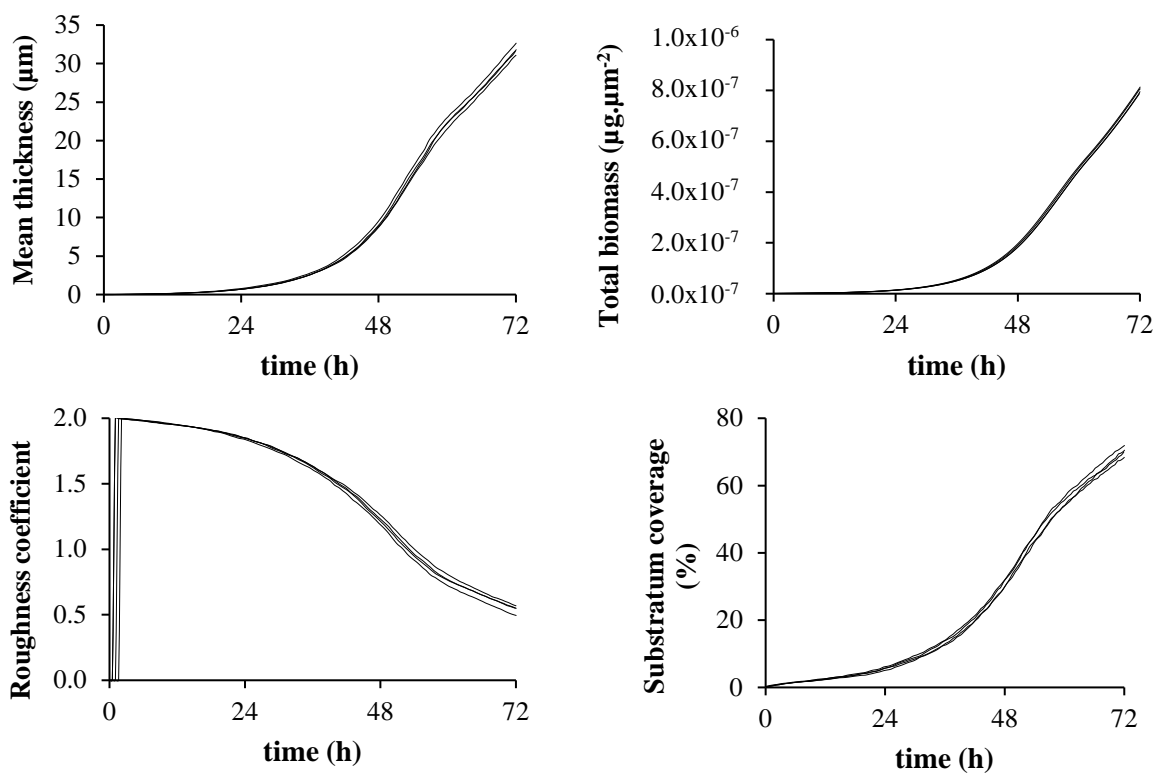


**Figure D1.** Sensitivity of structural parameters to stochastic effects. Four simulations were run using different seed values for the random number generator.

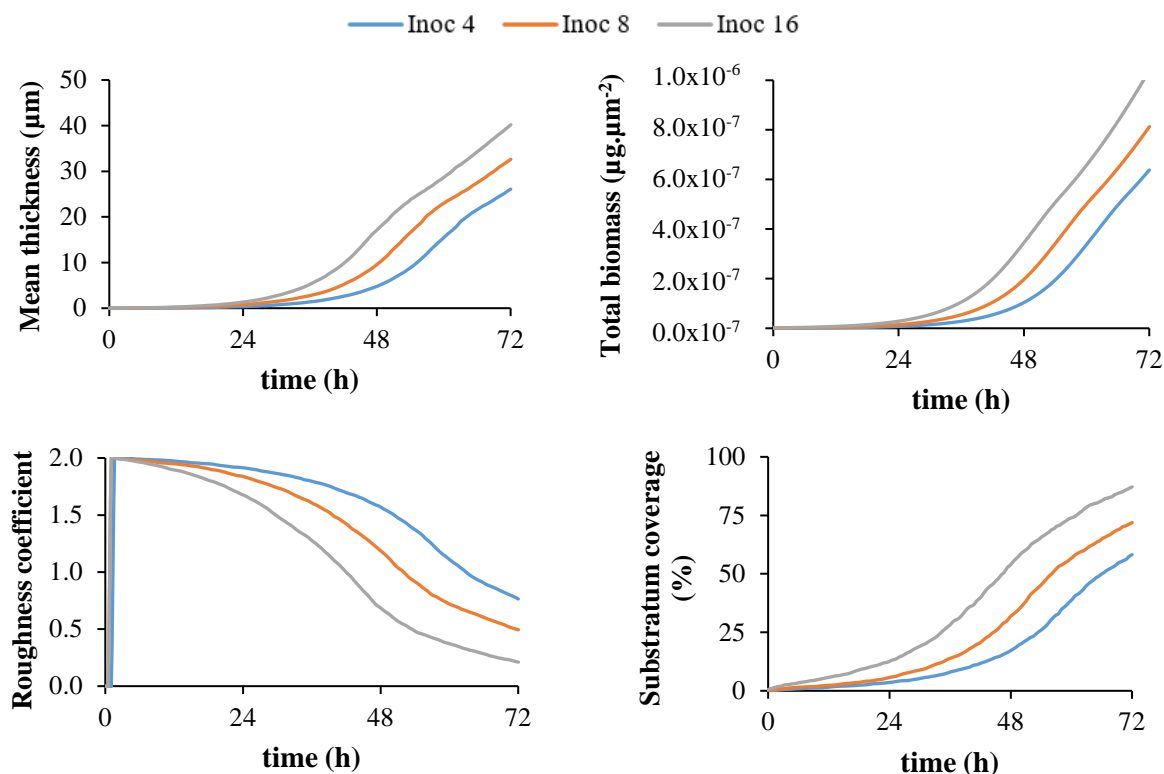


**Figure D2.** Sensitivity of structural parameters to changes in simulation inoculation numbers. Simulations were initiated with the indicated number of particles.

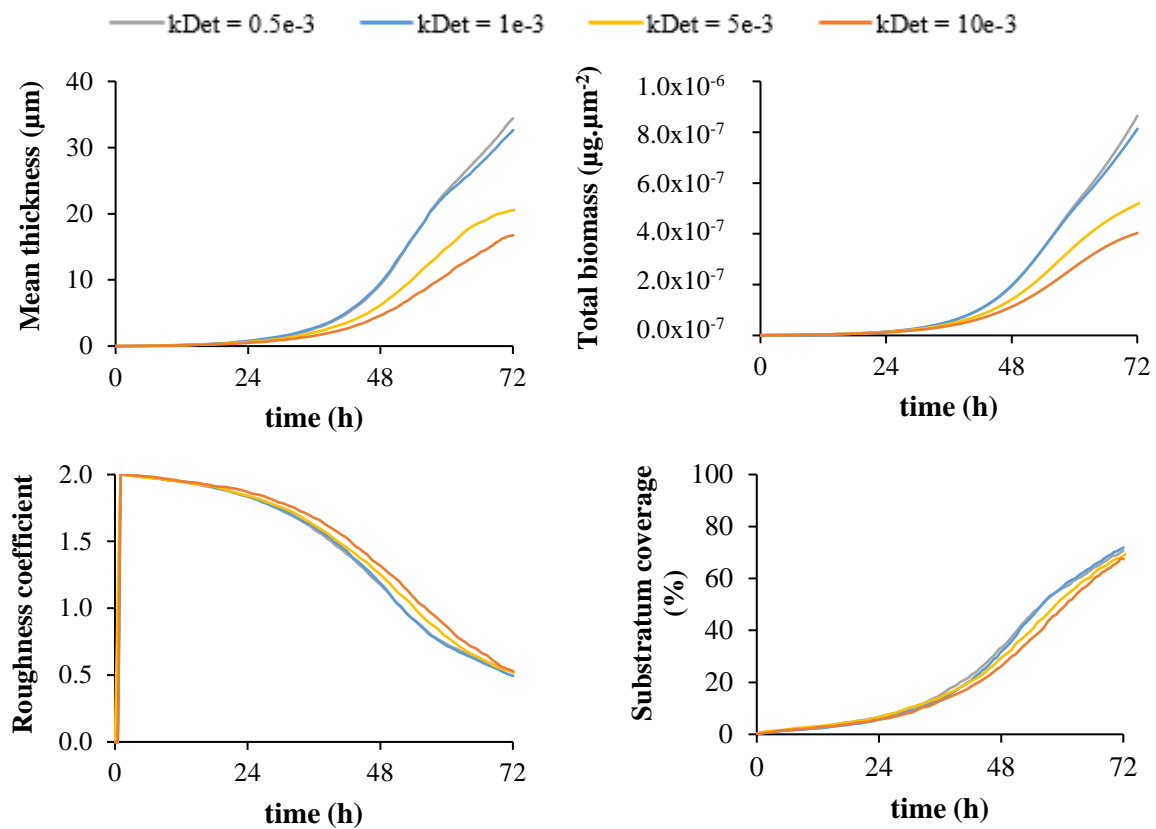


**Figure D3.** Sensitivity of structural parameters to changes in the value of detachment coefficient ( $k_{\text{Det}}$ ).

## Appendix E: Protocol file used to initiate iDyNoMiCS simulations

```

<?xml version="1.0" encoding="UTF-8"?>
<!--
#####
iDyNoMiCS: individual-based Dynamics of Microbial Communities Simulator
#####
-->

Website: http://www.idynamics.org

The entire simulation description is contained within the <idynamics> mark-up tags.
-->

<idynamics>

<!--#####
      SIMULATOR SECTION
#-->

<simulator>
    <param name="quietMode">false</param>
    <param name="restartPreviousRun">false</param>
    <param name="randomSeed">42</param>
    <param name="outputPeriod" unit="hour">0.5</param>
    <param name="checkForReleaseUpdate">false</param>

    <timeStep>
        <param name="adaptive">true</param>
        <param name="timeStepIni" unit="hour">0.5</param>
        <param name="timeStepMin" unit="hour">0.025</param>
        <param name="timeStepMax" unit="hour">0.25</param>
        <param name="endOfSimulation" unit="day">4</param>
    </timeStep>

    <param name="attachment">onetime</param>
    <param name="agentTimeStep" unit="hour">0.025</param>
    <param name="invComp">false</param>
</simulator>

<!--#####
      INPUT SECTION
#-->

<input>
    <param name="useAgentFile">false</param>
    <param name="inputAgentFileURL">agent_State(last).xml</param>
    <param name="useBulkFile">false</param>
    <param name="inputBulkFileURL">env_Sum(last).xml</param>
</input>

<!--#####
      SOLUTES AND BIOMASS TYPES SECTION
#-->

<solute domain="Biofilm" name="O2">
    <param name="diffusivity" unit="m2.day-1">2e-4</param>
</solute>
<solute domain="Biofilm" name="NH4">
    <param name="diffusivity" unit="m2.day-1">1.7e-4</param>
</solute>
<solute domain="Biofilm" name="NO3">
    <param name="diffusivity" unit="m2.day-1">1.7e-4</param>
</solute>
<solute domain="Biofilm" name="COD">
    <param name="diffusivity" unit="m2.day-1">1e-4</param>
</solute>
<solute domain="Biofilm" name="DCF">
    <param name="diffusivity" unit="m2.day-1">0.25e-4</param>

```

```

</solute>
<solute domain="Biofilm" name="pressure">
    <param name="diffusivity" unit="m2.day-1">1</param>
</solute>

<particle name="biomass">
    <param name="density" unit="g.L-1">150</param>
</particle>
<particle name="inert">
    <param name="density" unit="g.L-1">150</param>
</particle>
<particle name="capsule">
    <param name="density" unit="g.L-1">30</param>
</particle>

<!--#####
WORLD SECTION
-->

<world>
    <bulk name="Bulk">
        <param name="isConstant">false</param>
        <param name="D" unit="h-1">18</param>

        <solute name="O2">
            <param name="Sbulk" unit="g.L-1">5e-3</param>
            <param name="Sin" unit="g.L-1">5e-3</param>
            <param name="isConstant">false</param>
        </solute>
        <solute name="NH4">
            <param name="Sbulk" unit="g.L-1">16e-3</param>
            <param name="Sin" unit="g.L-1">16e-3</param>
        </solute>
        <solute name="NO3">
            <param name="Sbulk" unit="g.L-1">0e-3</param>
            <param name="Sin" unit="g.L-1">0e-3</param>
        </solute>
        <solute name="COD">
            <param name="Sbulk" unit="g.L-1">120e-3</param>
            <param name="Sin" unit="g.L-1">120e-3</param>
            <param name="Spulse" unit="g.L-1">0</param>
            <param name="pulseRate" unit="h-1">0</param>
        </solute>
        <solute name="DCF">
            <param name="Sbulk" unit="g.L-1">0</param>
            <param name="Sin" unit="g.L-1">0</param>
        </solute>
        <solute name="pressure">
            <param name="Sbulk" unit="g.L-1">0</param>
            <param name="Sin" unit="g.L-1">0</param>
        </solute>
    </bulk>

    <computationDomain name="Biofilm">
        <grid nDim="3" nI="33" nJ="33" nK="33" />
        <param name="resolution" unit="um">8</param>
        <param name="boundaryLayer" unit="um">48</param>
        <param name="biofilmDiffusivity">0.8</param>
        <param name="specificArea" unit="m2.m-3">1474</param>

        <boundaryCondition class="BoundaryZeroFlux" name="y0z">
            <shape class="Planar">
                <param name="pointIn" i="-1" j="0" k="0" />
                <param name="vectorOut" i="-1" j="0" k="0" />
            </shape>
        </boundaryCondition>
        <boundaryCondition class="BoundaryBulk" name="yNz">
            <param name="activeForSolute">yes</param>
    </computationDomain>
</world>

```

```

        <param name="bulk">Bulk</param>
        <shape class="Planar">
            <param name="pointIn" i="33" j="0" k="0"/>
            <param name="vectorOut" i="1" j="0" k="0"/>
        </shape>
    </boundaryCondition>
    <boundaryCondition class="BoundaryCyclic" name="x0z">
        <shape class="Planar">
            <param name="pointIn" i="0" j="-1" k="0"/>
            <param name="vectorOut" i="0" j="-1" k="0"/>
        </shape>
        <shape class="Planar">
            <param name="pointIn" i="0" j="33" k="0"/>
            <param name="vectorOut" i="0" j="1" k="0"/>
        </shape>
    </boundaryCondition>
    <boundaryCondition class="BoundaryCyclic" name="x0y">
        <shape class="Planar">
            <param name="pointIn" i="0" j="0" k="-1"/>
            <param name="vectorOut" i="0" j="0" k="-1"/>
        </shape>
        <shape class="Planar">
            <param name="pointIn" i="0" j="0" k="33"/>
            <param name="vectorOut" i="0" j="0" k="1"/>
        </shape>
    </boundaryCondition>
</computationDomain>
</world>

<!--#####
      REACTION SECTION
#####-->

<reaction catalyzedBy="biomass" class="ReactionFactor"
name="GrowthAutotrophs">
    <param name="muMax" unit="hour-1">0.0417</param>
    <kineticFactor class="MonodKinetic" solute="NH4">
        <param name="Ks" unit="g.L-1">1e-3</param>
    </kineticFactor>
    <kineticFactor class="MonodKinetic" solute="O2">
        <param name="Ks" unit="g.L-1">0.5e-3</param>
    </kineticFactor>
    <yield>
        <param name="NH4" unit="g.g-1">-4.1667</param>
        <param name="NO3" unit="g.g-1">4.1667</param>
        <param name="O2" unit="g.g-1">-18.024</param>
        <param name="biomass" unit="g.g-1">0.82</param>
        <param name="capsule" unit="g.g-1">0.18</param>
    </yield>
</reaction>

<reaction catalyzedBy="biomass" class="ReactionFactor"
name="MaintenanceAutotrophs">
    <param name="muMax" unit="hour-1">0.005</param>
    <kineticFactor class="MonodKinetic" solute="O2">
        <param name="Ks" unit="g.L-1">0.5e-3</param>
    </kineticFactor>
    <yield>
        <param name="biomass" unit="g.g-1">-1</param>
        <param name="O2" unit="g.g-1">-1</param>
    </yield>
</reaction>

<reaction catalyzedBy="biomass" class="ReactionFactor"
name="InactivationAutotrophs">
    <param name="muMax" unit="hour-1">0.00125</param>
    <kineticFactor class="FirstOrderKinetic"/>
    <yield>
```

```

        <param name="biomass" unit="g.g-1">-1</param>
        <param name="inert" unit="g.g-1">1</param>
    </yield>
</reaction>

<reaction catalyzedBy="biomass" class="ReactionFactor" name="GrowthHeterotrophs">
    <param name="muMax" unit="hour-1">0.3178</param>
    <kineticFactor class="MonodKinetic" solute="COD">
        <param name="Ks" unit="g.L-1">4e-3</param>
    </kineticFactor>
    <kineticFactor class="MonodKinetic" solute="O2">
        <param name="Ks" unit="g.L-1">0.2e-3</param>
    </kineticFactor>
    <yield>
        <param name="COD" unit="g.g-1">-2.029</param>
        <param name="O2" unit="g.g-1">-1.029</param>
        <param name="biomass" unit="g.g-1">0.49</param>
        <param name="capsule" unit="g.g-1">0.2</param>
    </yield>
</reaction>

<reaction catalyzedBy="biomass" class="ReactionFactor"
name="GrowthHeterotrophsDCF">
    <param name="muMax" unit="hour-1">0.327</param>
    <kineticFactor class="MonodKinetic" solute="O2">
        <param name="Ks" unit="g.L-1">0.2e-3</param>
    </kineticFactor>
    <kineticFactor class="HaldaneKinetic" solute="DCF">
        <param name="Ks" unit="g.L-1">0.001e-3</param>
        <param name="Ki" unit="g.L-1">5e-3</param>
    </kineticFactor>
    <yield>
        <param name="O2" unit="g.g-1">-1.029</param>
        <param name="DCF" unit="g.g-1">-1</param>
        <param name="biomass" unit="g.g-1">0.49</param>
        <param name="capsule" unit="g.g-1">0.2</param>
    </yield>
</reaction>

<reaction catalyzedBy="biomass" class="ReactionFactor"
name="MaintenanceHeterotrophs">
    <param name="muMax" unit="hour-1">0.01333</param>
    <kineticFactor class="MonodKinetic" solute="O2">
        <param name="Ks" unit="g.L-1">0.2e-3</param>
    </kineticFactor>
    <yield>
        <param name="biomass" unit="g.g-1">-1</param>
        <param name="O2" unit="g.g-1">-1</param>
    </yield>
</reaction>

<reaction catalyzedBy="biomass" class="ReactionFactor"
name="InactivationHeterotrophs">
    <param name="muMax" unit="hour-1">0.02058</param>
    <kineticFactor class="FirstOrderKinetic"/>
    <yield>
        <param name="biomass" unit="g.g-1">-1</param>
        <param name="inert" unit="g.g-1">1</param>
    </yield>
</reaction>

<reaction catalyzedBy="capsule" class="ReactionFactor" name="HydrolysisEPS">
    <param name="muMax" unit="hour-1">0.007083</param>
    <kineticFactor class="FirstOrderKinetic"/>
    <yield>
        <param name="capsule" unit="g.g-1">-1</param>
        <param name="COD" unit="g.g-1">1</param>
    </yield>

```

```

</reaction>

<!--#####
      SOLVER SECTION
#-->

<solver class="Solver_multigrid" name="solutes" domain="Biofilm">
    <param name="active">true</param>
    <param name="preStep">150</param>
    <param name="postStep">150</param>
    <param name="coarseStep">1500</param>
    <param name="nCycles">5</param>

    <reaction name="GrowthHeterotrophs" />
    <reaction name="GrowthHeterotrophsDCF" />
    <reaction name="MaintenanceHeterotrophs" />
    <reaction name="GrowthAutotrophs" />
    <reaction name="MaintenanceAutotrophs" />
    <reaction name="HydrolysisEPS" />
</solver>
<solver class="Solver_pressure" name="pressure" domain="Biofilm">
    <param name="active">true</param>
</solver>

<!--#####
      AGENT GRID SECTION
#-->

<agentGrid>
    <param name="computationDomain">Biofilm</param>
    <param name="resolution" unit="um">4</param>

    <detachment class="DS_Biomass">
        <param name="kDet" unit="fg.um-4.hour-1">1e-3</param>
        <param name="maxTh" unit="um">400</param>
    </detachment>
    <param name="sloughDetachedBiomass">true</param>
    <param name="shovingMaxNodes">2e6</param>
    <param name="shovingFraction">0.025</param>
    <param name="shovingMaxIter">250</param>
    <param name="shovingMutual">true</param>
</agentGrid>

<!--#####
      SPECIES SECTION
#-->

<species class="ParticulateEPS" name="AutotrophEPS">
    <particle name="capsule">
        <param name="mass" unit="fg">0</param>
    </particle>
    <param name="color">yellow</param>
    <param name="computationDomain">Biofilm</param>
    <param name="divRadius" unit="um">2</param>
    <param name="divRadiusCV">0.0</param>
    <param name="deathRadius" unit="um">0.1</param>
    <param name="deathRadiusCV">0.0</param>
    <param name="babyMassFrac">0.5</param>
    <param name="babyMassFracCV">0.0</param>
    <param name="shoveFactor" unit="um">1.0</param>
    <param name="shoveLimit" unit="um">0.0</param>

    <reaction name="HydrolysisEPS" status="active" />
</species>

<species class="ParticulateEPS" name="HeterotrophEPS">
    <particle name="capsule">
        <param name="mass" unit="fg">0</param>

```

```

        </particle>
    <param name="color">green</param>
    <param name="computationDomain">Biofilm</param>
    <param name="divRadius" unit="um">2</param>
    <param name="divRadiusCV">0.0</param>
    <param name="deathRadius" unit="um">0.1</param>
    <param name="deathRadiusCV">0.0</param>
    <param name="babyMassFrac">0.5</param>
    <param name="babyMassFracCV">0.0</param>
    <param name="shoveFactor" unit="um">1.0</param>
    <param name="shoveLimit" unit="um">0.0</param>

        <reaction name="HydrolysisEPS" status="active"/>
    </species>

    <species class="Bacterium" name="Autotrophs">
        <particle name="biomass">
            <param name="mass" unit="fg">0</param>
        </particle>
        <particle name="inert">
            <param name="mass" unit="fg">0</param>
        </particle>
        <particle name="capsule" class="AutotrophEPS">
            <param name="mass" unit="fg">0</param>
        </particle>
        <param name="color">red</param>
        <param name="computationDomain">Biofilm</param>
        <param name="divRadius" unit="um">2</param>
        <param name="divRadiusCV">0.1</param>
        <param name="deathRadius" unit="um">0.2</param>
        <param name="deathRadiusCV">0.1</param>
        <param name="babyMassFrac">0.5</param>
        <param name="babyMassFracCV">0.1</param>
        <param name="shoveFactor" unit="um">1.15</param>
        <param name="shoveLimit" unit="um">0.0</param>
        <param name="epsMax">0.1</param>

        <reaction name="GrowthAutotrophs" status="active"/>
        <reaction name="MaintenanceAutotrophs" status="active"/>
        <reaction name="InactivationAutotrophs" status="active"/>

        <initArea number="4">
            <param name="birthday" unit="hour">0</param>
            <coordinates x="0" y="0" z="0"/>
            <coordinates x="1" y="264" z="264"/>
        </initArea>
    </species>

    <species class="BactEPS" name="Heterotrophs">
        <particle name="biomass">
            <param name="mass" unit="fg">0</param>
        </particle>
        <particle name="inert">
            <param name="mass" unit="fg">0</param>
        </particle>
        <particle name="capsule" class="HeterotrophEPS">
            <param name="mass" unit="fg">0</param>
        </particle>
        <param name="color">blue</param>
        <param name="computationDomain">Biofilm</param>
        <param name="divRadius" unit="um">2</param>
        <param name="divRadiusCV">0.1</param>
        <param name="deathRadius" unit="um">0.2</param>
        <param name="deathRadiusCV">0.1</param>
        <param name="babyMassFrac">0.5</param>
        <param name="babyMassFracCV">0.1</param>
        <param name="shoveFactor" unit="um">1.15</param>
        <param name="shoveLimit" unit="um">0.0</param>

```

```
<param name="kHyd" unit="hr-1">0.007083</param>

<reaction name="GrowthHeterotrophs" status="active"/>
<reaction name="GrowthHeterotrophsDCF" status="active"/>
<reaction name="MaintenanceHeterotrophs" status="active"/>
<reaction name="InactivationHeterotrophs" status="active"/>

<initArea number="8">
    <param name="birthday" unit="hour">0</param>
    <coordinates x="0" y="0" z="0"/>
    <coordinates x="1" y="264" z="264"/>
</initArea>
</species>
</idynamics>
```